Ⅳ.研究成果の刊行物・別刷

(19)日本国特許庁(JP)　(12)公開特許公報(A)　(11)特許出願公開番号
特開2015-195835
(P2015-195835A)
(43)公開日　平成27年11月9日(2015.11.9)

(51)Int.Cl.			F I			テーマコード（参考）
A61B	10/00	(2006.01)	A61B	10/00	H	
G09B	19/00	(2006.01)	G09B	19/00	G	

審査請求 未請求　請求項の数 4　ＯＬ　（全 22 頁）

(21)出願番号　特願2014-74112(P2014-74112)
(22)出願日　平成26年3月31日(2014.3.31)

(71)出願人　504145308
国立大学法人　琉球大学
沖縄県中頭郡西原町字千原１番地
(74)代理人　100093230
弁理士　西澤　利夫
(72)発明者　石内　勝吾
沖縄県中頭郡西原町字千原１番地　国立大学法人琉球大学内

(54)【発明の名称】海馬機能の評価値算出方法、海馬機能の評価値算出システム、海馬機能の評価方法およびテストアイテムセット

(57)【要約】　（修正有）
【課題】被験者の海馬機能を簡便かつ確実に評価することができる海馬機能の評価値算出方法を提供する。
【解決手段】以下の工程により海馬機能の評価値を算出する。複数のテストアイテムを被験者に順次提示する試行を繰り返し行う工程と、この工程における各試行の終了後、被験者にその試行で提示されたテストアイテムが、（A）初めて提示されたテストアイテム、（B）従前の試行で提示されたテストアイテムと類似する別種のテストアイテム、（C）従前の試行で提示されたことがあるテストアイテムと同一のテストアイテム、のうちのいずれであるかを回答させる工程と、試行工程で提示したテストアイテムと回答工程で得られた回答結果とを比較して各試行に対する回答結果の正誤を判定する正誤判定工程と、正誤判定工程で得られた結果を集計して、前記（A）、（B）、（C）の各パターンごとに正答率を算出し、その正答率を海馬機能の評価値とする。
【選択図】図１

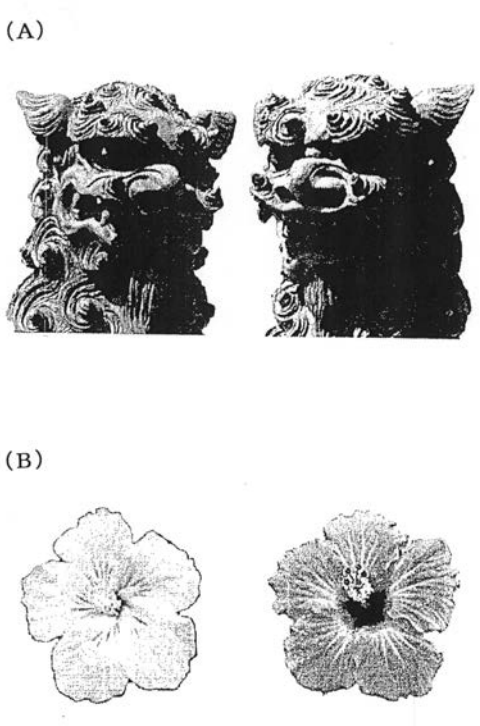

【特許請求の範囲】
【請求項１】
被験者の海馬機能の健全性を判断するための指標となる海馬機能の評価値を算出する方法であって、以下の工程：
複数のテストアイテムを被験者に順次提示する試行を繰り返し行う試行工程；
前記試行工程における各試行の終了後、被験者にその試行で提示されたテストアイテムが、以下の（A）～（C）のパターン、
（A）初めて提示されたテストアイテム
（B）従前の試行で提示されたテストアイテムと類似する別種のテストアイテム
（C）従前の試行で提示されたことがあるテストアイテムと同一のテストアイテム
のうちのいずれであるかを回答させる回答工程；
前記試行工程で提示したテストアイテムと前記回答工程で得られた回答結果とを比較して各試行に対する回答結果の正誤を判定する正誤判定工程；および
前記正誤判定工程で得られた結果を集計して、前記（A）、（B）、（C）の各パターンごとに正答率を算出し、その正答率を海馬機能の評価値として得る評価値算出工程
を含むことを特徴とする海馬機能の評価値算出方法。
【請求項２】
被験者の海馬機能の健全性を判断するための指標となる海馬機能の評価値を算出するためのシステムであって、
複数のテストアイテムを被験者に順次提示する試行を繰り返し実行するためのテストアイテム提示手段と、
各試行で提示するテストアイテムをテストアイテム提示手段に出力するテストアイテム出力手段と、
各試行の終了後、被験者が各試行で提示されたテストアイテムが、以下の（A）～（C）のパターン、
（A）初めて提示されたテストアイテム
（B）従前の試行で提示されたテストアイテムと類似する別種のテストアイテム
（C）従前の試行で提示されたことがあるテストアイテムと同一のテストアイテム
のうちのいずれであるかについての回答結果を入力する回答結果入力手段と、
回答結果入力手段を介して入力された回答結果を記憶する回答結果記憶手段と、
前記テストアイテム出力手段によって出力された各試行におけるテストアイテムと、前記回答結果記憶手段に記憶された回答結果とを比較して、各試行に対する回答結果の正誤を判定して、前記（A）、（B）、（C）の各パターンごとに正答率を算出し、その正答率を海馬機能の評価値として得る評価値算出手段、
を含むことを特徴とする海馬機能の評価値算出システム。
【請求項３】
被験者の海馬機能の健全性を評価するための海馬機能の評価方法であって、以下の工程：
複数のテストアイテムを被験者に順次提示する試行を繰り返し行う試行工程；
前記試行工程における各試行の終了後、被験者にその試行で提示されたテストアイテムが、以下の（A）～（C）のパターン、
（A）初めて提示されたテストアイテム
（B）従前の試行で提示されたテストアイテムと類似する別種のテストアイテム
（C）従前の試行で提示されたことがあるテストアイテムと同一のテストアイテム
のうちのいずれであるかを回答させる回答工程；
前記試行工程で提示したテストアイテムと前記回答工程でと同一のテストアイテム
のうちのいずれであるかを回答させる回答工程；
前記試行工程で提示したテストアイテムと前記回答工程で得られた回答結果とを比較して各試行に対する回答結果の正誤を判定する正誤判定工程；
前記回答工程で得られた回答結果の正誤を集計して、前記（A）、（B）、（C）の各パ

ターンごとに正答率を算出する正答率算出工程；
前記正答率算出工程で算出された被験者のパターン（B）の正答率を、健常者のパターン（B）の正答率（平均値±標準偏差）と比較する工程、
被験者の正答率が、健常者のパターン（B）の正答率の標準偏差の２倍以上低い場合に、海馬に疾患または損傷が生じていると評価する海馬機能評価工程；
を含むことを特徴とする海馬機能の評価方法。
【請求項４】
請求項１の海馬機能の評価値算出方法に使用されるテストアイテムのセットであって、30名以上の健常者のうちの85％～98％が同一であると判断するアイテム群からなる同一テストアイテムセットと、30名以上の健常者のうちの40％～50％が前記同一テストアイテムと類似しているが異なると判断するアイテム群からなる類似テストアイテムセットと、前記同一テストアイテムセットおよび類似テストアイテムセットとは異なると判断される単独のテストアイテム群からなる単独テストアイテムセットとを含むことを特徴とするテストアイテムセット。

【発明の詳細な説明】
【技術分野】
【０００１】
海馬機能の評価値算出方法、海馬機能の評価値算出システム、海馬機能の評価方法およびテストアイテムセットに関する。
【背景技術】
【０００２】
海馬は、学習と記憶に重要な役割を果たすことが知られており、その機能についての様々な研究が行われている。
【０００３】
例えば、非特許文献１には、遺伝子改変動物を用いて、海馬歯状回のＮＭＤＡ受容体が似ているが少し異なる事物に対する認識（pattern separation）に関与することが記載されている。非特許文献２には、新生神経細胞がpattern separationに関与し、成熟神経細胞がpattern completion(似ている物の形状の認識)に関与することが記載されている。
【０００４】
一方、特許文献１には、被験者にディスプレイに表示した一次画像と二次画像が同じであるか異なるかを回答してもらい、その回答結果から脳機能の活性度を計測する脳機能計測方法が記載されている。より具体的には、特許文献１の方法は、注視エリアが設けられた一次画像が順次、自動的に表示され、つづいて、これら一次画像に対して、注視エリア内の画像情報が同じまたは異なる二次画像が同様に順次、自動的に表示され、その指定注視エリアの画像を目視して、先に目視した一次画像と同じ画像か異なる画像かを回答させるものである。特許文献１の方法によれば、機能的磁気共鳴画像（fMRI）などの高価な装置を利用しなくても、簡便に、海馬などの機能の活性度を計測することができるとされている。
【先行技術文献】
【特許文献】
【０００５】
【特許文献１】特開2005－192637号公報
【非特許文献】
【０００６】
【非特許文献１】Science 317, 94-97, Jul6, 2007
【非特許文献２】Cell 149,188-201, March30,2012
【発明の概要】
【発明が解決しようとする課題】
【０００７】

非特許文献１、２に記載されているように、被験者の海馬機能を適確に評価するためには、pattern separationに関与する海馬の新生神経細胞の状態を把握することが重要であると考えられるが、特許文献１の脳機能計測方法は、注視エリアを設けた一次画像と二次画像が同じであるか異なるかを判断させるものであるため、主に被験者の一次記憶（最初に入る記憶の情報）についての検査が行われているに過ぎない。また、特許文献１の方法では、被験者が注視エリアを確認できるか否かの注意機能（前頭葉機能）が回答結果に大きく影響するため、海馬機能を評価することは難しいという問題がある。

【０００８】

本発明は、以上のとおりの事情に鑑みてなされたものであり、被験者の海馬機能を簡便かつ確実に評価することができる海馬機能の評価値算出方法、海馬機能の評価値算出システムおよび海馬機能の評価方法を提供することを課題としている。また、海馬機能の評価に利用されるテストアイテムを提供することを課題としている。

【課題を解決するための手段】

【０００９】

上記の課題を解決するために、本発明の海馬機能の評価値算出方法は、被験者の海馬機能の健全性を判断するための指標となる海馬機能の評価値を算出する方法であって、以下の工程：

複数のテストアイテムを被験者に順次提示する試行を繰り返し行う試行工程；

前記試行工程における各試行の終了後、被験者にその試行で提示されたテストアイテムが、以下の（A）～（C）のパターン、

（A）初めて提示されたテストアイテム

（B）従前の試行で提示されたテストアイテムと類似する別種のテストアイテム

（C）従前の試行で提示されたことがあるテストアイテムと同一のテストアイテム

のうちのいずれであるかを回答させる回答工程；

前記試行工程で提示したテストアイテムと前記回答工程で得られた回答結果とを比較して各試行に対する回答結果の正誤を判定する正誤判定工程；および

前記正誤判定工程で得られた結果を集計して、前記（A）、（B）、（C）の各パターンごとに正答率を算出し、その正答率を海馬機能の評価値として得る評価値算出工程

を含むことを特徴としている。

【００１０】

本発明の海馬機能の評価値算出システムは、被験者の海馬機能の健全性を判断するための指標となる海馬機能の評価値を算出するためのシステムであって、

複数のテストアイテムを被験者に順次提示する試行を繰り返し実行するためのテストアイテム提示手段と、

各試行で提示するテストアイテムをテストアイテム提示手段に出力するテストアイテム出力手段と、

各試行の終了後、被験者が各試行で提示されたテストアイテムが、以下の（A）～（C）のパターン、

（A）初めて提示されたテストアイテム

（B）従前の試行で提示されたことがあるテストアイテムと類似する別種のテストアイテム

（C）従前の試行で提示されたことがあるテストアイテムと同一のテストアイテム

のうちのいずれであるかについての回答結果を入力する回答結果入力手段と、

回答結果入力手段を介して入力された回答結果を記憶する回答結果記憶手段と、

前記テストアイテム出力手段によって出力された各試行におけるテストアイテムと、前記回答結果記憶手段に記憶された回答結果とを比較して、各試行に対する回答結果の正誤を判定して、前記（A）、（B）、（C）の各パターンごとに正答率を算出し、その正答率を海馬機能の評価値として得る評価値算出手段、

を含むことを特徴としている。

【００１１】

本発明の海馬機能の評価方法は、被験者の海馬機能の健全性を評価するための海馬機能の評価方法であって、以下の工程：
複数のテストアイテムを被験者に順次提示する試行を繰り返し行う試行工程；
前記試行工程における各試行の終了後、被験者にその試行で提示されたテストアイテムが、以下の（A）～（C）のパターン、
（A）初めて提示されたテストアイテム
（B）従前の試行で提示されたテストアイテムと類似する別種のテストアイテム
（C）従前の試行で提示されたことがあるテストアイテムと同一のテストアイテム
のうちのいずれであるかを回答させる回答工程；
前記試行工程で提示したテストアイテムと前記回答工程で得られた回答結果とを比較して各試行に対する回答結果の正誤を判定する正誤判定工程；
前記回答工程で得られた回答結果の正誤を集計して、前記（A）、（B）、（C）の各パターンごとに正答率を算出する正答率算出工程；
前記正答率算出工程で算出された被験者のパターン（B）の正答率を、健常者のパターン（B）の正答率の（平均値±標準偏差）と比較する工程、
被験者の正答率が、健常者のパターン（B）の正答率の標準偏差の２倍以上低い場合に、海馬に疾患または損傷が生じていると評価する海馬機能評価工程；
を含むことを特徴としている。

【００１２】

本発明のテストアイテムセットは、前記海馬機能の評価値算出方法に使用されるテストアイテムのセットであって、30名以上の健常者のうちの85％～98％が同一であると判断するアイテム群からなる同一テストアイテムセットと、30名以上の健常者のうちの40％～50％が前記同一テストアイテムと類似しているが異なると判断するアイテム群からなる類似テストアイテムセットと、前記同一テストアイテムセットおよび類似テストアイテムセットとは異なると判断される単独のテストアイテム群からなる単独テストアイテムセットとを含むことを特徴としている。

【発明の効果】

【００１３】

本発明の海馬機能の評価値算出方法、海馬機能の評価値算出システムによれば、被験者の海馬機能の健全性の指標となる評価値を簡便かつ確実に算出することができる。また、本発明の海馬機能の評価方法によれば、被験者の海馬に疾患または損傷が生じている否かや新生神経細胞の状態、放射線治療後の認知機能の回復経過、内分泌系代謝疾患、糖尿病、肥満患者の認知能力（海馬新生機能）を簡便かつ確実に評価することができる。さらに、本発明のテストアイテムによれば、海馬機能の評価値を簡便に得ることができる。

【図面の簡単な説明】

【００１４】

【図１】「類似する別種のテストアイテム」の具体例を示した図である。
【図２】本発明の海馬機能の評価値算出方法の一実施形態を例示した概要図である。
【図３】健常者１例（２５歳男子）のBOLD解析の結果および海馬機能の評価値（New、Lure、Sameの正答率（平均値±標準偏差））の結果を示す図である。
【図４】健常者、良性脳腫瘍患者、悪性脳腫瘍患者、悪性脳腫瘍放射線治療施行患者のNew、Lure、Sameの正答率の結果を示す図である。
【図５】被験者の左右の海馬に放射線を照射して治療した際の放射線量とLure正答率の関係を示す図である。
【図６】海馬のBOLD信号とLure正答率との関係を示す図である。
【図７】非定型髄膜腫の患者に対して、放射線化学療法を施行した例におけるNew、Lure、Sameの正答率とBOLD信号を示す図である。
【図８】悪性脳腫瘍（グリオーマ）の患者に対して、放射線化学療法を施行した例におけるNew、Lure、Sameの正答率とBOLD信号を示す図である。
【図９】左側頭葉神経膠芽腫の患者に対して放射線化学療法を施行後、薬剤による治療介

入した例におけるNew、Lure、Sameの正答率の変化を示す図である。

【発明を実施するための形態】

【００１５】

本発明の海馬機能の評価値算出方法は、被験者の海馬機能の健全性を判断するための指標となる海馬機能の評価値を算出する方法であって、以下の工程：

複数のテストアイテムを被験者に順次提示する試行を繰り返し行う試行工程；

前記試行工程における各試行の終了後、被験者にその試行で提示されたテストアイテムが、以下の（A）～（C）のパターン、

（A）初めて提示されたテストアイテム

（B）従前の試行で提示されたテストアイテムと類似する別種のテストアイテム

（C）従前の試行で提示されたことがあるテストアイテムと同一のテストアイテム

のうちのいずれであるかを回答させる回答工程；

前記試行工程で提示したテストアイテムと前記回答工程で得られた回答結果とを比較して各試行に対する回答結果の正誤を判定する正誤判定工程；

前記回答工程で得られた回答結果の正誤を集計して、前記（A）、（B）、（C）の各パターンごとに正答率を算出し、その正答率を海馬機能の評価値として得る工程；

を含む。

【００１６】

以下、本発明の海馬機能の評価算出方法の各工程について説明する。なお、本発明において「海馬」には、歯状回が含まれる。

【００１７】

試行工程は、複数のテストアイテムを被験者に順次提示する試行を繰り返し行う工程である。

【００１８】

テストアイテムとは、被験者が目視によって図柄などを記憶すべきアイテムをいい、例えば、図柄が表されたカード、立体物、画面上に表された画像などを例示することができる。したがって、被験者にテストアイテムを提示する方法、手段もテストアイテムの種類や被験者の状態などを考慮して適宜設定することができる。具体的には、例えば、テストアイテムが図柄が表されたカードである場合には、被験者に対し、カードを一枚づつ順次提示していく方法を採用することができる。このような複数のテストアイテムが一組のセットになったテストアイテムセットを利用することが好ましい。

【００１９】

試行工程における試行回数（テストアイテムの提示回数）やテストアイテムの提示時間、各試行間の時間的間隔などは、比較対象となる被験者の条件が同一であればよく、特に限定されない。例えば、試行回数（テストアイテムの提示回数）については、被験者の状態や難易度などを考慮して、例えば３０回～１５０回程度の範囲を例示することができる。

【００２０】

回答工程では、試行工程における各試行の終了後（１回のテストアイテムの提示後）、被験者にその試行で提示されたテストアイテムが、以下の（A）～（C）のパターン、

（A）初めて提示されたテストアイテム

（B）従前の試行で提示されたテストアイテムと類似する別種のテストアイテム

（C）従前の試行で提示されたことがあるテストアイテムと同一のテストアイテム

のうちのいずれであるかを回答させる。

【００２１】

すなわち、回答工程において被験者が正答するためには、従前の試行で提示されたテストアイテムの内容（図柄など）をすべて記憶し、現在提示されているテストアイテムとの比較によって、（A）～（C）のパターンを選択して回答する必要がある。したがって、試行回数（テストアイテムの提示数）が増えるに従って、被験者が記憶すべきテストアイテムの種類は増えることになるため回答の難易度は高まることになる。また、テストアイテ

ムの図柄の類似性や、テストアイテムの提示の順番などによっても回答の難易度は変わり得るため、試行工程におけるテストアイテムの提示条件を統一して、予め基準となる健常者の正答率の平均値を得ておく必要がある。

【００２２】

回答工程における回答形式は特に限定されず、被験者の口頭での回答を第三者が記録してもよいし、被験者自身に回答用紙に回答を記入させたり、コンピュータに回答を入力させるなどしてもよい。

【００２３】

なお、パターン（B）の「類似する別種のテストアイテム」とは、例えば、図柄が表されたテストアイテムの場合では、従前の試行で提示されたテストアイテムの図柄に対して、図柄の一部が欠損または付加されているもの、図柄の外形が同一形状であるが色彩が異なるもの、図柄が左右対称に表されているものなどを例示することができる。したがって、このようなテストアイテムを複数含むテストアイテムセットは、例えば、30名以上の健常者のうちの85％～98％が同一であると判断するアイテム群からなる同一テストアイテムセットと、30名以上の健常者のうちの40％～50％が同一テストアイテムと類似しているが異なると判断するアイテム群からなる類似テストアイテムセットと、同一テストアイテムセットおよび類似テストアイテムセットとは異なると判断される単独のテストアイテム群からなる単独テストアイテムセットによって構成することができる。テストアイテムの類似性については、このような基準に基づいて作成されたものを使用することができる。なお、ここでいう「健常者」とは、脳の海馬機能に疾患や損傷などによる機能低下が確認されない者をいう。

【００２４】

図１は、「類似する別種のテストアイテム」の具体例を示した図である。図１（Ａ）に例示したテストアイテムとしてのカードの左右の図柄では、シーサーの向きと口の開閉状態が異なっており、両図柄を有するカードは互いに類似するテストアイテムとして設計されている。また、図１（Ｂ）に例示したカードの図柄では、略同一の形の花であるが、その色が異なっており、両図柄を有するカードは互いに類似するテストアイテムとして設計されている。

【００２５】

正誤判定工程では、試行工程で提示したテストアイテムと回答工程で得られた回答結果とを比較して各試行に対する回答結果の正誤を判定する。回答結果の正誤を判定する方法は特に限定されず、例えば第三者が被験者の回答の正誤を判定してもよいし、コンピューターなどによって自動的に回答の正誤を判定してもよい。正誤判定工程では、試行工程で提示したテストアイテムのパターン（A）（B）（C）と、回答工程で得られた被験者の回答とが一致するか否かを確認すればよく、回答の正誤を判定するのは容易である。

【００２６】

さらに、本発明の海馬機能の評価値算出方法における試行工程、回答工程、正誤判定工程について、図２に示す具体例を用いて説明する。図２は、本発明の海馬機能の評価値算出方法の一実施形態を例示した概要図であり、テストアイテムとして図柄が表されたカードを使用する実施形態を例示している。

【００２７】

以下、便宜的に、（A）初めて提示されたテストアイテムを「New」、（B）従前の試行で提示されたテストアイテムと類似する別種のテストアイテムを「Lure」、（C）従前の試行で提示されたことがあるカードと同一のテストアイテムを「Same」と記載する。

【００２８】

図２に示したように、試行工程で被験者に提示するカードには各種の図柄が描かれており、一組のテストアイテムセットを構成する。

【００２９】

第１試行では、図２中のカード１を提示する。カード１には三味線の図が描かれており、被験者はこの図柄を記憶する。第１試行であるため、被験者は「New」を回答すること

が求められる。

【００３０】

第２試行では、図２中のカード２を提示する。カード２には飲料缶の図が描かれており、被験者はこの図柄を記憶する。この図柄は、第１試行で提示されたカードの図柄と異なる新しいものであるため、被験者は「New」を回答することが求められる。

【００３１】

第３試行では、図２中のカード３を提示する。カード３には青色のハイビスカスの図が描かれており、被験者はこの図柄を記憶する。この図柄は、第１、第２試行で提示されたカードの図柄と異なる新しいものであるため、被験者は「New」を回答することが求められる。

【００３２】

第４試行では、図２中のカード４を提示する。カード４には、右方向を向き、口を閉じたシーサーの図が描かれており、被験者はこの図柄を記憶する。この図柄は、第１～第３試行で提示されたカードの図柄と異なる新しいものであるため、被験者は「New」を回答することが求められる。

【００３３】

第５試行では、図２中のカード５を提示する。カード５にはリンゴの図が描かれており、被験者はこの図柄を記憶する。この図柄は、第１～第４試行で提示されたカードの図柄と異なる新しいものであるため、被験者は「New」を回答することが求められる。

【００３４】

第６試行では、図２中のカード６を提示する。カード６には、第１試行のカード１と同じ三味線の図が描かれているため、被験者は「Same」を回答することが求められる。

【００３５】

第７試行では、図２中のカード７を提示する。カード７には、ガラス製容器の図が描かれており、被験者はこの図柄を記憶する。この図柄は、第１～第６試行で提示されたカードの図柄と異なる新しいものであるため、被験者は「New」を回答することが求められる。

【００３６】

第８試行では、図２中のカード８を提示する。カード８には、第５試行のカード５と同じリンゴの図が描かれているため、被験者は「Same」を回答することが求められる。

【００３７】

第９試行では、図２中のカード９を提示する。カード９には、第３試行のカード３と外形がほぼ同じだが色が赤色のハイビスカスの図が描かれているため、被験者は「Lure」を回答することが求められる。

【００３８】

第１０試行では、図２中のカード１０を提示する。カード１０には、ゴーヤの図が描かれており、被験者はこの図柄を記憶する。この図柄は、第１～第９試行で提示されたカードの図柄と異なる新しいものであるため、被験者は「New」を回答することが求められる。

【００３９】

第１１試行では、図２中のカード１１を提示する。カード１１にはアジサイの図が描かれており、被験者はこの図柄を記憶する。この図柄は、第１～第１０試行で提示されたカードの図柄と異なる新しいものであるため、被験者は「New」を回答することが求められる。

【００４０】

第１２試行では、図２中のカード１２を提示する。カード１２には、第４試行のカード４のシーサーとは向きが異なり、かつ、口が開いているシーサーの図が描かれているため、被験者は「Lure」を回答することが求められる。

【００４１】

本発明の海馬機能の評価値算出方法では、このような試行を繰り返し行い（試行工程）

、被験者に、各試行の回答をパターン（A）：New、パターン（B）：Lure、パターン（C）：Sameのいずれかで回答させて（回答工程）、その回答結果を正誤判定をする（正誤判定工程）。

【００４２】

さらに、評価値算出工程では、正誤判定工程で得られた回答結果の正誤を集計して、（A）、（B）、（C）の各パターンごとに正答率を算出し、その正答率を海馬機能の評価値として得る。

【００４３】

正答率（％）は、（A）、（B）、（C）の各パターンごとの正答数を、各パターンごとの提示回数で割ることで算出され、この数値が海馬機能の評価値となる。健常者の正答率（海馬機能の評価値）の平均を算出する場合には、「平均値±標準偏差」で表すことができる。

【００４４】

本発明の海馬機能の評価方法では、健常者の海馬機能の評価値（（A）、（B）、（C）の各パターンごとの正答率）の平均を予め実験によって得ておき、この評価値（正答率）と被験者の海馬機能の評価値（正答率）との比較によって、被験者の海馬機能の健全性を評価することができる。

【００４５】

本発明の海馬機能の評価方法では、上記の海馬機能の評価値算出方法に加え、被験者のパターン（B）の正答率を、健常者のパターン（B）の正答率の平均（平均値±標準偏差）と比較する工程と、被験者の正答率が、健常者のパターン（B）の正答率の標準偏差の２倍（2SD）以上低い場合に、海馬に疾患または損傷が生じていると評価する工程を含む。

【００４６】

本発明者による検証では、本発明の海馬機能の評価値算出方法で得られる海馬機能の評価値は、健常者におけるパターン（A）の評価値（平均値±標準偏差（ＳＤ））は96±3、パターン（B）の評価値は47±19、パターン（C）の評価値は89±10の値を得ている。この場合、例えば、それぞれの評価値が平均より２ＳＤ（標準偏差ＳＤの２倍）以上に低下している場合（例えば、パターン（B）の評価値では、10未満の場合）には、海馬神経新生能障害と評価することができる。同様に、パターン（C）の評価値が70以下の場合には、数週間に及ぶ海馬神経新生能障害であると評価することができる。さらに、パターン（A）の評価値が90未満では、１カ月以上に及ぶ海馬神経新生能障害であると評価することができる。

【００４７】

海馬神経細胞では、歯状回部で新生された（young neuron）細胞が、似て非なるものを識別するため、海馬神経細胞にける新生機能の低下傾向がある場合には、まずパターン（B）の評価値の低下が確認される。新生海馬神経細胞は、数週間で成熟神経細胞に分化してyoung adult neuronになるが、この細胞機能がパターン（C）の評価値に反映される。さらに、海馬神経細胞にける新生機能が継続して１カ月以上傷害されるとold neuronの機能障害が機能障害をきたし、パターン（A）の評価値の低下を招くと考えられる。

【００４８】

本発明の海馬機能の評価値算出方法で得られた評価値によれば、fMRIなどの装置を使用なくとも、海馬機能に影響する疾患や環境について簡便かつ確実に評価することができる。具体的には、本発明の海馬機能の評価値算出方法で得られた評価値によれば、脳卒中、頭部外傷、ハンチンソン病、ストレス、うつ病、パーキンソン病、統合失調症、アルツハイマー型認知症などの病態をリアルタイムで簡便に評価することができる。このため、脳の病気の進行の程度、治療効果の判定、鑑別などに有用である。このような評価では、数値化された海馬機能の評価値（回答の正答率）によって行うことが可能であるため、必ずしも医療従事者による専門的知識や技術が必要とされない。

【００４９】

さらに、本発明者は、肥満や糖尿病、内分泌疾患においても海馬機能の低下が確認され

ることを新たに見出している。したがって、本発明の海馬機能の評価値算出方法によって得られた被験者の評価値を、健常者の海馬機能の評価値と比較することで、肥満患者の認知能力、糖尿病、内分泌代謝疾患の治療や管理に有効利用することができる。

【００５０】

また、本発明者は、放射線治療を施した患者では認知機能障害が誘発されており、本発明の海馬機能の評価値算出方法によって得られた被験者の評価値によって、治療介入による海馬新生機能の回復経過を評価できることを確認している。

【００５１】

次に、本発明の海馬機能の評価値算出システムについて説明する。本発明の海馬機能の評価値算出システムは、本発明の海馬機能の評価値算出方法を自動化して行うものである。したがって、上記の海馬機能の評価値算出方法と共通する内容については、説明を省略する。

【００５２】

本発明の海馬機能の評価値算出システムは、被験者の海馬機能の健全性を判断するための指標となる海馬機能の評価値を算出するためのシステムであって、

複数のテストアイテムを被験者に順次提示する試行を繰り返し実行するためのテストアイテム提示手段と、

各試行で提示するテストアイテムをテストアイテム提示手段に出力するテストアイテム出力手段と、

各試行の終了後、被験者が各試行で提示されたテストアイテムが、以下の（A）～（C）のパターン、

（A）初めて提示されたテストアイテム

（B）従前の試行で提示されたことがあるテストアイテムと類似する別種のテストアイテム

（C）従前の試行で提示されたことがあるテストアイテムと同一のテストアイテム

のうちのいずれであるかについての回答結果を入力する回答結果入力手段と、

回答結果入力手段を介して入力された回答結果を記憶する回答結果記憶手段と、

前記テストアイテム出力手段によって出力された各試行におけるテストアイテムと、前記回答結果記憶手段に記憶された回答結果とを比較して、各試行に対する回答結果の正誤を判定して、前記（A）、（B）、（C）の各パターンごとに正答率を算出し、その正答率を海馬機能の評価値として得る評価値算出手段、

を含む。

【００５３】

テストアイテム提示手段は、例えばディスプレイなどを例示することができ、ディスプレイ上に表示される画像によってテストアイテムを表示する形態のものを例示することができる。

【００５４】

テストアイテム出力手段は、各試行で提示するテストアイテムをテストアイテム提示手段に出力して表示する。テストアイテム出力手段は、予め設定されたテストアイテムの提示パターンを実行して表示するためのシステムなどを例示することができる。

【００５５】

回答結果入力手段は、被験者がテストアイテム提示手段によって提示されたテストアイテムを確認し、自身の記憶に照らして回答を入力するための手段である。具体的な実施形態は特に限定されないが、例えば、ボタンを押して回答を入力するものや、ディスプレイ（テストアイテム提示手段）上においてタッチパネル形式で入力するものなどを例示することができる。

【００５６】

回答結果記憶手段は、回答結果入力手段を介して入力された回答結果を記憶する記憶媒体（メモリー）などを例示することができる。

【００５７】

評価値算出手段は、テストアイテム出力手段によって出力された各試行におけるテストアイテムと、前記回答結果記憶手段に記憶された回答結果とを比較して自動的に正誤を判定し、（A）、（B）、（C）の各パターンごとに正答率を算出するものであり、公知の演算処理機などを例示することができる。

【００５８】

このような海馬機能の評価値算出システムによれば、自動的に被験者の海馬機能の評価値を得ることができるため、極めて簡便である。

【００５９】

本発明の海馬機能の評価値算出方法、海馬機能の評価値算出システム、海馬機能の評価方法およびテストアイテムセットは、以上の実施形態に限定されることはない。

【００６０】

以下、本発明の海馬機能の評価値算出方法および海馬機能の評価方法について実施例とともにより詳細に説明するが、本発明の海馬機能の評価値算出方法および海馬機能の評価方法は、以下の実施例に何ら限定されるものではない。

【実施例】

【００６１】

＜実施例１＞海馬機能の評価値算出

（１）手順

図柄が描かれたカード（テストアイテム）１０８枚を用意し、被験者に一枚ずつ提示する試行を繰り返し行い、各試行ごとに、被験者に、「初めて提示されたもの（New）」、「従前に提示されたことがあるものと似ているが異なるもの（Lure）」、「従前に提示されたことがあるものと全く同じもの（Same）」のいずれであるか回答させた。被験者の回答は、「初めて提示されたもの（New）」、「従前に提示されたことがあるものと似ているが異なるもの（Lure）」、「従前に提示されたことがあるものと全く同じもの（Same）」の３種の回答カードを指指して選択させ、被験者の選択回答を記録用紙に記入した。この記録用紙には、カードの提示順序、カードの種類、正答カード（Correct answer）、被験者の反応を記入する欄を設け、被験者がどのカードが提示された時に正答または誤答したかを簡便に記録できるものとした。その際、回答の正誤に関するフィードバックは行わなかった。また、１０８枚のカードは所定の順序で提示されるものとし、すべての試行の所要時間を約７分に設定した。なお、以下の実施例においても同様の手順で実験を行った。

【００６２】

被験者は、健常者３６名、良性脳腫瘍患者３１名、悪性脳腫瘍患者１０名、悪性脳腫瘍放射線治療施行患者１３名とした。また、悪性脳腫瘍放射線治療施行患者の治療放射線量は、22.7±18.3Gy（from 10 to 60Gy）とした。

【００６３】

さらに、被験者の海馬の状態は、機能的磁気共鳴画像（fMRI）によるBOLD（blood oxygenation level dependent）解析によって確認した。BOLD解析によって、脳内の血液中酸素量の変化に伴う磁化率の変動をとらえることができ、海馬の経時的変化の評価をすることができる。

（２）結果

図３に健常者１例（２５歳男子）のBOLD解析の結果および海馬機能の評価値（New、Lure、Sameの正答率（平均値±標準偏差））の結果を示す。図３に示したように、BOLD曲線は、開始２秒で下向きのピークをとり、５-６秒目に最初の上向きのピークをとった後オーバーシュートしていることが確認される。また、この健常者のNew、Lure、Sameの正答率は、それぞれ93%、44%および81%であり、他の健常者の平均値と比較して正常範囲内であることが確認された。

【００６４】

図４に、健常者３６名、良性脳腫瘍患者３１名、悪性脳腫瘍患者１０名、悪性脳腫瘍放射線治療施行患者１３名のNew、Lure、Sameの正答率の結果を示す。

【００６５】
図４に示したように、健常者３６名のNew、Lure、Sameの正答率（平均値±標準偏差）は、New：96±3、Lure：47±19、Same：89±10であった。良性脳腫瘍患者３１名のNew、Lure、Sameの正答率（平均値±標準偏差）は、New：93±8、Lure：43±21、Same：86±22であった。悪性脳腫瘍患者１０名のNew、Lure、Sameの正答率（平均値±標準偏差）は、New：95±4、Lure：38±19、Same：86±19であった。悪性脳腫瘍放射線治療施行患者１３名のNew、Lure、Sameの正答率（平均値±標準偏差）は、New：93±8、Lure：25±27、Same：81±26であった。
【００６６】
Lureの評価値について、健常者３６名、良性脳腫瘍患者３１名、悪性脳腫瘍患者１０名と、悪性脳腫瘍放射線治療施行患者１３名との間に有意差が確認された。悪性脳腫瘍放射線治療施行患者は、海馬（海馬歯状回）の新生機能が低下しているため、Lureの評価値は、海馬歯状回の神経細胞の新生能力または新生機能を反映していることが確認された。
【００６７】
＜実施例２＞海馬放射線治療とLure正答率
図５に、被験者の左右の海馬に放射線を照射して治療した際の放射線量とLure正答率の関係を示す。図５に示したように、多くの被験者において、海馬放射線治療によってLureの正答率が低下している。すなわち、Lureの評価値は、海馬歯状回の神経細胞の新生能力または新生機能を反映していることが確認された。
【００６８】
＜実施例３＞BOLD信号とLure正答率との関係
実施例１における被験者である健常者３６名、良性脳腫瘍患者３１名、悪性脳腫瘍患者１０名、悪性脳腫瘍放射線治療施行患者１３名について、fMRIを利用して、海馬のBOLD信号とLure正答率との関係を検討した。
【００６９】
結果を図６に示す。図６に示したように、健常者と良性脳腫瘍患者は、BOLD信号とLure正答率の間に相関関係があり、BOLD信号が強いほどLure正答率が高く、逆に、BOLD信号が弱いほどLure正答率が低いことが確認された。一方で、悪性脳腫瘍患者については、相関関係の傾向は弱まり、放射線照射後（悪性脳腫瘍放射線治療施行患者）では、BOLD信号とLure正答率の間に相関関係が消失することが確認された。すなわち、Lure正答率は、海馬機能の状態（海馬歯状回の神経細胞の新生能力または新生機能）を反映していることが確認された。
【００７０】
＜実施例４＞New、Lure、Sameの正答率とBOLD信号の時間軸変化の具体例
（１）図７は、非定型髄膜腫の患者（６１歳）に対して、放射線化学療法を施行した例におけるNew、Lure、Sameの正答率とBOLD信号を示している。この例では、放射線化学療法の前の段階において、BOLD信号は、正常型であり、Lure正答率が56.3％と高く、海馬機能がほぼ正常に維持されていることが確認される。その後、14Gyの放射線治療によってBOLD信号は、初回陽性波ピーク値の低下を来たし、Lure正答率が0％になり、海馬の新生機能が抑制されていることが確認されるが、治療前のLure正答率が56.3％と高かったため、NewとSameの正答率はすぐには低下しない。46Gyの放射線治療終了後には、Lure正答率が回復し始め（Lure正答率：12.5％）、放射線治療後３か月後では、New、Lure、Sameの正答率が正常化していることが確認される。
（２）図８は、悪性脳腫瘍（グリオーマ）の患者（６２歳）に対して、放射線化学療法を施行した例におけるNew、Lure、Sameの正答率とBOLD信号を示している。この例では、放射線化学療法の前の段階において、BOLD信号は、健常者と異なる像を呈しており、また、Lure正答率：6.3％、Same正答率：0％であり、海馬機能が非常に低下していることが分かる。そして、放射線化学療法の開始後（14Gy）には、BOLD信号は、２相性の陰性波であり、Lure正答率が0％なったため、海馬の神経新生機能を支援する薬剤を投与したところ、５週間後にはBOLD信号は、正常化するとともに、Lure正答率が37.5％まで正常化した（薬

剤によるneuromodulation）。放射線治療の終了後に化学療法を３回施したことで、放射線治療の終了後３カ月ではBOLD信号は、再び健常者と異なる像を呈するとともに、Lure正答率が再び0％になったが、Lureの正答率が37.5％を示していた時点（放射線治療開始後５週間後）での海馬の新生神経細胞がSameを認識する機能を担っているため、Same正答率が正常化したと考えられる。

（３）図９は、左側頭葉神経膠芽腫の患者（４７歳）に対して放射線化学療法を施行後、薬剤による治療介入した例におけるNew、Lure、Sameの正答率の変化を示している。この例では、手術後にLure正答率およびSame正答率が低下し、16Gyの放射線治療後にはSame正答率が回復する一方で、Lure正答率は低下している。この時、薬剤（メマンチン酸塩）による治療介入を行ったところ、Lure正答率が正常化したことが確認された。

（４）以上の通り、本発明の海馬機能の評価値算出方法によって得られた評価値を利用することで、放射線治療によって海馬機能が低下した患者の認知機能の状態（海馬新生機能の回復経過）をリアルタイムで簡便に診断することができる。

【００７１】

＜実施例５＞下垂体線腫の患者および糖尿病の患者のNew、Lure、Sameの正答率

（１）下垂体線腫の患者９名に対し、本発明の方法で海馬機能の評価値を算出した。その結果、New、Lure、Sameの正答率（平均値±標準偏差）は、New：77±32、Lure：20±17、Same：91±9であった。下垂体線腫の患者の場合、健常者の評価値（正答率）と比較すると、Newの正答率は２標準偏差、Lureの正答率は１標準偏差低下している。

（２）糖尿病の患者（６名、肥満患者を含む）に対し、本発明の方法で海馬機能の評価値を算出した。その結果、評価値（New、Lure、Sameの正答率（平均値±標準偏差））は、New：93±6、Lure：23±17、Same：80±10であった。糖尿病の患者の場合、健常者の評価値（正答率）と比較すると、Lureの正答率は１標準偏差、低下している。

（３）このように、本発明の方法で算出した海馬機能の評価値によれば、内分泌系代謝疾患、糖尿病、肥満の患者の認知能力（海馬新生機能）を簡便に評価することができる。

【図１】

(A)

(B)

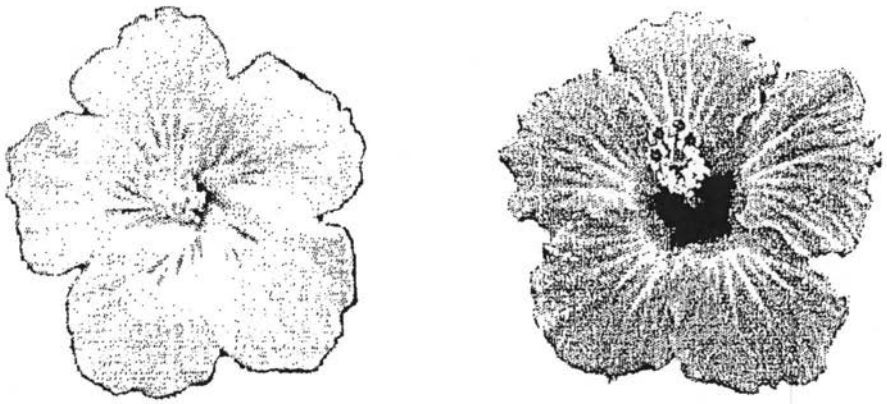

【図２】

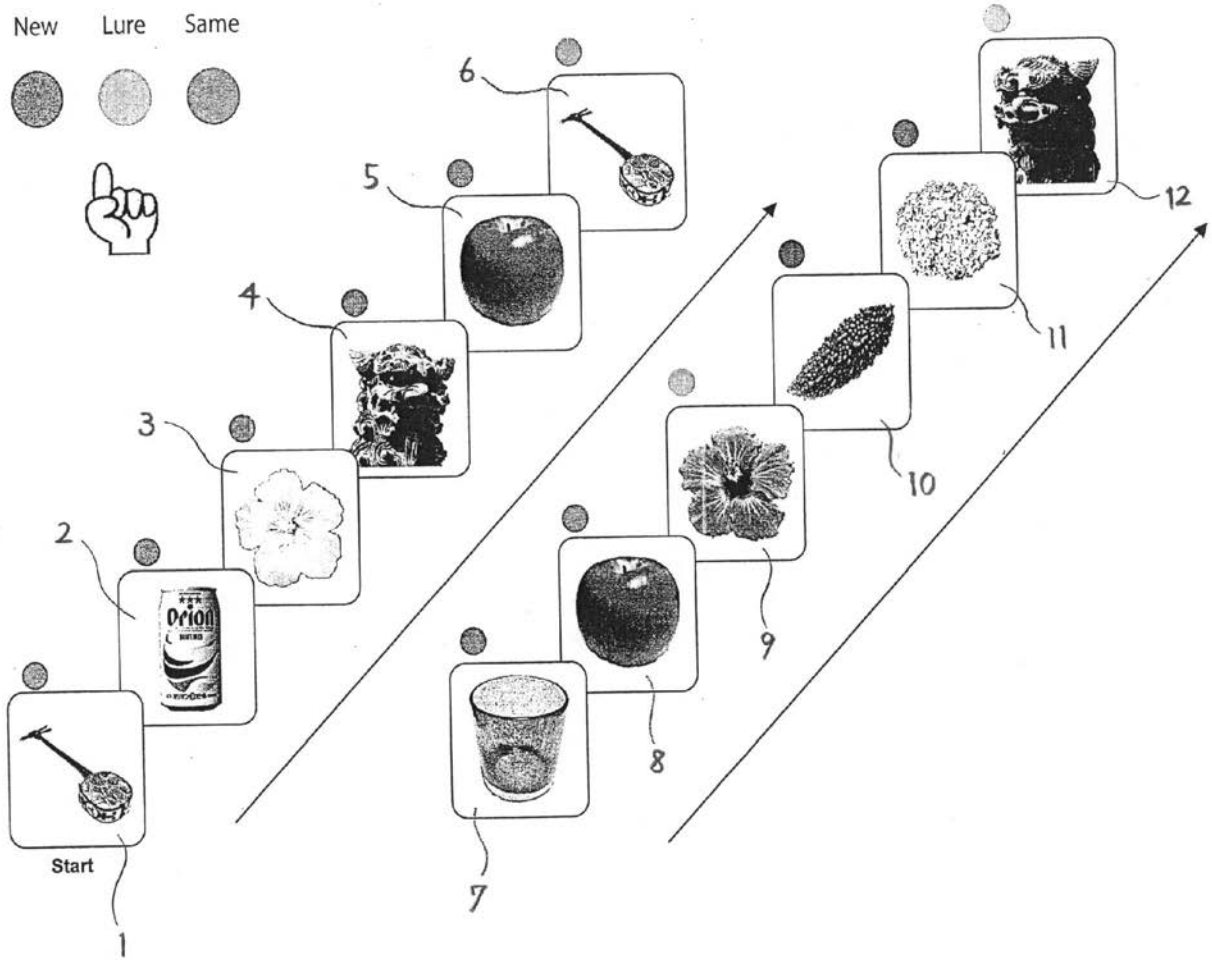

【図３】

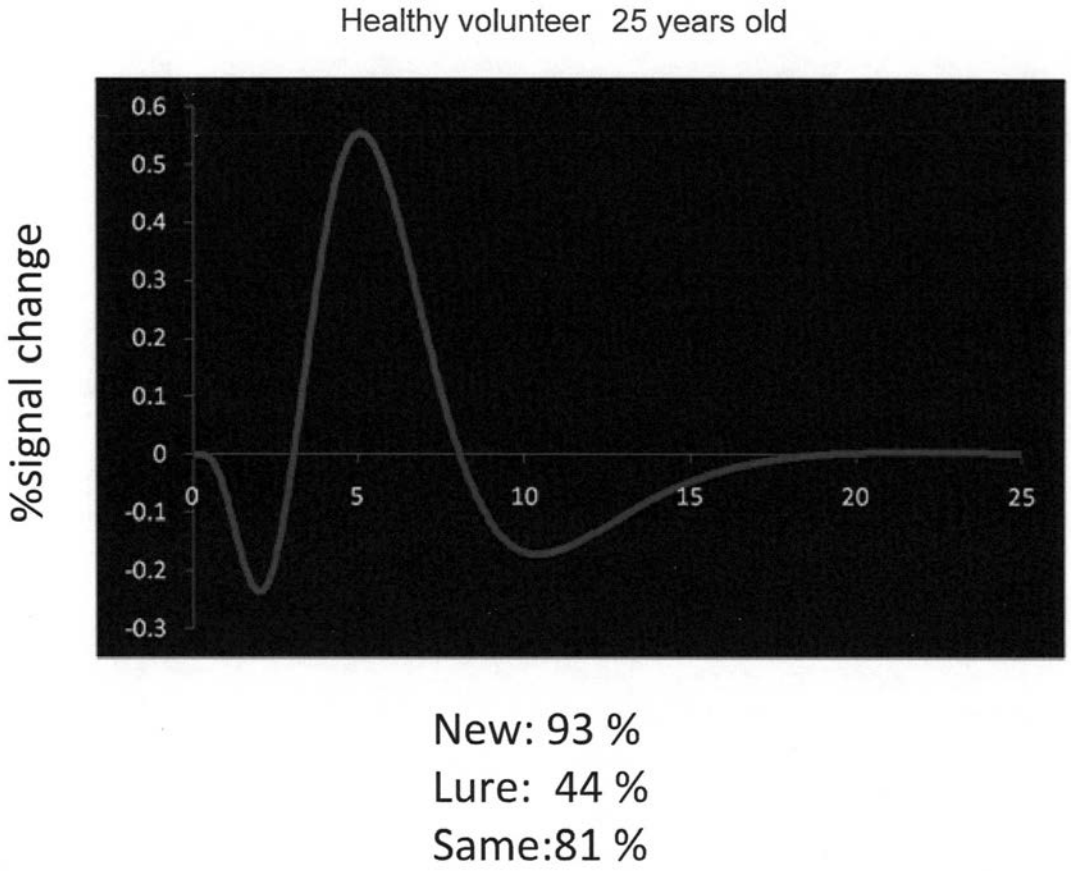
Healthy volunteer 25 years old
%signal change
0.6
0.5
0.4
0.3
0.2
0.1
0
-0.1
-0.2
-0.3
0
5
10
15
20
25
New: 93 %
Lure: 44 %
Same:81 %

【図４】

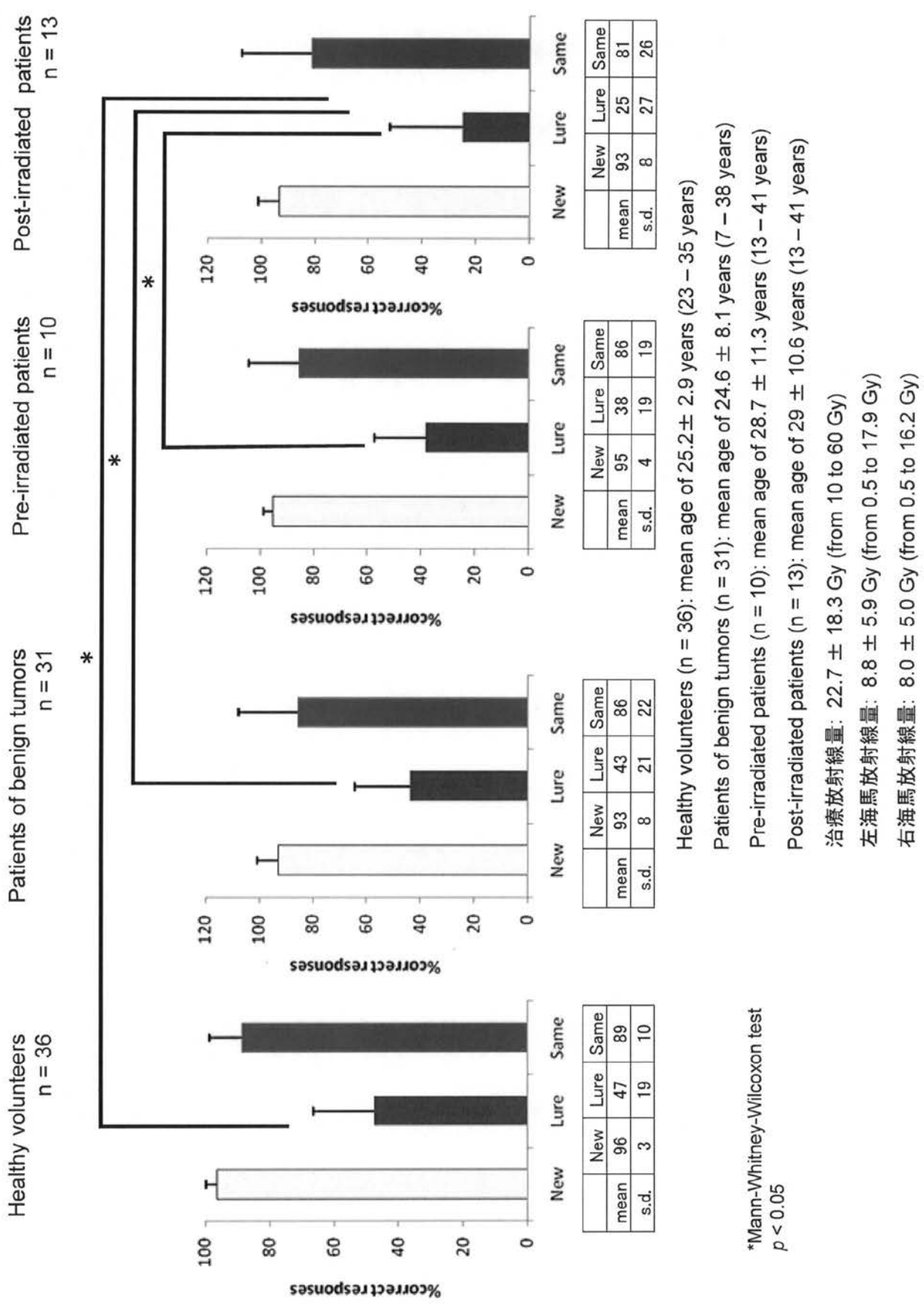

	New	Lure	Same
mean	96	47	89
s.d.	3	19	10

	New	Lure	Same
mean	93	43	86
s.d.	8	21	22

	New	Lure	Same
mean	95	38	86
s.d.	4	19	19

	New	Lure	Same
mean	93	25	81
s.d.	8	27	26

Healthy volunteers (n = 36): mean age of 25.2± 2.9 years (23 – 35 years)

Patients of benign tumors (n = 31): mean age of 24.6 ± 8.1 years (7 – 38 years)

Pre-irradiated patients (n = 10): mean age of 28.7 ± 11.3 years (13 – 41 years)

Post-irradiated patients (n = 13): mean age of 29 ± 10.6 years (13 – 41 years)

治療放射線量: 22.7 ± 18.3 Gy (from 10 to 60 Gy)

左海馬放射線量: 8.8 ± 5.9 Gy (from 0.5 to 17.9 Gy)

右海馬放射線量: 8.0 ± 5.0 Gy (from 0.5 to 16.2 Gy)

*Mann-Whitney-Wilcoxon test
$p < 0.05$

【図５】

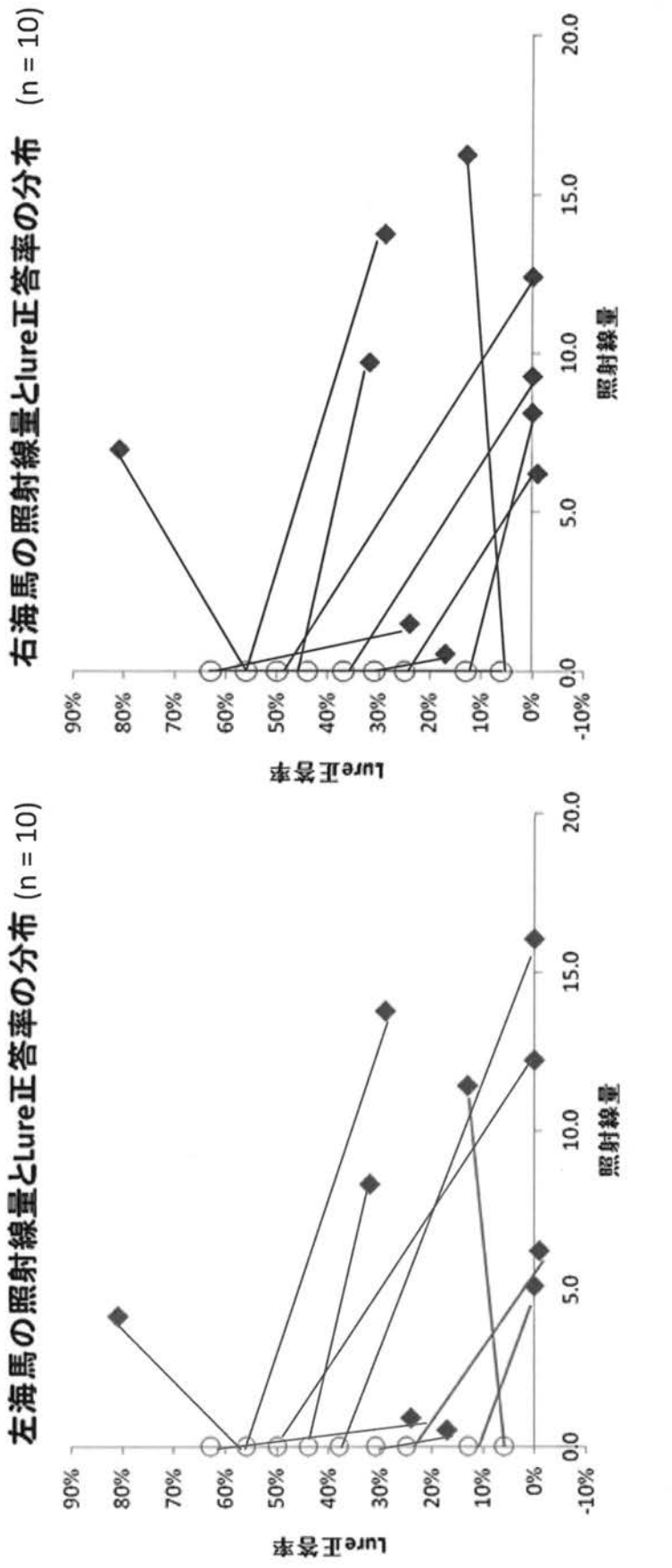
右海馬の照射線量とlure正答率の分布 (n = 10)
Lure正答率
90%
80%
70%
60%
50%
40%
30%
20%
10%
0%
-10%
0.0
5.0
10.0
15.0
20.0
照射線量
左海馬の照射線量とlure正答率の分布 (n = 10)
Lure正答率
90%
80%
70%
60%
50%
40%
30%
20%
10%
0%
-10%
0.0
5.0
10.0
15.0
20.0
照射線量

【図６】

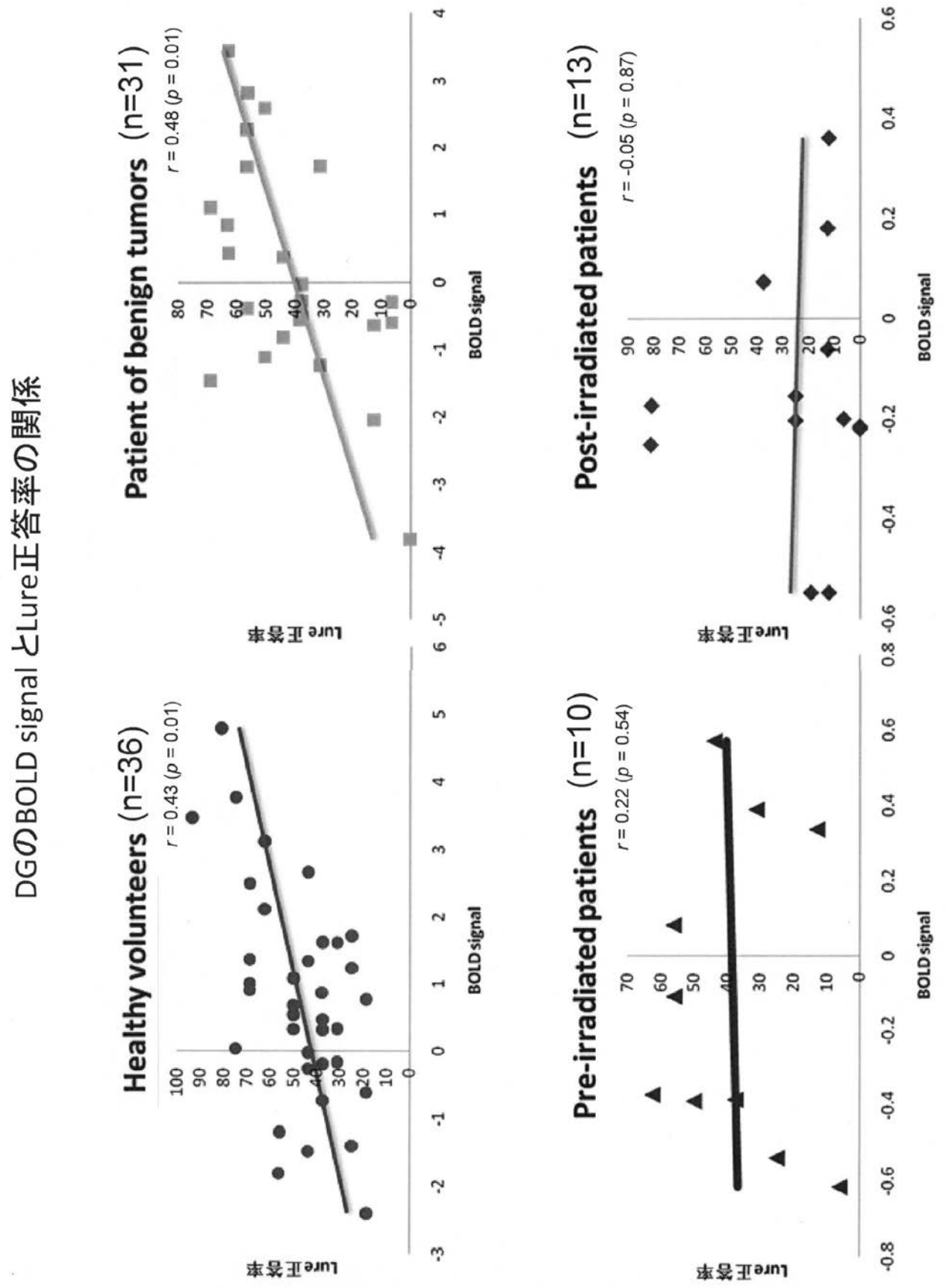
DGのBOLD signal とLure正答率の関係
Healthy volunteers (n=36)
r = 0.43 (p = 0.01)
Patient of benign tumors (n=31)
r = 0.48 (p = 0.01)
Pre-irradiated patients (n=10)
r = 0.22 (p = 0.54)
Post-irradiated patients (n=13)
r = -0.05 (p = 0.87)
Lure正答率
BOLD signal

【図７】

61 yrs female atypical meningioma
Pre-operation
14Gy post-irradiation
46Gy Post-irradiation
After 3months of irradiation
%signal change
New: 89.5 % (1SD ↓)
Lure: 56.3 %
Same: 62.5 % (2SD ↓)
New: 93.4 %
Lure: 0 % (2SD ↓)
Same: 93.8 %
New: 88.2 %(2SD ↓)
Lure: 12.5 % (1SD ↓)
Same: 81.3 %
New: 92.1 %
Lure: 25 %
Same: 93.8 %

【図８】

62 yrs Gliomatosis cerebri (Lt temporal, thalamus)
Pre-operation
14Gy post-irradiation
56Gy Post-irradiation
After 3months of irradiation
%signal change
New:100%
Lure:6.3% (2SD ↓)
Same:0%
New: 81.6% (2SD ↓)
Lure: 0% (2SD ↓)
Same: 0% (2SD ↓)
New:100 %
Lure: 37.5 %
Same: 0 %(2SD ↓)
New:97.4 %
Lure: 0 % (2SD ↓)
Same: 87.5 %

【図９】

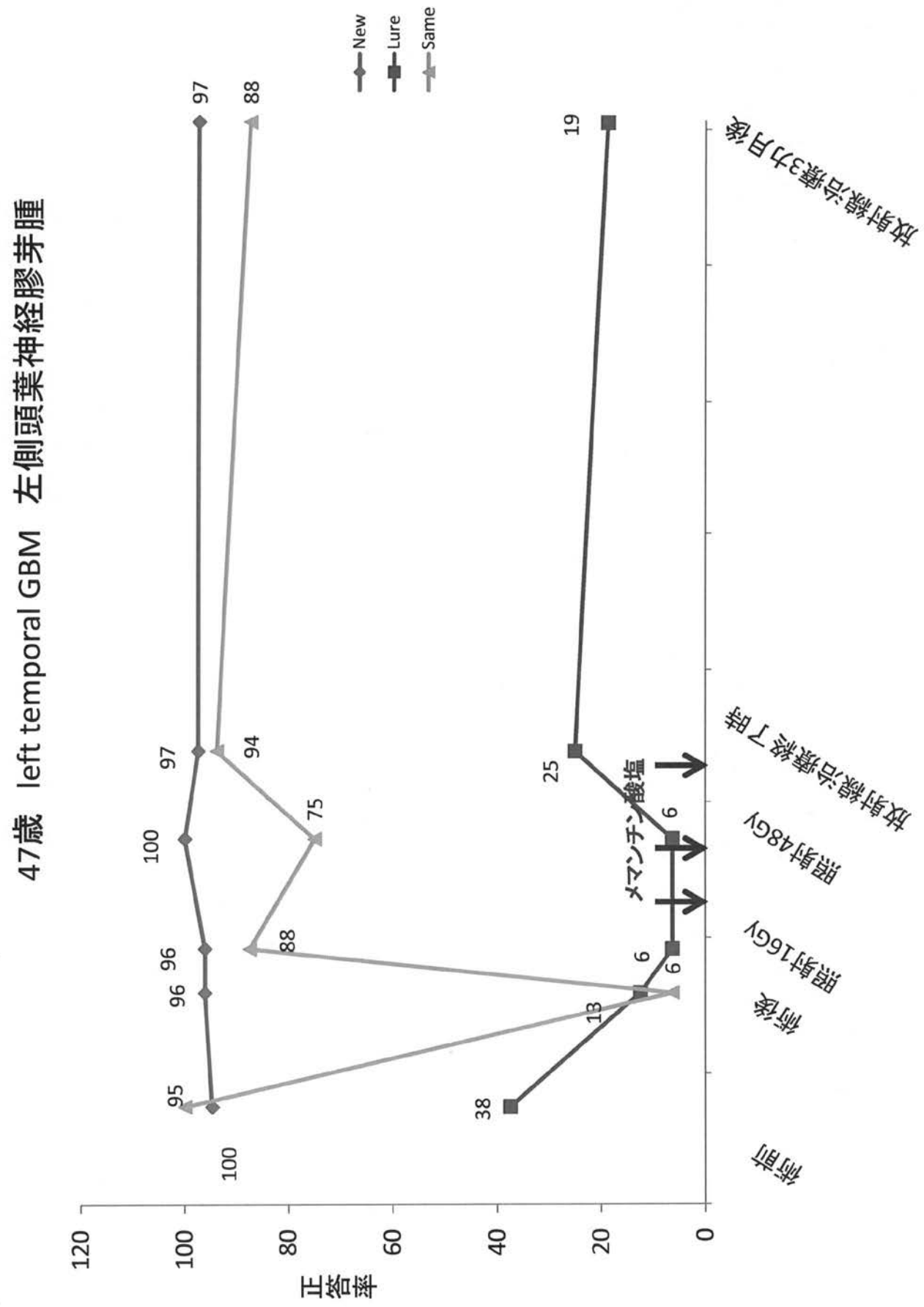
47歳 left temporal GBM 左側頭葉神経膠芽腫
New
Lure
Same
正答率
120
100
80
60
40
20
0
97
88
97
94
100
75
96
88
96
95
100
19
25
38
13
6
6
6
メマンチン塩酸塩
術前
術後
照射16Gy
照射48Gy
放射線治療終了時
放射線治療3カ月後

BRAIN NURSING ブレインナーシング

第31巻2号　2015年2月1日発行

MC メディカ出版

第2特集

4 経頭蓋直流電気刺激法と脳腫瘍手術

石内勝吾（いしうち・しょうご）琉球大学大学院医学研究科脳神経外科教授

経頭蓋直流電気刺激法とは

1. 脳の可塑性

経頭蓋直流電気刺激法とは、微弱な1～5mAの直流電流を頭皮上に貼った電極から流すことで、脳の可塑性を誘導して治療効果を高めようとする方法です。ヒトの脳は病気になると、状況に応じて臨機応変に、周辺の正常な脳組織が失われた機能を取り戻そうとする性質があります。これを脳の可塑性といいます。

2. 治療方法

治療は簡単かつ安全に行えます。治療する部位に5×5cmまたは5×7cmの大きさの電極を貼ります（**図1、2**）。そこへ刺激装置（スティムレーター）から送り出される、微弱な1mAから最大5mA程度の直流電流を流して、頭皮から頭蓋内へ通電します。直下の大脳皮質の神経活動が変化し、これを治療に応用します。陽極（**図1c**）で刺激すると電極直下の神経活動が興奮します。反対に陰極（**図1b**）で刺激すると電極直下の神経活動は抑制されます。

効果は1時間～1時間半程度、継続します。皮膚の切開といった手術は必要ありません。治

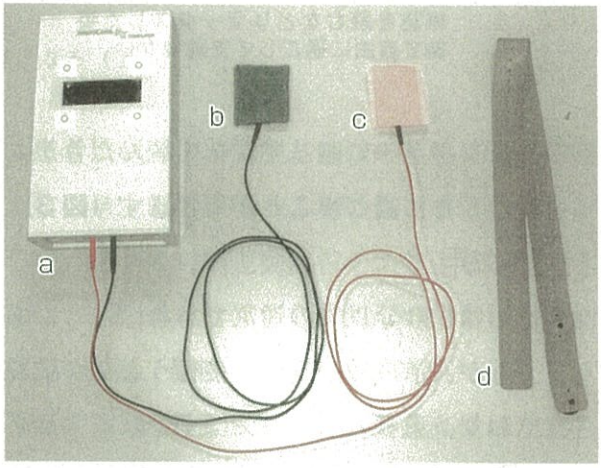

図1 ■ 経頭蓋直流電気刺激法の治療システム一式

a：刺激装置（スティムレーター）、b：陰性電極（5×7cm）、c：陽性電極（5×7cm）、d：電極固定用ゴムバンド。

図2 ■ 刺激の実際

a：右側陽極直下で神経活動の刺激。左側陰極直下では抑制が誘導される。この貼り方では左側からの半球間抑制が解除できる。
b：右側の賦活のみを目的とする場合は刺激部位に陽極を、基準電極（陰極）を反対側前頭部に置く。
c：右側の抑制のみを目的とする場合は刺激部位に陰極を、基準電極（陽極）を反対側前頭部に置く。

図3 ■ 治療中の様子

治療時間は 20 ～ 30 分。治療中は雑誌を読むなどリラックスした姿勢で自由に過ごして支障はない。

療中は、ソファーに座って雑誌を読んだりテレビを見たりして過ごすことができます（**図 3**）。

3. 副作用

副作用は、30 分以内の通電であればとくにありませんが、治療は医師が直接行うことが推奨されており、患者の安全性には十分配慮する必要があります。通電時のぴりぴり感や軽度の頭痛、皮膚の発赤などの報告もありますが、いずれも重篤なものではないようです。

4. 経頭蓋直流電気刺激法の将来性

経頭蓋直流電気刺激法は、現在、保険診療として認可されていません。病院の倫理審査委員会に申請し審議され、許可を得てから行う必要があります。現時点ではあくまで研究用ですが、日本を含めて世界中で臨床研究が活発に行われています。近い将来、脳神経外科におけるさまざまな病気に対する標準治療の一つとなる有効な方法です。

◆対象疾患・病態

1. 対象疾患と作用のメカニズム

対象となる脳の疾患には、脳腫瘍、脳卒中、高次脳機能障害、耳鳴、慢性疼痛およびうつ病などがあります。脳腫瘍や脳卒中の患者で片麻痺をきたしている場合には、病変部位を陽極刺激（神経活動を促進させる）し、健側に陰性刺激（神経活動を抑制する）を行います。脳内に病変があると健側脳が病変側の脳を抑制して、ますます手足が動かなくなる「半球間抑制」という現象が引き起こされることがあります。これに対して病変側を陽極で、健側を陰極で刺激するのは理にかなっています。半球間抑制を解除し、さらに病変部位の活動を促進できるからです。陽極刺激だけあるいは陰極刺激だけでよい場合は、もう一方の電極（基準電極）は反対側前頭部（額）に貼ります。

2. 経頭蓋直流電気刺激法の応用

高次脳機能障害では、2 つ 3 つ以上の仕事を並行して行えなくなります。たとえば主婦の場合、煮込み物をしながら、炒め物をつくり、玄関で郵便の受け取りをするなど、普段行っていることができなくなるわけですから、日常生活や仕事で支障をきたします。このような症状に対しては、左側前頭葉の外側部位を陽極刺激すると効果があります。

難治性の耳鳴に対しては、中枢性つまり側頭葉にある聴覚中枢の過活動が原因とする説があり、ここを陰極で刺激して神経活動を抑制することで治療に応用します。脳の帯状回（前頭葉

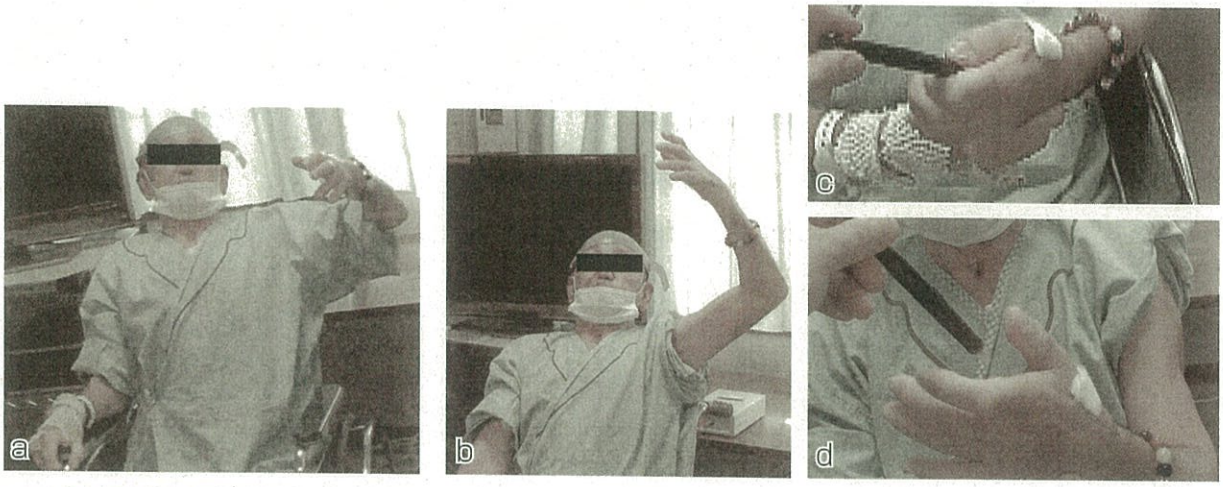

図4 ■ 治療前後の様子

a：治療前、b：治療後の左上肢挙上。
刺激後にはボールペンをつかみ（c）、離すことが可能となる（d）。

の内側部分）で痛みが増幅されて症状を出す慢性疼痛と、薬物が効きにくい難治性うつ病では、中心溝周囲（一次運動野 M1 および一次感覚野 S1 を含む領域）を刺激すると、症状の安定が得られます。この部位を刺激すると多幸感を誘導する内因性（脳が自分でつくる）の麻薬が産生され、症状改善につながるようです。

このようにさまざまな病気に対して経頭蓋直流電気刺激法が応用されていますが、今後さらに症例を増やして、より有効性の高い刺激法の確立や、治療による背景の神経回路網の変化の詳細を明らかにする必要があります。

◆経頭蓋直流電気刺激法を使ったニューロリハビリの実際

ここでは、運動麻痺の改善を目的に、一次運動野へ通電した脳腫瘍患者に対する治療の実際を示します（**図4**）。

患者は脳深部・大脳基底核の腫瘍によって左上肢の挙上制限があり、胸の高さまでしか上がらず、左手の巧緻運動障害があり、物を手で握ることができませんでした。この患者は病変側 M1 に陽極、健側 M1 に陰極を置いて通電しました。1回の経頭蓋直流電気刺激直後にただちに改善が認められています。左上肢は頭部より高く挙上できるようになりました。また治療前にはボールペンをつかめませんでしたが、治療後はボールペンをつかんで離すこともできるようになりました。

機能的な磁気共鳴画像で検査すると、手が動かなかった治療前には一次運動野に血流の上昇はありませんが、通電後には左右の運動野と中心部の補足運動野にも血流の上昇を認めています。経頭蓋直流電気刺激によって、脳の機能的な活性が誘導された証拠です。何回か治療を繰り返すことで可塑性が高まり、症状の改善に結びつきます。

Cerebellum (2016) 15:645–662
DOI 10.1007/s12311-015-0726-0

ORIGINAL PAPER

Cerebellar Contribution to Pattern Separation of Human Hippocampal Memory Circuits

Ayano Shiroma[1] · Masahiko Nishimura[1] · Hideki Nagamine[1] · Tomohisa Miyagi[1] · Yohei Hokama[1] · Takashi Watanabe[1] · Sadayuki Murayama[2] · Masato Tsutsui[3] · Daisuke Tominaga[4] · Shogo Ishiuchi[1]

Published online: 6 October 2015

Abstract The cerebellum is a crucial structure for cognitive function as well as motor control. Benign brain tumors such as schwannomas, meningiomas, and epidermoids tend to occur in the cerebellopontine angle cisterns and may cause compression of the posterior lateral cerebellum near the superior posterior fissure, where the eloquent area for cognitive function was recently identified. The present study examined cognitive impairment in patients with benign cerebellar tumors before and after surgical intervention in order to clarify the functional implications of this region in humans. Patients with cerebellar tumors showed deficits in psychomotor speed and working memory compared with healthy controls. Moreover, these impairments were more pronounced in patients with right cerebellar tumors. Functional magnetic resonance imaging during performance of a lure task also demonstrated that cerebellar tumors affected pattern separation or the ability to distinguish similar experiences of episodic memory or events with discrete, non-overlapping representations, which is one of the important cognitive functions related to the hippocampus. The present findings indicate that compression of the human posterior lateral cerebellum affects hippocampal memory function.

Keywords Posterior lateral cerebellum · Cognitive function · Brain tumor · Memory · Hippocampus · fMRI

Introduction

Recent research has shown that the cerebellum plays an important role in cognitive and emotional functions as well as motor control [1–4]. Studies using functional magnetic resonance imaging (fMRI) have shown that the actual use of a tool (e.g., scissors) primarily activates the anterior cerebellum, whereas imaginary use of a tool activates the lateral posterior lobe of the cerebellum [5]. Skilled use of the tool after learning activates a specific area near the superior posterior fissure, indicating that the posterior cerebellum is essential for information processing, space representation, and some procedural memory [6, 7] and is dependent upon the sequential relationship between discrete elements, just as in the serial reaction task. However, the acquisition of other skills does not require the learning of sequences like prism adaptation, which can be acquired during short-term motor learning. Human studies have identified the important contribution of the cerebellum to intrinsic functional connectivities [8, 9] and higher cognitive functions, especially to episodic memory, working memory, and procedural memory [10–13]. Nonetheless, the relationship between the cerebellum and hippocampal circuits in memory systems has not been fully evaluated.

Benign cerebellar tumors are isolated focal lesions that are frequently localized in the cerebellopontine angle or around

Ayano Shiroma, Masahiko Nishimura and Shogo Ishiuchi contributed equally to this work.

✉ Shogo Ishiuchi
ishogo@med.u-ryukyu.ac.jp

[1] Department of Neurosurgery, Graduate School of Medicine, University of the Ryukyus, 207 Uehara, Nishihara-machi, Nakagami-gun, Okinawa 903-0215, Japan

[2] Department of Radiology, Graduate School of Medicine, University of the Ryukyus, 207 Uehara, Nishihara-machi, Nakagami-gun, Okinawa 903-0215, Japan

[3] Department of Pharmacology, Graduate School of Medicine, University of the Ryukyus, 207 Uehara, Nishihara-machi, Nakagami-gun, Okinawa 903-0215, Japan

[4] Okinawa Study Center, The Open University of Japan, 1Senbru, Nishihara, Okinawa 903-0219, Japan

the superior posterior fissure and do not invade or destroy neural networks, unlike gliomas or vascular strokes. These tumors are essentially regional, thereby allowing a more discrete estimation of the functionality of a specific region through examination of whether the function lost before operation recovers after surgical treatment. However, although preservation of VIIth and VIIIth cranial nerve function is prioritized during neurosurgical treatment, the cognitive function of these patients has not been evaluated. We therefore analyzed the cognitive impairment of patients before and after surgical intervention in order to evaluate the functional involvement of the posterior lateral cerebellum near the superior posterior fissure. We found that patients with right cerebellar tumors exhibited disturbances in psychomotor speed as examined by the digit symbol test (DST) and working memory as examined by the digit span test (DS) when compared with healthy controls. Nonetheless, the classical neuropsychological domain does not really have a distinct functional anatomy.

In the current study, we analyzed the distinct human cerebellar contribution to memory systems under whole brain network organization using the method of Global Brain Connectivity (GBC). Several past studies have indicated that cognition involves large-scale human brain systems with multiple interacting regions. We therefore tried to identify a prominent feature of this hub of human cognition using lure task-related and resting-state functional MRI (rs-fMRI) data. We focused on the pattern separation ability that discriminates between similar experiences of episodic memory, a crucial component of the hippocampal memory circuit, and used functional MRI (fMRI) to investigate subjects performing an established lure task [14]. Interestingly, patients with cerebellar tumors selectively showed a decreased ability for pattern separation in the lure task. We first identified nine regions related to pattern separation ability by imposing stringency criteria based on an activation map of lure task fMRI findings from normal volunteers. Blood oxygen level-dependent (BOLD) signals, which are one of the indices of hemodynamic responses to neural activity, were correlated to correct response rates in the lure task associated with the activity of the following four distinct regions: right and left cerebellar hemisphere (lobule VI/Crus I), left anterior mid-cingulate cortex (aMMC), and right hippocampal dentate gyrus (DG). We then tested whether these regions showed high GBC in the rest of the brain using rs-fMRI data. We found that GBC correlated to a correct response rate in the lure task was limited to three of these regions, excluding the left cerebellar lobule VI/Crus I. Finally, we ascertained that this correlation was altered in patients with right and left cerebellar tumors as compared with normal healthy volunteers. We therefore hypothesized that the cerebellar contribution to pattern separation ability is dependent upon integration of the right cerebellar hemisphere (lobule VI/Crus I) associated with the left aMMC and right hippocampal DG. The pattern changes in the functional connectivity of patients with cerebellar tumors may indicate an important contribution of the human cerebellum to higher cognitive functions associated with hippocampal memory systems.

Materials and Methods

Subjects

Neuropsychological assessments were carried out on 28 patients with benign cerebellar tumors (mean age 50.9± 12.1 years; 11 males, 17 females), 17 with right cerebellar lesions (mean age 49.4±13.6 years; 8 schwannomas, 8 meningiomas, and 1 epidermoid) and 11 with left cerebellar lesions (mean age 53.5±8.3 years; 6 schwannomas, 2 meningiomas, 2 epidermoid, and 1 lipoma) (Table 1), as well as on a control group consisting of 23 healthy controls matched for age, sex, and years of education (mean age 53.4±14.1, range 21–72 years; 9 males, 14 females). Regarding clinical histories, one patient (R19) had previously undergone gamma knife radiosurgery, and two patients (L10 and L17) had recurrent tumors. Patients were excluded for the following reasons: age under 20 or over 78 years; lesions involving non-cerebellar cortical or subcortical regions; history of alcohol or drug abuse; or pre-existing psychiatric disease. Neurological examinations of gait, kinetic function-arm, kinetic function-leg, speech, and eye movements were conducted based on the Brief Ataxia Rating Scale [15]. All patients showed normal performance except for two cases (R2 and R7) who walked almost naturally, but were unable to walk with their feet in the tandem position. The locations of the cerebellar tumors are shown in Fig. 1 and Table 2. Notably, the tumor compressed the posterior lateral cerebellum in all patients, especially lobule VI and Crus I (Fig. 1 and Table 2). Lesion size was measured in milliliters on preoperative MRI, according to the formula; $a \times b \times c/2$, where a and b indicate the longest crossed dimension of the horizontal plane, and c indicates the greatest length of the tumor in the coronal plane.

Informed Consent and Approval

All patients and control subjects provided written informed consent for this investigation. The study was approved by the ethical committee of the University of the Ryukyus.

Experimental Design

In the preoperative stage, 28 patients with cerebellar lesions underwent neuropsychological assessments and 19 patients participated in the fMRI examination. The fMRI study was conducted once before surgical treatment. In the postoperative stage, 12 patients with right cerebellar tumors (mean age 45.0 ±11.5 years, range 21–64 years; 3 males, 9 females)

Table 1 Summary of 28 patients examined by neuropsychological assessment

Patient number	Sex/age/handedness	Diagnosis	Lesion side	Size of lesion (mL)	Follow-up assessment	fMRI study (preop)
R1	F/38/right	Meningioma	Right	3.41		
R2	M/21/right	Schwannoma	Right	50.56	+	
R6	M/61/right	Schwannoma	Right	0.27	+	
R7	F/42/right	Schwannoma	Right	18.31	+	+
R10	F/51/right	Meningioma	Right	6.55	+	+
R11	M/64/right	Epidermoid	Right	2.66	+	+
R12	F/34/right	Meningioma	Right	3.46	+	+
R13	F/52/right	Meningioma	Right	5.85	+	
R14	M/63/right	Schwannoma	Right	7.95		+
R15	M/76/right	Schwannoma	Right	5.79		
R16	F/50/right	Meningioma	Right	5.79	+	+
R17	M/49/right	Schwannoma	Right	3.68	+	+
R18	F/40/right	Schwannoma	Right	11.7	+	+
R19	M/60/right	Schwannoma	Right	5.22		+
R20	F/40/right	Meningioma	Right	0.42	+	+
R21	F/36/right	Meningioma	Right	7.71	+	+
R22	F/63/right	Meningioma	Right	13.51		+
L2	M/49/right	Meningioma	Left	3.82		
L4	F/48/right	Schwannoma	Left	27.34		+
L9	F/55/right	Schwannoma	Left	3.18		
L10	F/47/right	Schwannoma	Left	4.69		+
L11	F/69/right	Meningioma	Left	5.68		+
L12	F/59/right	Epidermoid	Left	3.97		
L13	M/53/right	Lipoma	Left	0.79		+
L14	M/38/left	Schwannoma	Left	25.94		
L15	F/62/right	Schwannoma	Left	0.25		+
L16	M/55/right	Epidermoid	Left	13.55		+
L17	F/38/right	Schwannoma	Left	16.89		+

"+" indicates participation in the follow-up assessment or fMRI study

M male, *F* female

underwent follow-up neuropsychological assessments in order to examine whether surgical intervention had an effect on functional recovery. Detailed individual profiles are shown in Table 1.

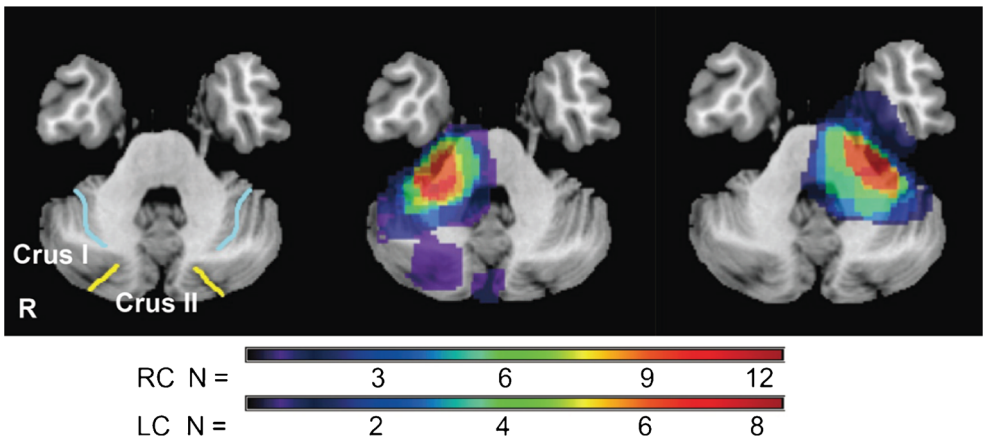

Fig. 1 Tumor topography of right (*middle image*, $n=17$) and left cerebellar tumors (*right image*, $n=11$). *Light blue line* indicates the superior posterior fissure; *yellow line* indicates the horizontal fissure in the left image

Table 2 Lesion characteristics in patients with cerebellar tumors

	Hemisphere											
Case code	I	II	III	IV	V	VI	Crus I	Crus II	VII B	VIII	IX	X
Right side												
R1							×	×				
R2			×	×	×	×	×	×	×	×	×	×
R6												×
R7			×	×	×	×	×	×		×	×	×
R10						×	×	×	×	×		
R11				×	×	×	×	×	×	×		
R12						×	×	×	×	×		×
R13							×	×	×	×		
R14			×	×	×	×				×	×	×
R15				×	×	×						×
R16			×	×	×	×	×	×	×	×		×
R17			×	×	×	×				×		×
R18						×	×			×	×	×
R19				×	×	×	×	×	×	×	×	×
R20						×	×		×			
R21				×	×	×	×	×	×			×
R22			×	×	×	×	×		×	×		×
Left side												
L2			×	×	×	×						×
L4			×	×	×	×	×	×	×	×	×	×
L9						×				×		×
L10				×	×	×	×		×	×		×
L11				×	×	×	×	×	×	×		×
L12				×	×	×	×	×	×	×		×
L13												×
L14			×	×	×	×	×	×	×	×		×
L15												×
L16			×	×	×	×						×
L17			×	×	×	×						×

"×" denotes the existence of a tumor at preoperative stage. "×" indicates the residue at postoperative stage

Neuropsychological Assessment

The battery consisted of the following tests: (I) mini-mental state examination (MMSE) [16] and modified MMSE (3MS) [17] for global cognitive screening, (II) Trail Making Test (TMT) [18] and Stroop test (ST) [18] for executive function, (III) Wechsler Adult Intelligence Scale-Revised (WAIS-R) digit span subtest (DS) [19] for working memory, (IV) WAIS-R DST [19] for psychomotor speed, (V) partial WAIS-R block design subtest (fifth and ninth items) [19] and the cube-copying test for visuospatial ability. For quantitative assessment of constructional ability in the cube-copying test, the points of connection and plane-orientation errors were evaluated. A point of connection was defined as a point at which three lines met to form a vertex, hence subjects could score up to eight points, since eight points of connection are present in a cube. Each plane with two pairs of parallel lines was evaluated in terms of the number of lines and the extent to which they were parallel. No plane-error points were scored if the cube was copied accurately [20]. We selected brief neuropsychological tests that could be performed within 1 h in order to reduce the burden on patients in the preoperative or postoperative therapeutic stage. As for the duration of patients' follow-up, we carried out of the assessment within 6 months after resection of the tumor. Patient R2 with a huge schwannoma showed transient neurological symptoms related

to the IVth nerve. The double vision by such nerve injury influenced cognitive performance, so we followed up the patient until recovery of its symptom.

Event-Related fMRI Study

Subjects

Twelve patients with right cerebellar tumors (mean age 46.9± 13.3 years, range 17–66 years; 3 males, 9 females), 7 patients with left cerebellar tumors (mean age 53.3±10.1 years, range 38–69 years; 2 males, 5 females), and 30 normal healthy volunteers (mean age 24.0±5.2 years, range 22–35 years; 21 males, 9 females) were enrolled in this study (Table 1). The normal healthy volunteers that participated in the fMRI study were different from those included in the neuropsychological analysis. Standard values in each generation of the correct response rate in fMRI behavioral task were not established. Therefore, to estimate a normal value of the correct response rate, we recruited healthy young subject. None of these patients had any signs or history of neurological or psychological diseases. This study was approved by the ethical committee of the University of the Ryukyus with written informed consent obtained from all participants. Subjects were all right-handed according to the Edinburgh Handedness Laterality Index, with a median score of 100 (range 80–100).

Experimental Paradigm

The fMRI behavioral paradigm used was a rapid event-related fMRI design [14, 21, 22] based on an explicit three-alternative forced choice task including novel (new), repeated (same), and lure (similar) stimuli consisting of color photographs of common objects. A fully randomized functional run consisted of 108 total trials, 16 lure sets, 16 repeat sets, and 44 unrelated novel items (foils) (Fig. 2). Forty-four foil trials, 16 trials first presented from repeat sets, and 16 trials first presented from lure sets were presented as the new stimuli. The same stimuli were 16 trials, which are second presented from repeat sets. The lure stimuli were 16 trials which are second presented from similar sets. Each stimulus was presented for 2,500 ms with a 0–1,000 ms interstimulus interval to prevent adaptive stimulus responses. The number of trials separating similar and identical pairs was randomly varied from 10 to 40 trials. Several photographs were displayed to participants on a goggles display during the session. If the photograph was first presented in the session, participants were required to press the *red* button indicating a new object. If the photograph had been displayed before in the session, examinees were instructed to press the *blue* button indicating a repeated object. Finally, if they thought that the photograph was similar to, but not the same as previous stimuli, they were required to press the *green* button, indicating a similar but not identical object. Responses and reaction times were recorded in a button box (Current Designs, Inc., Philadelphia, Pennsylvania). Visual stimuli were presented to the subjects using 800×600 resolution magnet-compatible goggles under computer control (Resonance Technologies, Inc., Salem, Massachusetts) using Presentation® software (Neurobehavioral Systems, Inc., Austin, Texas).

MRI Data Acquisitions

Anatomical and functional images were obtained using a 3-T MRI scanner (Discovery MR750; GE Medical System, Waukesha, Wisconsin, USA) with a 32-channel head coil and high-order manual shimming to the temporal lobes. The array spatial sensitivity encoding technique (a parallel imaging technique) was used to acquire imaging data by reducing geometric distortion for echo planar imaging (EPI). The anatomical three-dimensional (3D) spoiled gradient recalled echo (SPGR) sequence was obtained with a high-resolution 1-mm slice thickness (matrix size 256×256, field of view 256×256 mm, repetition time 6.9 ms, echo time 3 ms, flip angle 15°). T2*-weighted EPI sequence was used to measure BOLD contrast (repetition time 1,500 ms, echo time 25 ms, flip angle 70°, matrix size 128×128, field of view 192×192, in-plane resolution 1.5×1.5 mm^2, 23 slices, 3-mm thickness, 0-mm space). A total of 303 volumes were collected over one session during the experiment in a sequential ascending order. A high-resolution T2 fast spin echo (T2 FSE) sequence (repetition time 4,300 ms, echo time 92 ms, matrix size 512×512, field of view 192×192, in-plane resolution 0.375×0.375 mm^2, 23 slices, 3-mm thickness, 0-mm space) was obtained for the co-registration of 3D SPGR and EPI functional images. EPI functional images and T2 FSE structural images were acquired in an oblique coronal plane perpendicular to the long axis of the hippocampus. Almost the entire hippocampus (head, body, and tail) was included in the 23 slices. Functional images were localized in the sagittal plane of the SPGR image to identify the long axis of the hippocampus. Oblique coronal slices were fitted to the principal longitudinal axis of the hippocampus covering the entire bilateral medial temporal lobes. Firstly, distortions of fMRI signals were corrected by array spatial sensitivity encoding techniques, which were used to improve temporal and spatial resolution and reduce artifacts. Secondly, higher order shims were employed to directly compensate for local field distortions. These methods guaranteed homogeneity of the magnetic field.

Preprocessing and Estimations

Functional and structural MR images of the brain were preprocessed using the methods of realignment, temporal correlation, spatial normalization, and spatial smoothing. The data were analyzed using SPM8 software (Wellcome Trust

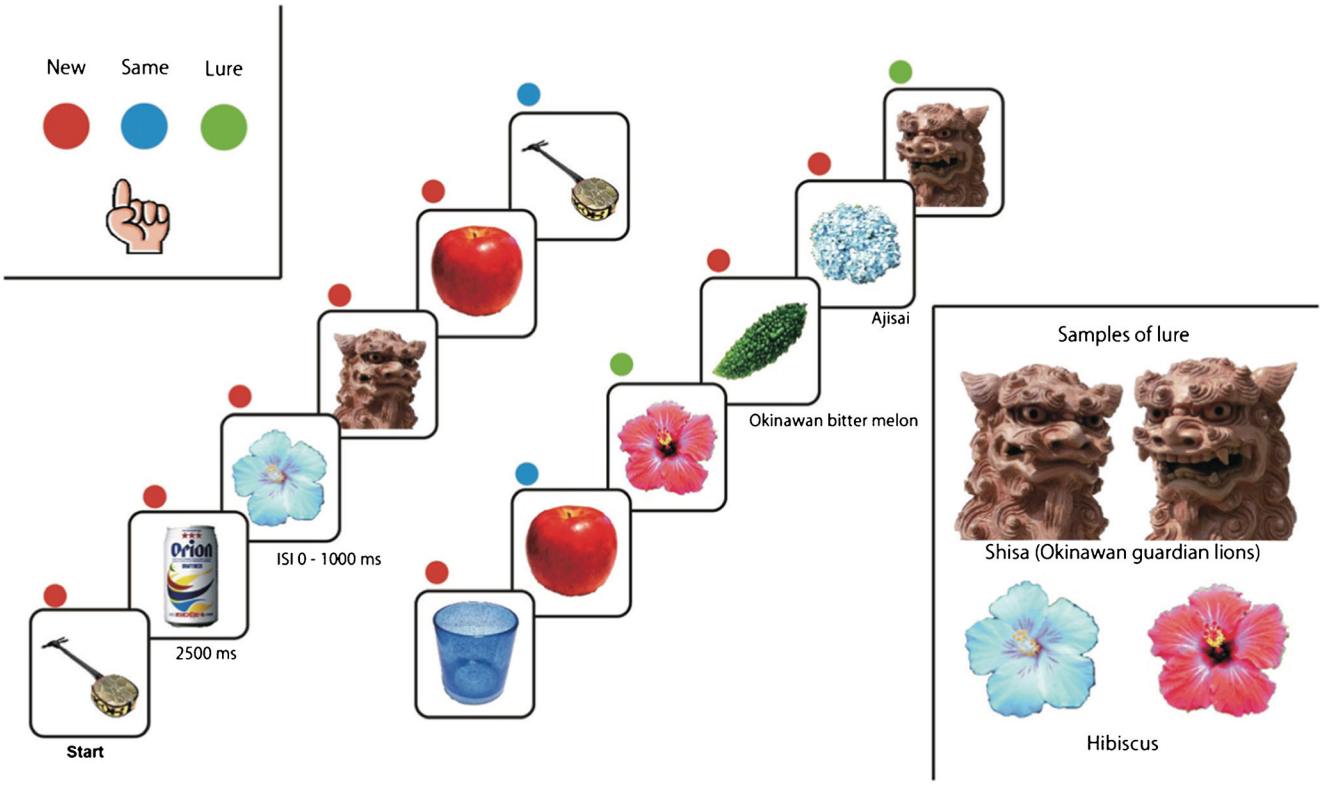

Fig. 2 fMRI behavioral task. Images of single items were presented for 2,500 ms followed by a 0–1,000 ms interstimulus interval. Novel, repeated, and similar lure items were randomly shuffled in the task. *Upper left insets* show three task buttons for new (*red*), lure (*green*), and repeated (*blue*) stimuli. *Lower right insets* show examples of lure pairs; Okinawa guardian lions and hibiscuses

Centre for Neuroimaging, University College London, London, UK). The first five volumes in each data set were removed to ensure that the signal reached a steady state. EPI functional images were corrected to account for the differences in slice acquisition times by interpolating the voxel time series using sinc interpolation and resampling the time series using the center slice as the reference point. The EPI functional images were then corrected for motion artifacts by realignment to the first volume. A mean EPI functional image was constructed during realignment. Co-registration was performed through two processes. Both the mean EPI functional image and the motion-corrected EPI functional images were co-registered to the T2 FSE structural image. The co-registered T2 FSE structural image was then co-registered to the structural SPGR image. Next, the registration points of the anterior and posterior horns of the lateral ventricle, top surface of the paracentral lobule, and bottom surface of the inferior temporal gyrus were checked in the T2 FSE structural, structural SPGR, and EPI functional images. Before spatial normalization, a parameter was produced by the segmentation process from the structural SPGR image. The structural SPGR image and EPI functional images were spatially normalized ($1 \times 1 \times 1$ mm) using the Montreal Neurological Institute space. Finally, the images were spatially smoothed using a Gaussian kernel with a full width at a half maximum of 3 mm. To detect the brain activation associated with a specific task while simultaneously reducing noise, the size of the smoothing kernel was kept at a recommended 2 to 3 times the voxel size [23]. A high-pass filter regressor (200 s) was included in the design matrix to exclude low-frequency noise and artifacts. To identify the correct activation spots of the brain, movement effects were discounted in a number of rows (298) and columns (3 translations and 3 rotations). For each subject, the three (new, lure, and repeated) regressors were estimated by a general linear model calculated by applying a canonical hemodynamic response function combined with time and dispersion derivatives. To assess the main effect of the lure images, as characterized by both the hemodynamic response function and these derivatives, an F-contrast obtained by the F test was required. Intra-individual activation maps were calculated by F tests. We calculated second-level group contrasts using a one-sample t test for each regressor (new, lure, and same) from the response of the canonical hemodynamic function. Differences in the intensities of the activation between task conditions were confirmed by a voxel-level threshold of $p<0.001$ uncorrected, and a cluster-level threshold of FWE (family-wise error)-corrected $p<0.05$. We extracted the average percent signal change values of the regions of interest (ROIs) from the anatomically defined AAL ROI atlas [24] and established 3D MRI atlases [25–27] for each subject and type of task stimuli using the MarsBar toolbox [28].

Global Brain Connectivity Analysis

Subjects

Twelve patients with right cerebellar tumors (mean age 46.9± 13.3 years, range 17–66 years; 3 males, 9 females), 7 patients with left cerebellar tumors (mean age 53.3±10.1 years, range 38–69 years; 2 males, 5 females), and 15 right-handed healthy volunteers (mean age 27.6±6.5 years, range 20–44 years; 5 males, 10 females) were enrolled in this study. The normal healthy volunteers participating in the resting-state fMRI study were different from those included in the neuropsychological analysis and the event-related fMRI experiment. No participants had any signs or history of neurological or psychological diseases. This research was approved by the ethical committee of the University of the Ryukyus, and written informed consent was obtained from all participants.

Acquisition of Resting-State fMRI Data

Functional and anatomical images were obtained using a GE Discovery MR750 3.0 Tesla MRI scanner (GE Medical System) with a 32-channel head coil. In order to minimize head movement, the heads of each of the participants were fixed using foam pads. In order to reduce geometric distortion in EPI, a parallel imaging technique known as the array spatial sensitivity encoding technique was used during imaging data acquisition. T2*-weighted EPI images were used to measure BOLD contrast (repetition time 2,000 ms, echo time 30 ms, flip angle 70°, matrix size 64×64, field of view 256×256, in-plane resolution 4× 4 mm, 42 slices, 4-mm thickness, 0-mm space). During EPI image scanning, participants were instructed to remain motionless, remain awake, relax with their eyes closed, and to try not to think about anything in particular. A total of 150 volumes were collected over one session in a sequential ascending manner (plus 5 initial discarded volumes). An anatomical three-dimensional spoiled gradient recalled echo (3D SPGR) sequence was obtained with high-resolution 1-mm slice thickness (matrix size 256× 256, field of view 256×256 mm, repetition time 6.9 ms, echo time 3 ms, flip angle 15°). A high-resolution T2 fast spin echo (T2 FSE) sequence (repetition time 4,300 ms, echo time 92 ms, matrix size 256×256, field of view 192×192, in-plane resolution 1.33×1.33 mm, 42 slices, 4-mm thickness, 0-mm space) was obtained for the co-registration of 3D SPGR images and EPI functional images. EPI functional and T2 FSE structural images were acquired in an oblique axial transverse plane (tilted 30° anterior relative to the intercommissural plane).

Preprocessing and Analysis of Resting-State fMRI Data

Following this step, fMRI preprocessing, analysis, and visualization methods were conducted as implemented in SPM (8 package, http://www.fil.ion.ucl.ac.uk/spm8/) and the "conn" toolbox (www.nitrc.org/projects/conn). Images were corrected for slice acquisition time within each volume, motion corrected with realignment to the first volume, spatially normalized to the standard MNI EPI template, and spatially smoothed using a Gaussian kernel with a full width at half maximum of 8 mm. 3D SPGR images were co-registered with each mean EPI and T2 FSE image, and averaged together to permit anatomical localization of the functional connectivity at the group level. The transformed structural images were segmented into gray matter (GM), white matter (WM), and cerebrospinal fluid (CSF) using a unified segmentation algorithm.

In addition to removing noise correlations present in WM and CSF, the addition of six motion regressors (six realignment parameters and first derivatives) controlled for correlations due to movement. Data were filtered between 0.009 and 0.08 Hz.

Correlation Analysis with Global Brain Connectivity and the Lure Task

A map of GBC was computed from resting-state fMRI data using the "conn" toolbox (www.nitrc.org/projects/conn) [29, 30]. In the "conn" toolbox, correlation maps were calculated on the basis of seed-based correlation analysis using the AAL ROI atlas [24]. When the population correlation coefficient is zero, the distribution of correlation coefficient is consistent with the normal distribution. However, normal distribution of the correlation coefficient is lost when the correlation coefficient approximates to 1 [31]. Each ROI's correlation coefficient map was transformed by Fisher's Z transformation to Z value maps in order to normalize the correlation coefficient.

These Z value maps were averaged together across each subject in order to calculate GBC values. For correlation analysis of the GBC and score of the lure task, GBC values were extracted from the ROIs that were activated by the lure stimulus in the event-related fMRI experiment. The Pearson product–moment correlation coefficient was used to calculate correlations between GBC values and the correct response rates in the lure task. When the correlation coefficient was close to +1, the r value indicated a proportional connection between GBC values and the scores in the lure task (positive correlation). Conversely, when the correlation coefficient was close to −1, the r value showed an inverse proportion (negative correlation). We estimated the strength of the correlation in five categories: negligible correlation (0.00 to 0.30 or 0.00 to −0.30), low correlation (0.30 to 0.50 or −0.30 to −0.50), moderate correlation (0.50 to 0.70 or −0.50 to −0.70), high correlation (0.70 to 0.90 or −0.70 to −0.90), and very high correlation (0.90 to 1.00 or −0.90 to −1.00) [32].

Statistical Analysis

The Kruskal-Wallis test for three independent samples or the Mann–Whitney U test for two independent samples was used

to evaluate statistical significance in the neuropsychological assessments and fMRI behavioral tasks, since a normally distributed population could not be assumed. Preoperative and postoperative neuropsychological data were compared using the Wilcoxon signed rank test. Statistical significance was accepted at $p<0.05$. The chi-square test was used to evaluate the performance in the block design subtest, since only two items of the block design subtest were evaluated as pass/fail.

Results

Preoperative Neuropsychological Profile of Patients with Benign Cerebellar Tumors

The results of the neuropsychological test of DST ($p<0.05$), forward span of DS ($p<0.05$), backward span of DS ($p<0.01$), and total score of DS ($p<0.05$) among patients with cerebellar tumors ($n=27$) indicated a significant impairment as compared with the control group, which was further confirmed using the Mann–Whitney U test. To examine whether the profile of the impairments depended on the side of the lesion, patients with right and left tumors were compared to the control group. Performance on neuropsychological tests including MMSE, DST, forward span of DS, backward span of DS, total score of DS, and cube-copying test significantly differed across groups. Patients with right cerebellar tumors performed significantly worse than the control group on DST ($p<0.001$), forward span of DS ($p<0.010$), backward of DS ($p<0.001$), and total score of DS ($p<0.05$), as indicated by a post hoc Mann–Whitney U test with Bonferroni correction (Table 3). In contrast, there were no significant impairments in left-sided tumors as compared to the control group (Table 3). A Mann–Whitney U test was used to confirm that patients with right-side tumors showed significantly lower scores on the MMSE when compared with patients with left-side tumors ($p<0.05$) (Table 3). No direct relationship was found between tumor size and scores on neuropsychological assessments, with the exception of the DST ($r=-0.48$, $p<0.05$). None of subjects failed the fifth item of block design test. Chi-square analysis of the performance of the ninth item on the block design subtest revealed no significant difference between patients with right or left cerebellar tumors and the control group.

Postoperative Neuropsychological Profile of Patients with Benign Cerebellar Tumors

Since most neuropsychological tests showed a significant decline in patients with right-sided tumors as compared with the control group at the preoperative stage, 12 patients with right cerebellar tumors were further tested 2 weeks to 18 months after resection of the tumor in order to investigate whether cognitive function became normalized after surgical decompression of the posterior lateral cerebellum. T1-weighted MRI confirmed that the decompressed cerebellum, especially lobule VI and Crus I had completely recovered after treatment (Table 2 and Fig. 3). Comparison of preoperative and postoperative neuropsychological tests revealed improvements in the raw scores of DST from 8.33±3.20 to 8.92±3.23, DS forward span from 6.08±1.16 to 6.25±1.60, DS backward span from 4.08±0.90 to 4.58±1.73, and DS total score from 9.92±3.06 to 10.83±4.59. However, no significant difference was found between neuropsychological assessments because of the small sample size (Table 4).

Hippocampal Function

Analysis of the reaction times for new, lure, and repeated task revealed no significant difference across groups (Fig. 4a–c). However, a significant decline was observed in the correct response rates during lure tasks in patients with right cerebellar tumors (13±18 %; $n=12$, age 53.4±13.4 years) ($P=0.0003$) compared with those of normal healthy volunteers (46.3±3.3 %; $n=30$, age 24.0±5.2 years). Furthermore, no difference was found between patients with right and left cerebellar tumors (30±18 %; $n=7$, age 53.3±10.1 years) ($P=0.25$) (Fig. 4d–f).

BOLD Responses

We confirmed the BOLD signal activity in the right DG but not left ones correlated to correct response rate of the lure task rather than error one, nor other new and similar ones in normal healthy volunteers. These results indicate a crucial contribution of right DG for the performance of pattern separation ability (Fig. 5a, b). We therefore analyzed BOLD response patterns in the right DG during lure tasks. In normal healthy volunteers, the initial dip in the BOLD response occurred at 1.7±1.3 s (mean±S.D.) in time course, followed by a fractional increase in blood flow within 3.9±4.2 s. The subsequent signal decrease was delayed by 8.3±5.1 s, and the % BOLD change from that of the resting state was −0.19±0.27, followed by a slope to a plateau or peak value for long pulses (>20 s) (Table 5 and Fig. 5c). Signal fluctuation or alteration of the BOLD pattern was found in patients with cerebellar tumors. A delayed latency of the initial positive peak (5.3±1.9 s) with a large amplitude of % BOLD change (0.190±0.060) subsequently followed by an initial dip (2.1±0.9 s) was found in patients with right cerebellar tumors (Table 5 and Fig. 5d). For patients with left cerebellar tumors, we found a rapid initial peak (3.3±1.4 s) without an initial dip, followed by a slope to a plateau value with a large S.D. value ranging from −0.18 to 0.28, indicating signal fluctuations among examinees of this group (Table 5 and Fig. 5e).

Table 3 Results of neuropsychological assessment of patients with damage to the right or left cerebellar hemispheres

Test	Cerebellar lesion		Controls, $n=23$	P
	Right, $n=17$	Left, $n=11$		
Age, years	49.41 (13.99)	52.09 (9.48)	53.39 (14.05)	n.s
Education, years	13.29 (1.90)	12.82 (2.04)	12.91 (2.39)	n.s
Cerebellar lesion size, mL	8.99 (11.66)	9.65 (9.86)	–	n.s.
3MS	96.18 (4.37)	97.59 (2.52)	97.50 (2.14)	n.s.
MMSE	28.53 (2.00) †	29.73 (0.90)	29.13 (1.26)	0.034
WAIS-R Digit symbol test #	8.65 (3.57)*	11.64 (3.38)	12.04 (2.44)	0.015
WAIS-R Digit span test				
Forward span	5.88 (1.05)*	6.45 (1.13)	6.86 (1.39)	0.025
Backward span	4.12 (0.86)*	4.64 (1.29)	5.43 (1.31)	0.006
Total score #	10.06 (2.70)*	11.55 (2.30)	12.08 (2.82)	0.048
TMT, s				
Part A	36.94 (11.94)	34.82 (11.16)	30.74 (8.59)	n.s
Part B	64.82 (22.74)	64.00 (26.20)	52.52 (19.61)	n.s
Part B-A	27.88 (13.61)	29.18 (19.41)	21.78 (14.20)	n.s
Stroop test, s				
Reading (I)	24.94 (4.70)	22.00 (4.38)	22.78 (4.19)	n.s
Naming (II)	33.24 (6.89)	30.64 (5.28)	30.35 (6.59)	n.s
Interference (III)	58.41 (22.61)	48.09 (15.27)	48.04 (13.62)	n.s.
III-II	25.18 (18.46)	17.45 (12.19)	17.70 (8.19)	n.s.
Cube-copying test				
Point of connection	7.00 (1.97)	7.45 (1.04)	8.00	0.011
Plane-drawing errors	0.41 (1.00)	0.45 (0.82)	0	n.s

Values are mean (standard deviation). # denotes scaled score (mean = 10, standard deviation = 3). *P* indicates a significant difference after Kruskal-Wallis test or Mann–Whitney *U* test; * indicates a significant decline compared to controls (post hoc Mann–Whitney *U* test with Bonferroni correction, $p<0.05$); † denotes a significant decline compared to patients with left lesions (post hoc Mann–Whitney *U* test with Bonferroni correction, $p<0.05$)

n.s. not significant, *3MS* modified mini-mental state examination, *MMSE* mini-mental state examination, *TMT* Trail Making Test

Correlation Analysis with Brain Activation and Lure Task

We began by detecting important regions for memory systems on the basis of the activation maps gathered from 30 healthy participants during the performance of a lure task involving pattern separation, which is an important human memory function of hippocampal circuits (Table 6). Next, we evaluated whether neural activity measured by local BOLD signal changes correlated to accurate response rates in the lure task across examinees, indicating a functional role of the regions instead of individual differences between examinees (Fig. 6a–i). The source ROIs were defined as the right DG, left anterior middle cingulate cortex (aMCC), and bilateral cerebellar lobule VI including Crus I, based on the correlation analysis of BOLD responses and percentage of correct responses in the lure task (Fig. 7a, c, e). Correct identification of source ROIs was confirmed by established 3D MRI atlases (Fig. 7b, d, f) [24–27]. Subdivisions of the rostral cingulate cortex, hippocampus, and cerebellum were painted on an individual structural SPGR image using FSLview in the FMRIB Software Library v5.0 (FMRIB Analysis Group, University of Oxford, Oxford, UK). The parameters of the GBC were extracted from the source ROIs above.

Correlation with GBC and Pattern Separation

For the GBC measure, we assessed standard resting-state fMRI data, and tested whether the right DG, left aMCC, and bilateral cerebellar lobule VI including Crus I had high GBC with the rest of the brain. The range of GBC values was from −2.1 to 1.9 in the normal control group, while patients with left and right cerebellar tumors showed more narrow ranges, from −0.09 to 0.07, and −0.07 to 0.11, respectively. The Pearson product–moment correlation coefficient was used to assess correlations between the GBC parameters of the four source ROIs and the percentage of correct responses in the lure task. The control subjects ($n=15$) showed moderate positive correlations with the GBC of the right cerebellar lobule VI, including Crus I ($r=0.65$, $p<0.01$), right hippocampal DG ($r=0.62$, $p<0.01$), and left aMCC ($r=0.56$, $p<0.05$) (Fig. 8a),

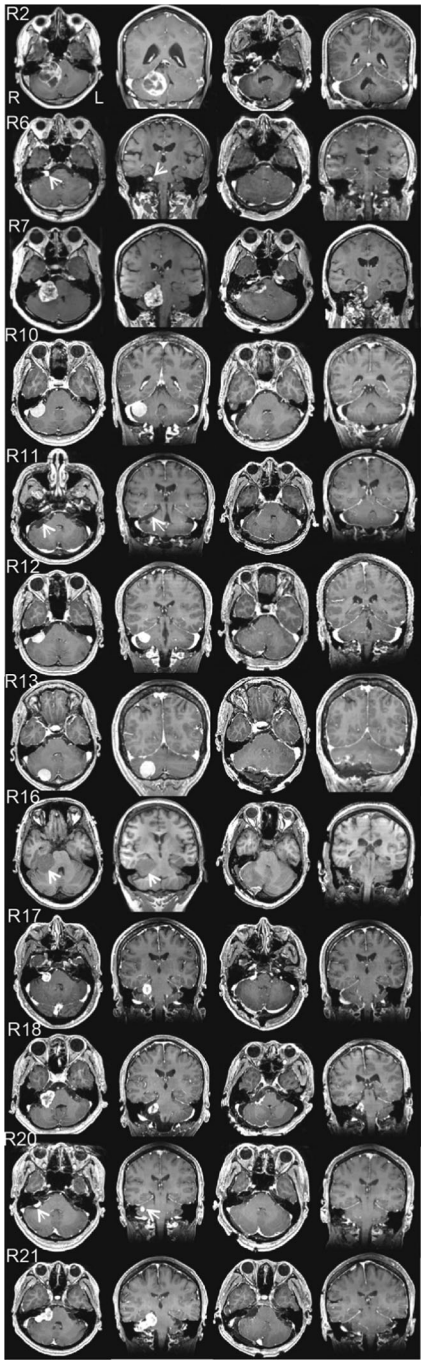

Fig. 3 Panels of pre- and postoperative gadolinium-enhanced T1-weighted MRI of cases R2, R6, R7, R10, R11, R12, R13, R16, R17, R18, R20, and R21 (from *top* to *bottom*). *Rows* show axial and coronal images before the operation, and axial and coronal images after the operation (from *left* to *right*). Since Case R16 is subject to asthma, T1-weighted MRI was performed without contrast medium

though no significant correlation was found in the left cerebellar lobule VI including Crus I (r=0.0001, p>0.05). We found that GBC connectivity correlated to correct response rates during lure tasks was limited to three regions including the right cerebellar hemisphere (lobule VI/Crus I), left aMMC, and right hippocampal DG. Herein, we raised the hypothesis that these three regions might play a crucial role in the human memory system, since rs-fMRI connectivity not only correlated to established structural connectivity, but also reflected well-known functional networks [33, 34]. Thus, GBCs in the right cerebellar hemisphere (lobule VI/Crus I), left aMMC, and right hippocampal DG were considered as the essential intrinsic connectivity of human cognition, statistically. In patients with left cerebellar tumors (n=7), high positive correlations were found in the right cerebellar lobule VI including Crus I (r=0.76, p<0.05), right DG (r=0.72, p<0.05), and left aMCC (r=0.81, p<0.01) (Fig. 8b), while the left cerebellar lobule VI including Crus I showed an extremely negative correlation (r=−0.96, p<0.001). In patients with right cerebellar tumors (n=12), significant alteration of correlations were found in the right cerebellar lobule VI including Crus I (moderate negative correlation; r=−0.64, p<0.05) and left cerebellar lobule VI including Crus I (high negative correlation; r=−0.74, p<0.01), but no correlation was found in the right DG (r=−0.04, p>0.05) or aMCC (r=−0.11, p>0.05) (Fig. 8c). These results might collectively indicate an important cerebellar contribution to pattern separation.

Discussion

We examined functional involvement of the posterior lateral cerebellum and its functional relationships with the hippocampus and the prefrontal cortex including anterior mid-cingulate cortex. Previous studies have investigated patients with cerebellar lesions such as tumors, strokes, and degenerative diseases, which frequently damage normal brain tissues. Our study evaluated patients with benign cerebellar tumors, because these lesions do not extensively destroy the surrounding normal brain tissues, so that neuropsychological assessment before and after treatment could clarify the functional involvement of the decompressed area. Human cerebellar cognitive function has been extensively studied in relation to the prefrontal cerebral cortex, but few studies have evaluated the correlation between hippocampal function and the cerebellar neocortex. Therefore, the present study also analyzed the functional activity of the posterior lateral cerebellum in relation to the hippocampus and anterior mid-cingulate cortex.

Functional Involvement of the Posterior Lateral Cerebellum

To the best of our knowledge, the present study presents the first examination of the cognitive profiles of patients with benign cerebellar tumors that compress the posterior lateral cerebellum. Neuropsychological assessments indicated that patients with right cerebellar tumors showed impairments in working memory and psychomotor speed when compared with age-matched healthy controls. Patients with right

Table 4 Neuropsychological assessment of 12 patients with right cerebellar tumors at the preoperative stage and postoperative stage

Test	Preoperative assessment	Postoperative assessment	*P*
3MS	96.28 (4.99)	97.88 (2.59)	n.s.
MMSE	29.17 (1.11)	29.25 (1.76)	n.s.
WAIS-R Digit symbol test #	8.33 (3.20)	8.92 (3.23)	n.s.
WAIS-R Digit span test			
Forward span	6.08 (1.16)	6.25 (1.60)	n.s.
Backward span	4.08 (0.90)	4.58 (1.73)	n.s.
Total score #	9.92 (3.06)	10.83 (4.59)	n.s.
TMT, s			
Part A	33.58 (10.74)	36.50 (17.20)	n.s.
Part B	59.50 (23.33)	59.92 (23.91)	n.s.
Part B-A	25.92 (13.85)	23.42 (11.75)	n.s.
Stroop test, s			
Reading (I)	24.75 (2.30)	25.17 (3.79)	n.s.
Naming (II)	32.42 (4.64)	33.83 (7.76)	n.s.
Interference (III)	52.58 (18.92)	49.25 (14.64)	n.s.
III-II	20.17 (16.08)	15.42 (9.24)	n.s.
Cube-copying test			
Point of connection	7.33 (1.79)	7.92 (0.29)	n.s.
Plane-drawing errors	0.33 (0.89)	0	n.s.

Values are mean (standard deviation). # denotes a scaled score (mean=10, standard deviation=3). n.s. denotes not significant after a Wilcoxon singed rank test

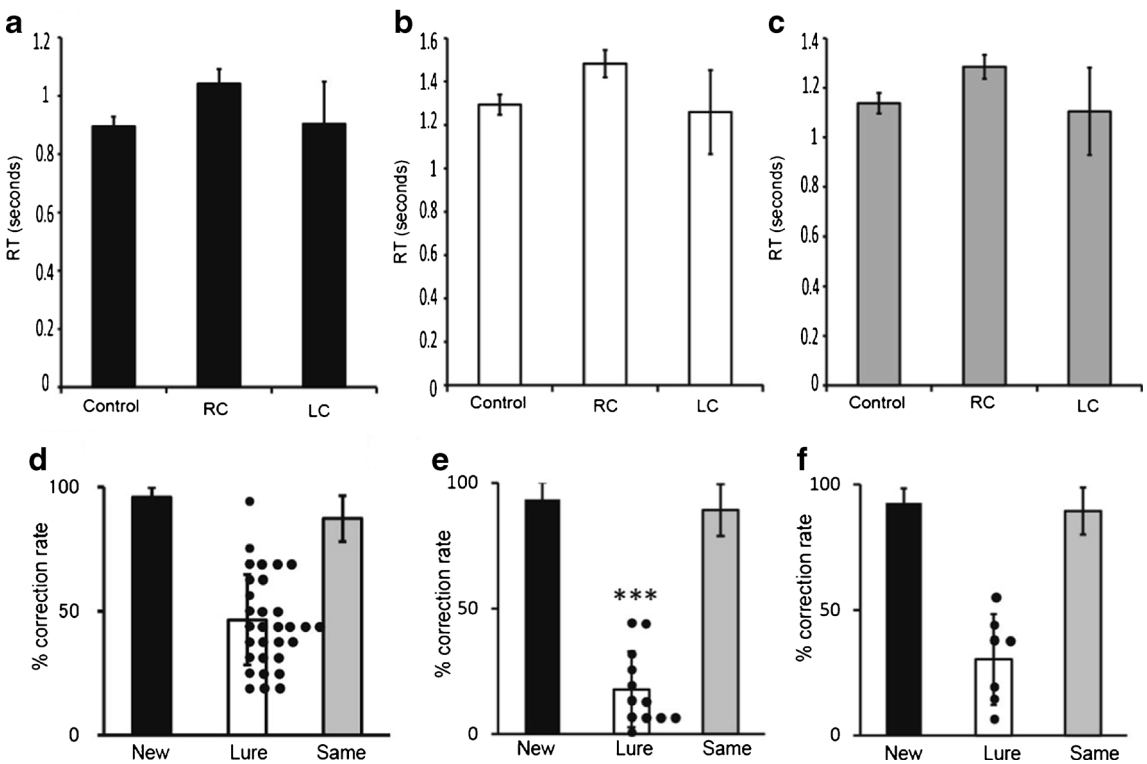

Fig. 4 Pattern separation task examined by fMRI. **a**–**c**. Reaction times (RT) for new (**a**), lure (**b**), and repeated (**c**) tasks. Control indicates normal healthy volunteers (n=30); RC, patients with right cerebellar tumors (n=12); LC, patients with left cerebellar tumors (n=7). *Bars* indicate mean; *Dots*, scores of individual cases. **d**–**f**. Percentage of correct response to new, lure, and repeated tasks in normal healthy volunteers (**d**), patients with right cerebellar tumors (**e**), and patients with left cerebellar tumors (**f**). *** in **e** indicates significant decrease compared to control (p<0.001, Mann–Whitney U test)

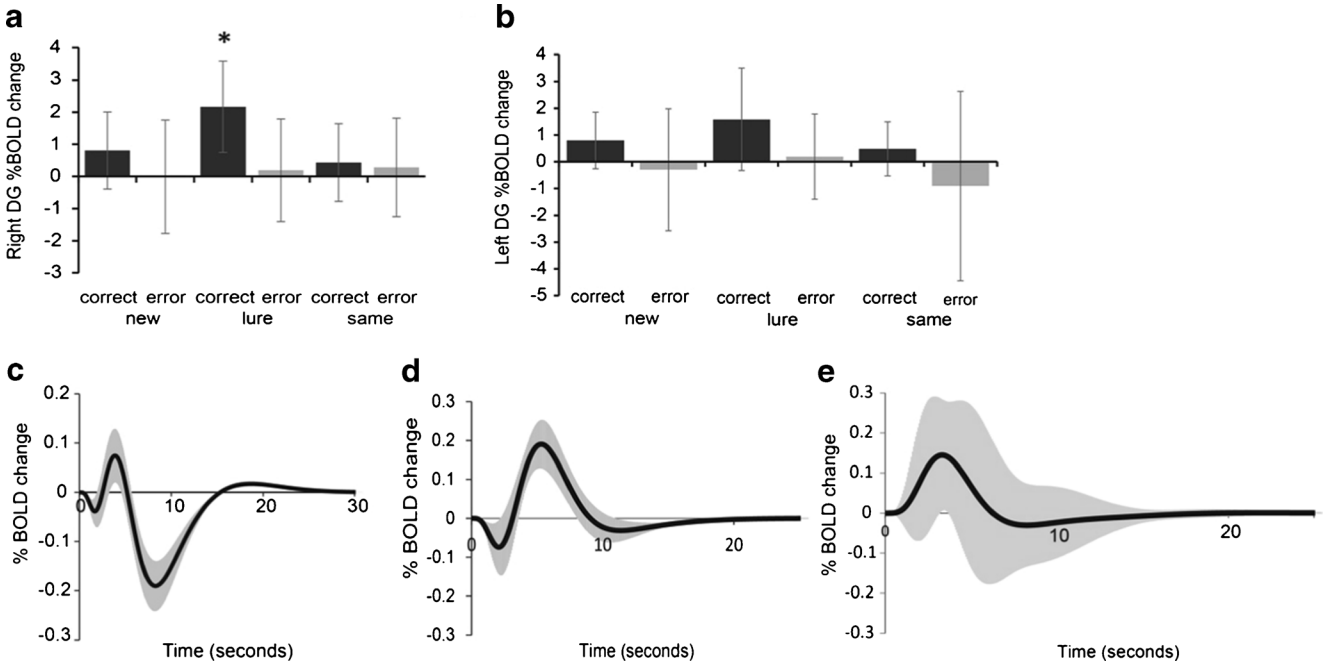

Fig. 5 BOLD response by pattern separation task. **a**–**b**. *Bar graph* showing BOLD responses in the *right* and *left* DG for correct and error responses of the new, lure, and same tasks in normal healthy volunteers. Correct responses in the lure task were increased during activation of the right DG more so than correct and error responses in other tasks (n=30) (two-way ANOVA, F=4.52, p<0.001, multiple comparisons two-sided test with Bonferroni-corrected critical p<0.05) (**a**). There was no significant difference in % BOLD change in the left DG caused by responses and/or tasks (two-way ANOVA, F=1.79, p=0.13) (**b**). *y*-axis indicates the magnitude of the % BOLD change. * denotes a significant increase compared to other conditions (p<0.05). *Graphs* showing the average BOLD curve for the lure task in normal healthy volunteers (**c**, n=30), that of patients with right cerebellar tumors (**d**, n=12), and that of patients with left cerebellar tumors (**e**, n=7). The *black line* shows the average BOLD curve and the *gray line* shows standard deviation. The *x*-axis represents time course (s) of the percentage of BOLD change. The *y*-axis represents the magnitude of % BOLD change, or the percentage BOLD signal change from the resting to stimulus condition

cerebellar tumors also showed lower scores in MMSE than patients with left-sided tumors. We tried to interpret these cognitive declines with the view that the cerebellum contributes to intrinsic functional connectivity. The laterality and disease dominancy of cerebellar tumors may therefore be important. With regard to crossed cerebello-cerebral connections, patients with right-sided cerebellar lesion showed impairments in verbal tasks, whereas patients with left-sided tumors showed deficits in spatial tasks [35, 36]. Several studies have suggested a similar laterality in cognitive symptoms [37–39], and imaging studies have elucidated cerebellar topography and lateralization effects [40, 41]. Imaging studies [40, 41] have shown that activation peaks in language tasks were lateralized to the right lobule VI and lobule VII. In contrast, spatial processing showed greater left hemisphere activation, predominantly in lobule VI [40] and lobule VII [41]. Consistent with these imaging and clinical findings, Wang et al. [42, 43] reported cerebellar symmetry in relation to cerebral intrinsic functional connectivity. They indicated a right-lateralized cerebellar network including crus I/II and a portion of lobule VI, which couples to a left-lateralized cerebral network involving the inferior frontal gyrus, superior temporal

Table 5 Latency and amplitude of BOLD in the lure task in normal healthy subjects and patients with cerebellar tumors

Peak	Mean (SD) latency (second)			Mean (SD) amplitude (% BOLD change)		
	Normal (n=30)	RC (n=12)	LC (n=7)	Normal (n=30)	RC (n=12)	LC (n=7)
N1	1.7 (1.3)	2.1 (0.9)	0.2 (1.1)	−0.039 (0.165)	−0.074 (0.070)	0.000 (0.000)
N2	8.3 (5.1)	None	None	−0.191 (0.272)	None	None
P1	3.9 (4.2)	5.3 (1.9)	3.3 (1.4)	0.074 (0.292)	0.190 (0.060)	0.140 (0.140)

RC indicates patients with right cerebellar tumors; LC, patients with left cerebellar tumors. The first negative peak is defined as N1, second negative peak as N2, and first positive peak as P1. None indicates the absence of a peak

Table 6 Significant whole-brain activations for the lure task

Region	Cluster size	Peak of *T* value	Peak coordinates		
			x	*y*	*z*
Rt. cerebellar lobule VI/Crus I	10,064	13.18	−32	−47	−33
Lt. cerebellar lobule VI/Crus I	8,572	12.96	35	−54	−22
Lt. lateral prefrontal cortex	12,393	12.25	57	10	29
Lt. caudate nucleus	4,885	11.45	13	6	11
Lt. middle cingulate gyrus	19,034	11.07	3	11	42
Rt. lateral prefrontal cortex	8,725	10.74	−49	9	25
Rt. caudate nucleus	5,150	8.73	−13	11	2
Rt. hippocampus including DG	1,859	8.51	−20	−36	−6
Rt. middle frontal gyrus	1,927	7.32	−33	2	55

Voxel-level threshold at $p<0.001$ uncorrected, corrected for multiple comparisons (family-wise error) to $p<0.05$ using a cluster threshold

Rt right, *Lt* left, *DG* dentate gyrus

gyrus, and temporal pole in the cerebral cortex. These regions include traditional language areas in the cerebral cortex, such that the cerebellar regions are commonly activated by language-related tasks. In our study, patients with right cerebellar tumors showed lower scores on the MMSE than patients with left-side tumors. Language processing is the main cognitive demand of the MMSE. Compression of the portions of the right lobule VI and Crus I connected with language areas alters the right-lateralized cerebellar network that supports language processing, which may lead to MMSE scores in patients with right cerebellar tumors. In the working memory test, lesion studies revealed that the inferior cerebellum was associated with performance on digit span test [13, 44]. There are laterality differences within the inferior lobe of cerebellum. The left inferior lobe of cerebellum is associated with the processing of aural information, whereas the right inferior lobe is involved in visual information [12]. Damage to left inferior cerebellar lobule VIII has been shown to reduce auditory digit span [44]. However, Ravizza et al. [13] revealed that performance on the auditory digit span test was unaffected by laterality of the damaged cerebellar hemisphere. Inconsistent with previous studies, the present study shows that patients with right-sided tumors exhibited impairment in the performance of the digit span test when compared with normal healthy volunteers. Chen and Desmond [11] hypothesized two cerebro-cerebellar networks for verbal working memory: the frontal/superior cerebellar network involving the right cerebellar lobule VI, Crus I, and Broca's area, which is associated with articulatory rehearsal; and the parietal/inferior cerebellar network involving the right cerebellar lobule VIIB and inferior parietal lobe, which is related to maintenance/storage of information. In the present study, impairment on working memory in patients with right-sided tumors might be related to some change in the neural bases for processing verbal working memory caused by tumor compression in the right superior and inferior cerebellum. We also found that psychomotor speed was disturbed in patients with right cerebellar tumors compared with control subjects. DST is a psychomotor performance test thought to be affected by various cognitive demands, such as motor skill, attention, and visuomotor coordination [18]. Fronto-parietal cortical networks are related to performance on the DST, and these activations reflect the processes of visual searching and updating of working memory [45]. Since patients with right cerebellar tumors also exhibited impairment of working memory, the intrinsic functional connectivity between the left fronto-parietal network coupled with the right cerebellar hemisphere might be altered by compression. We suspected that the cognitive impairments of patients with right cerebellar tumors were related to alteration of cerebellar contributions to intrinsic functional connectivity. A huge tumor may secondary compress the dentate nucleus of the human cerebellar nuclei as well as direct compression of posterior lateral cerebellum. The nucleus conjuncted with neocortex and reported an important role for human learning and cognition [46].

We found an improvement in the raw scores of some of the neuropsychological tests after surgical intervention associated with anatomical normalization of the lateral posterior cerebellum. At the postoperative stage of neuropsychological estimation, some patients with no improvements in psychomotor speed showed transient neurological symptoms related to the IVth or VIth cranial nerve function. Double vision might be a factor in preventing optimal performance. However, follow-up neuropsychological assessments in patients with cerebellar lesions have been limited [39, 47]. These previous findings [39, 47, 48] might suggest that the cerebellum can recover from pathological insult by changing the relationships of cerebral connectivity. Further studies are required to identify the detailed mechanisms behind the restoration of cognitive function following treatment of cerebellar lesions.

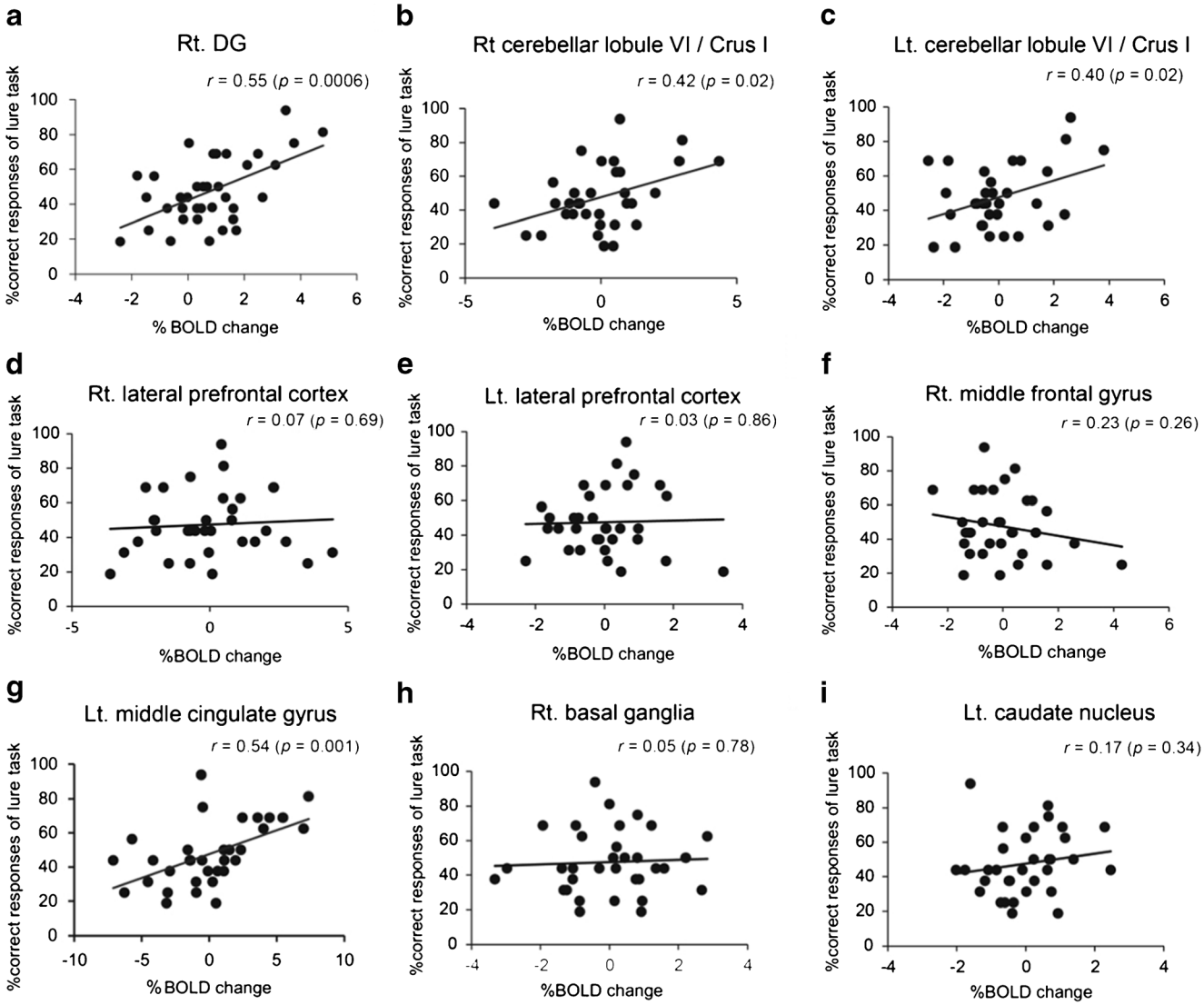

Fig. 6 Regions related to pattern separation ability. Graph (**a** to **i**) showing correlation of percentage of correct responses of the lure task and that of BOLD signals in control subjects (n=30). Hippocampus including dentate gyrus (DG) (**a**), right cerebellar lobule VI including Crus I (lobule VI/Crus I) (**b**), left lobule VI/Crus I (**c**), right lateral prefrontal cortex (**d**), left lateral prefrontal cortex (**e**), right middle frontal cortex (**f**), left middle cingulate gyrus (**g**), right basal ganglia (**h**), and left caudate nucleus (**i**). The percentage of correct responses in the lure task was significantly correlated with BOLD signals in right DG (**a**), right lobule VI/Crus I (**b**), left lobule VI/Crus I (**c**), and left middle cingulate cortex (**g**). No significant relationships were observed in the percentage of BOLD signals in the right and left lateral prefrontal cortex, right middle frontal cortex, right basal ganglia, and left caudate nucleus. The r value indicates the correlation coefficient of the Pearson product–moment (**a**–**i**). The p value indicates the significance level of the correlation coefficient. When the p value is lower than 0.05, the significance of correlation coefficient is accepted. x-axis represents the magnitude of % BOLD change that represents the rate of BOLD signal from stimulus to resting condition. y-axis represents the correct response rate in the lure task

Hippocampal Memory Function in Patients with Cerebellar Tumors

The involvement of the cerebellum in non-declarative memory has been previously investigated. Patients with focal cerebellar lesions showed impaired motor sequencing [10]. Such investigations provide evidence for a cerebellar contribution to procedural learning and support the idea that the cerebellum is an important anatomical component for competent skill acquisition. However, it is still unclear whether cerebellar lesions influence hippocampal episodic memory. On the other hand, the role of the hippocampus in episodic memory has been extensively studied, and the DG subregion of the hippocampus is well known as a substrate for cognition [49].

Pattern separation is a function of the DG that transforms similar experiences or events into discrete, non-overlapping representations. The DG and its projections into the CA3 subregion have been shown to be involved in pattern separation [14]. fMRI was used to observe the process of pattern separation by scanning normal subjects during an incidental

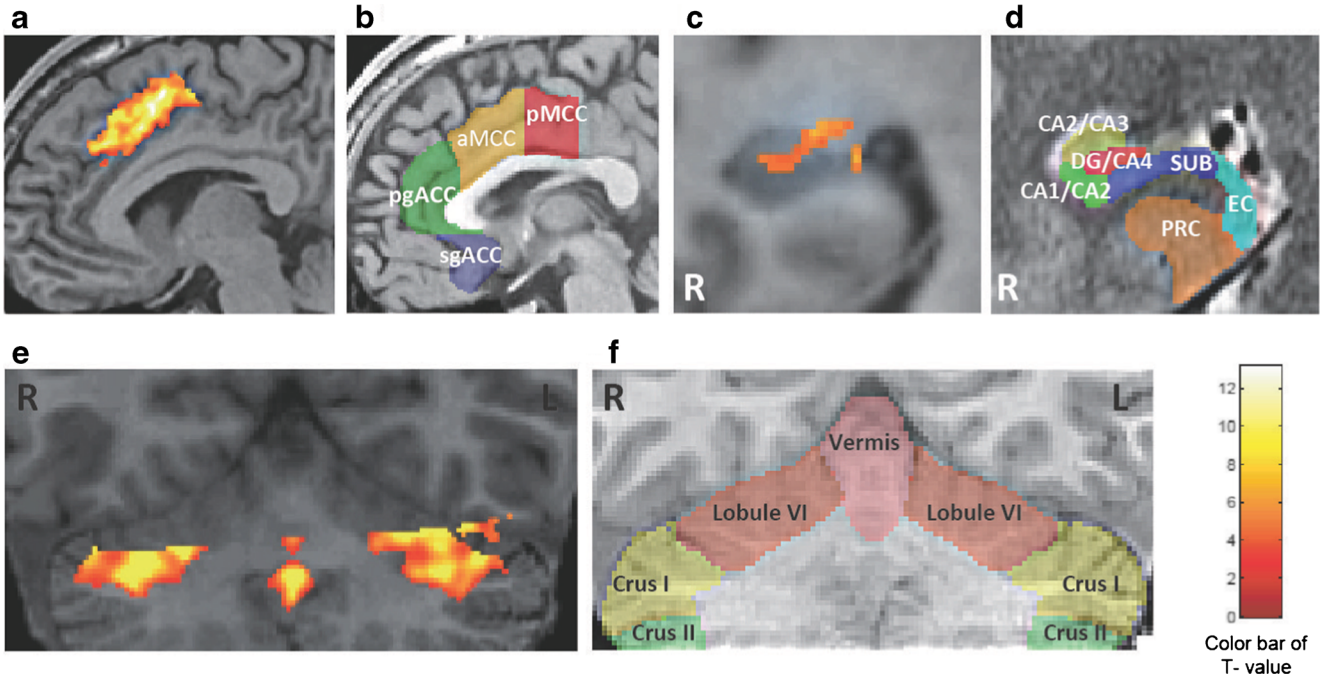

Fig. 7 Identification of source ROIs in the activation maps and topographical schemas in healthy subjects. **a**–**f**. Identification of source ROIs in the activation maps during a lure task from healthy subjects (n= 30, voxel-level threshold at $p<0.001$ uncorrected, corrected for multiple comparisons (family-wise error) to $p<0.05$ using a cluster threshold) (**a**, **c**, and **e**). Each transparent color indicates the subdivisions of the rostral cingulate cortex (**b**), right hippocampus (**d**), and cerebellum (**f**). The color maps were painted according to references [24–27], and are explained in details in the text. **b**, *transparent red*, *yellow*, *green*, and *blue*, indicate the pMCC, posterior mid-cingulate cortex; aMCC, anterior mid-cingulate cortex; pgACC, pregenual anterior cingulate cortex; sgACC, subgenual anterior cingulate cortex, respectively. **d**, *transparent red*, *yellow*, *green*, *blue*, *light blue*, and *orange* indicate the hippocampal dentate gyrus and Cornu Ammonis 4 (DG/CA4); Cornu Ammonis 2 and 3 (CA2/CA3); Cornu Ammonis 1 and 2 (CA1/CA2); subiculum (SUB); entorhinal cortex (EC); and perirhinal cortex (PRC), respectively. **f**, *Transparent pink*, *orange*, *yellow*, and *green* indicate the cerebellar vermis, and bilateral lobule VI, Crus I, and Crus II, respectively. Anatomical identification is specified in the text. Note that the aMCC in **a**, and DG/CA4 in **c**, and lobule VI and/or Crus I in **e** were selectively activated. The *color bar* indicates t values (maximum t=13.18, *white* represents the highest value). *R*, the right hemisphere. *L*, the left hemisphere

encoding task using pictures of common objects. The present fMRI study used a similar experimental paradigm to examine hippocampal memory function involvement in pattern separation in patients with cerebellar tumors. The BOLD response showed that the latency of the positive peak was significantly increased in patients with right cerebellar tumors, and these patients showed increases in the positive peak without any second negative peak. Logothetis et al. [50] reported a linear relationship between BOLD signals and neural activity. In addition, the BOLD signal was shown to represent the proportion of the cerebral blood flow (CBF) and the cerebral metabolic rate of oxygen ($CMRO_2$) [51]. The factor of gain in the positive response was interpreted as either a reduction in CBF or an increase in $CMRO_2$ [52]. Increases in BOLD responses are influenced by hemodynamics and metabolism based on the magnitude of neural response. However, the factor that exerts influence on the increase in positive BOLD responses has not yet been elucidated. Moreover, the physiological significance of the post-stimulus undershoot was interpreted as a normal decline to the resting state of neural activity [50, 53], and reductions in the second negative peak may reflect alteration of the neural responses in patients with right cerebellar tumors. The pattern of averaged BOLD responses did not illustrate the initial dip and post-stimulus undershoot in patients with left cerebellar tumors, which may have been masked by the initial dip and post-stimulus undershoot such that it could not be recognized by means of the extended standard derivation of BOLD responses. These results indicate fluctuations in the large BOLD signals in patients with left cerebellar tumors, though there was not much of a difference between patients with left and right tumors in the size of the lesion and the compressed portion of cerebellum. Further studies are required to examine the causal mechanism of fluctuation in the BOLD signals of patients with left cerebellar tumors.

These findings suggest that the cells surrounding a metabolic disturbance area may have provided appropriate assistance to the hippocampal circuitry. The assessment of hippocampal memory function indicated that patients with cerebellar tumors showed selective inability in a lure task, which reflects pattern separation inability and disturbance of the generating activity of young granule cells in the DG of the hippocampus. This inability was found in patients with both right and left cerebellar tumors, although performances in the other two tasks (new and same) were equal to those of normal

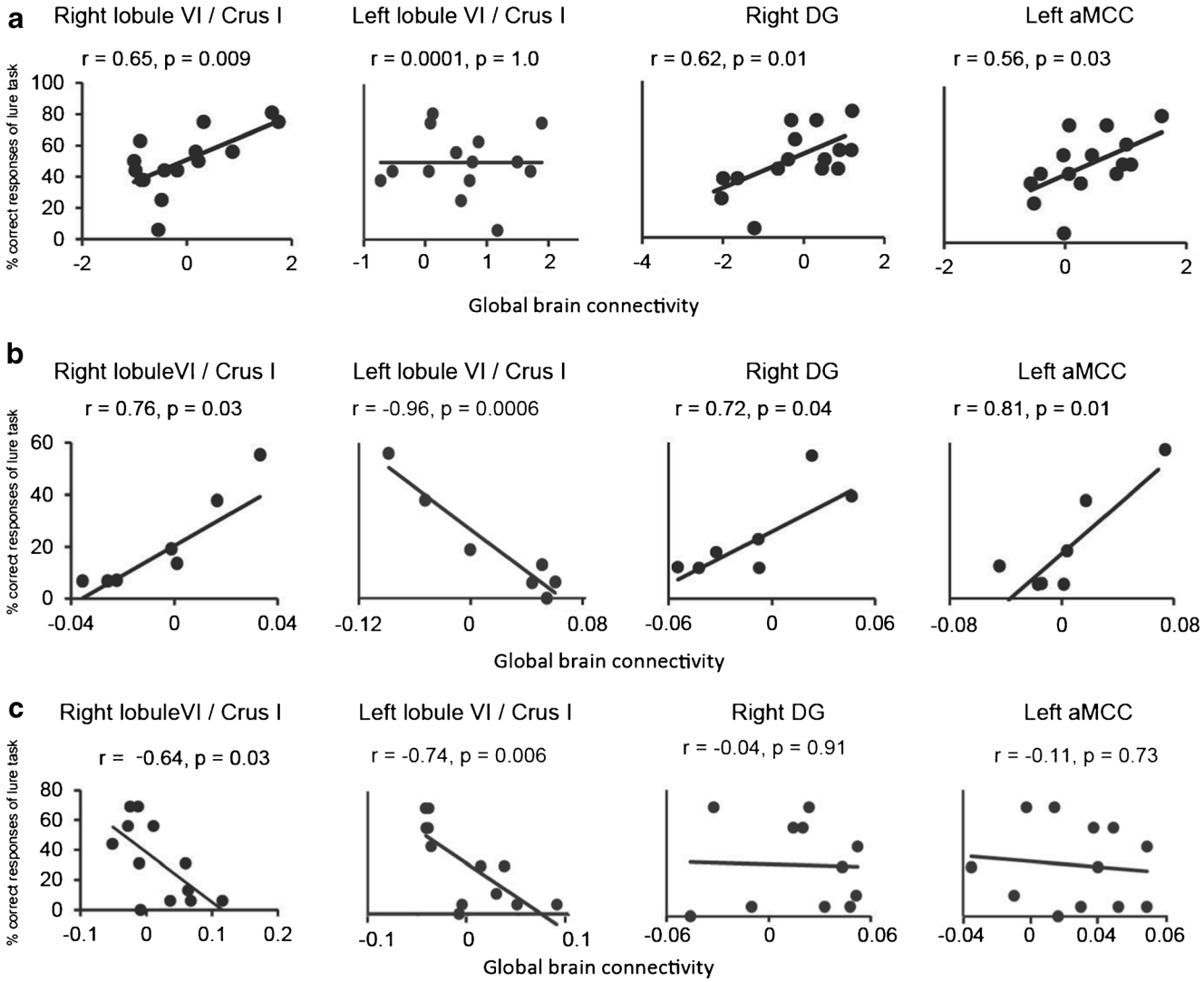

Fig. 8 Correlation of GBC value and pattern separation ability. **a**–**c**. Graphs showing correlation between the correct response rate in the lure task and the GBC value in the right cerebellar lobule VI including Crus I (*lobule VI/Crus I*), left lobule VI/Crus I, right dentate gyrus (DG), and left anterior middle cingulate cortex (*aMCC*). **a** healthy subjects (n=15). **b** patients with left cerebellar tumors (n=7). **c** patients with right cerebellar tumors (n=12). The r value, the correlation coefficient of the Pearson product–moment. The p value, the significance level of correlation coefficient. x-axis, the value of GBC. y-axis, the percentage of correct responses of lure task. Details are described in the text

healthy volunteers. Taken together, these findings indicate that the selective inability in the lure task was caused by cognitive dysfunction and not by motor impairment in patients with cerebellar tumors. Instead, cerebellar damage seems to affect hippocampal DG functions.

Influence on Pattern Separation Function by Global Brain Connectivity of Posterior Lateral Cerebellum

The fMRI examination of cognitive processing observed cerebellar activity in the convergent area of the posterior lateral lobe, which also regulates smooth motor control. Activations of posterior lateral cerebellum were previously proposed as the internal model for new tools [7]. Our present GBC study demonstrated that the value was altered in patients with cerebellar tumors compared with the normal control group. Interestingly, the left and right values of patients with cerebellar tumors converged on a narrow window. It was reported that cerebellum, cingulate cortex, and hippocampus have high GBC values that are included in the top 10 % of GBC [29]. High GBC areas have more connectivity with cortical and subcortical regions [29]. The GBC values that were restricted within the narrow window may represent a reduction in connectivity induced by lesions to the posterior lateral cerebellum.

Our present study also showed that the right cerebellar lobule VI/Curs I, right DG, and left aMCC are important regions for pattern separation. In particular, patients with right cerebellar tumors showed a disruption in the correlation of GBC to these areas associated with pattern separation function. High GBC areas are believed to integrate cortical and

subcortical activity and act as global hubs influencing cognitive control [29, 30]. According to resting-state fMRI analysis, it was reported that the posterior cerebellum has a functional connection with the prefrontal cortex, involving the anterior cingulate cortex for cognitive functions [8, 9]. Reduction in the GBC of patients with right cerebellar tumors not only elicited functional dissociation of the right and left lobule VI/Curs I from pattern separation ability but also affected the anterior mid-cingulate cortex and hippocampus. In light of these observations, global connectivity of the right posterior lateral cerebellum may play an important role in pattern separation as well as cognitive functions.

Interaction between the hippocampus and cerebellum occurs in the spatial domain [54]. Cerebellar impairment leads to dysfunction of the spatial cord as recorded by place cells in the CA1 hippocampus using L7-PKCI mice in which protein kinase C-dependent long-term depression at the parallel fiber-Purkinje cell synapses is blocked. Consequently, the cerebellum assists navigation by participating in the building of the hippocampal spatial map. Hippocampal-cerebellar interactions occur during spatio-temporal prediction [55]. Patients with right cerebellar tumors showed a high rate of error in the lure task, as was indicated by fMRI. Just as the cerebellum contributes to the fine tuning of coordination in skilled motor sequences in motor control, it also contributes to cognition by facilitating the precise discrimination of overlapping or similar experiences among episodic memories. Newly generated young neurons have been shown to facilitate pattern separation in the hippocampus [49]. Whether cognitive decline and disability in pattern separation in patients with cerebellar disease only reflect functional changes in new neurons or are instead associated with a decrease in hippocampal neurogenesis is an interesting question that requires further investigation.

Conclusions

The present findings show that compression of the posterior lateral cerebellum causes impairment of cognitive function. Surgical decompression of the cerebellum facilitated cognitive recovery. The fMRI study demonstrated global connectivity between the Crus I, aMCC, and hippocampus during analysis of hippocampal memory function. The posterior lateral cerebellum acts as a global hub, cooperating with the hippocampus and anterior mid-cingulate cortex to facilitate pattern separation ability.

Acknowledgments This work was supported by the Industrial Disease Clinical Research Grants by the Ministry of Health, Labour and Welfare (to S.I., T.W., Y.H., and M.N.), and Special Account Budget for Education and Research (to S.I., and M.T.), Grants-in-Aid for Scientific Research (B) (23390352) (to S.I.), and Challenging Exploratory Research (24650168) (to S.I.) by the Ministry of Education, Culture, Sports, Science and Technology in Japan, and the Princess Takamatsu Cancer Fund (to S.I.), and the Grants for Takeda Science Foundation (to M.T., and S.I.).

Conflict of Interest The authors declare that they have no conflict of interest.

Author Contributions A.S. and M.N. prepared the manuscript; A.S. and D.T. performed neuropsychological analysis; M.N. and S.M. analyzed fMRI data; H.N., T.M., Y.H., and T.W. handled the clinical management; and S.I. designed and administered this study and wrote the manuscript. All authors edited the manuscript.

References

1. Manto M, Bower JM, Conforto AB, Delgado-García JM, da Guarda SN, Gerwig M, et al. Consensus paper: roles of the cerebellum in motor control—the diversity of ideas on cerebellar involvement in movement. Cerebellum. 2012;11:457–87.
2. Grimaldi G, Manto M. Topography of cerebellar deficits in humans. Cerebellum. 2012;11:336–51.
3. Riva D, Annunziata S, Contarino V, Erbetta A, Aquino D, Bulgheroni S. Gray matter reduction in the vermis and CRUS-II is associated with social and interaction deficits in low-functioning children with autistic spectrum disorders: a VBM-DARTEL Study. Cerebellum. 2013;12:676–85.
4. Koziol LF, Budding D, Andreasen N, D'Arrigo S, Bulgheroni S, Imamizu H, et al. Consensus paper: the cerebellum's role in movement and cognition. Cerebellum. 2014;13:151–77.
5. Koziol LF, Budding DE, Chidekel D. From movement to thought: executive function, embodied cognition, and the cerebellum. Cerebellum. 2012;11:505–25.
6. Schmahmann JD, Sherman JC. The cerebellar cognitive affective syndrome. Brain. 1998;121(4):561–79.
7. Imamizu H, Miyauchi S, Tamada T, Sasaki Y, Takino R, Pütz B, et al. Human cerebellar activity reflecting an acquired internal model of a new tool. Nature. 2000;403:192–5.
8. Habas C, Kamdar N, Nguyen D, Prater K, Beckmann CF, Menon V, et al. Distinct cerebellar contributions to intrinsic connectivity networks. J Neurosci. 2009;29:8586–94.
9. Krienen FM, Buckner RL. Segregated fronto-cerebellar circuits revealed by intrinsic functional connectivity. Cereb Cortex. 2009;19:2485–97.
10. Molinari M, Leggio MG, Solida A, Ciorra R, Misciagna S, Silveri MC, et al. Cerebellum and procedural learning: evidence from focal cerebellar lesions. Brain. 1997;120(Pt 10):1753–62.
11. Chen SH, Desmond JE. Cerebrocerebellar networks during articulatory rehearsal and verbal working memory tasks. Neuroimage. 2005;24:332–8.
12. Marvel CL, Desmond JE. Functional topography of the cerebellum in verbal working memory. Neuropsychol Rev. 2010;20:271–9.
13. Ravizza SM, McCormick CA, Schlerf JE, Justus T, Ivry RB, Fiez JA. Cerebellar damage produces selective deficits in verbal working memory. Brain. 2006;129:306–20.

14. Bakker A, Kirwan CB, Miller M, Stark CE. Pattern separation in the human hippocampal CA3 and dentate gyrus. Science. 2008;319:1640–2.
15. Schmahmann JD, Gardner R, MacMore J, Vangel MG. Development of a brief ataxia rating scale (BARS) based on a modified form of the ICARS. Mov Disord. 2009;24:1820–8.
16. Folstein MF, Folstein SE, McHugh PR. "Mini-mental state". A practical method for grading the cognitive state of patients for the clinician. J Psychiatr Res. 1975;12:189–98.
17. Teng EL, Chui HC. The Modified Mini-Mental State (3MS) examination. J Clin Psychiatry. 1987;48:314–8.
18. Lezak MD, Howieson DB, Loring DW. Orientation and attention. In: Neuropsychological assessment 4th ed. New York: Oxford University Press; 2004 pp. 365–8, 371–4.
19. Wechsler D. Manual for the Wechsler adult intelligence scale—revised. New York: Psychological Corporation; 1981.
20. Maeshima S, Osawa A, Maeshima E, Shimamoto Y, Sekiguchi E, Kakishita K, et al. Usefulness of a cube-copying test in outpatients with dementia. Brain Inj. 2004;18:889–98.
21. Burock MA, Buckner RL, Woldorff MG, Rosen BR, Dale AM. Randomized event-related experimental designs allow for extremely rapid presentation rates using functional MRI. Neuroreport. 1998;9:3735–9.
22. Yassa MA, Stark SM, Bakker A, Albert MS, Gallagher M, Stark CE. High-resolution structural and functional MRI of hippocampal CA3 and dentate gyrus in patients with amnestic mild cognitive impairment. Neuroimage. 2010;51:1242–52.
23. Friston KJ, Holmes AP, Poline JB, Grasby PJ, Williams SC, Frackowiak RS, et al. Analysis of fMRI time-series revisited. Neuroimage. 1995;2:45–53.
24. Tzourio-Mazoyer N, Landeau B, Papathanassiou D, Crivello F, Etard O, Delcroix N, et al. Automated anatomical labeling of activations in SPM using a macroscopic anatomical parcellation of the MNI MRI single-subject brain. Neuroimage. 2002;15:273–89.
25. Schmahmann JD, Doyon J, McDonald D, Holmes C, Lavoie K, Hurwitz AS, et al. Three-dimensional MRI atlas of the human cerebellum in proportional stereotaxic space. Neuroimage. 1999;10:233–60.
26. Duvernoy HM. The human hippocampus: functional anatomy, vascularization and serial sections with MRI. Berlin: Springer Verlag; 2005.
27. Vogt BA, editor. Cingulate neurobiology and disease. NY: Oxford University Press; 2009.
28. Matthew Brett, Jean-Luc Anton, Romain Valabregue, Jean-Baptiste Poline. Region of interest analysis using an SPM toolbox [abstract] Presented at the 8th International Conference on Functional Mapping of the Human Brain, June 2–6, 2002, Sendai, Japan. Available on CD-ROM in NeuroImage, Vol 16, No 2.
29. Cole MW, Pathak S, Schneider W. Identifying the brain's most globally connected regions. Neuroimage. 2010;49:3132–48.
30. Cole MW, Yarkoni T, Repovs G, Anticevic A, Braver TS. Global connectivity of prefrontal cortex predicts cognitive control and intelligence. J Neurosci. 2012;32:8988–99.
31. Fisher RA. Frequency distribution of the values of the correlation coefficient in samples from an indefinitely large population. Biometrika. 1915;10:507–21.
32. Mukaka MM. Statistics corner: a guide to appropriate use of correlation coefficient in medical research. Malawi Med J. 2012;24:69–71.
33. Honey CJ et al. Predicting human resting-state functional connectivity from structural connectivity. Proc Natl Acad Sci U S A. 2009;106:2035–40.
34. Smith SM et al. Correspondence of the brain's functional architecture during activation and rest. Proc Natl Acad Sci U S A. 2009;106:13040–5.
35. Riva D, Giorgi C. The cerebellum contributes to higher functions during development: evidence from a series of children surgically treated for posterior fossa tumours. Brain. 2000;123:1051–61.
36. Baillieux H, De Smet HJ, Dobbeleir A, Paquier PF, De Deyn PP, Mariën P. Cognitive and affective disturbances following focal cerebellar damage in adults: a neuropsychological and SPECT study. Cortex. 2010;46:869–79.
37. Gottwald B, Mihajlovic Z, Wilde B, Mehdorn HM. Does the cerebellum contribute to specific aspects of attention? Neuropsychologia. 2003;41:1452–60.
38. Gottwald B, Wilde B, Mihajlovic Z, Mehdorn HM. Evidence for distinct cognitive deficits after focal cerebellar lesions. J Neurol Neurosurg Psychiatry. 2004;75:1524–31.
39. Hokkanen LS, Kauranen V, Roine RO, Salonen O, Kotila M. Subtle cognitive deficits after cerebellar infarcts. Eur J Neurol. 2006;13:161–70.
40. Stoodley CJ, Schmahmann JD. Functional topography in the human cerebellum: a meta-analysis of neuroimaging studies. Neuroimage. 2009;44:489–501.
41. Stoodley CJ, Valera EM, Schmahmann JD. Functional topography of the cerebellum for motor and cognitive tasks: an fMRI study. Neuroimage. 2012;59:1560–70.
42. Wang D, Buckner RL, Liu H. Cerebellar asymmetry and its relation to cerebral asymmetry estimated by intrinsic functional connectivity. J Neurophysiol. 2013;109:46–57.
43. Wang D, Buckner RL, Liu H. Functional specialization in the human brain estimated by intrinsic hemispheric interaction. J Neurosci. 2014;34:12341–52.
44. Kirschen MP et al. Verbal memory impairments in children after cerebellar tumor resection. Behav Neurol. 2008;20:39–53.
45. Usui N et al. Cortical areas related to performance of WAIS Digit Symbol Test: a functional imaging study. Neurosci Lett. 2009;463:1–5.
46. Habas C. Functional imaging of the deep cerebellar nuclei: a review. Cerebellum. 2010;9:22–8.
47. Neau JP, Arroyo-Anllo E, Bonnaud V, Ingrand P, Gil R. Neuropsychological disturbances in cerebellar infarcts. Acta Neurol Scand. 2000;102:363–70.
48. O'Halloran CJ, Kinsella GJ, Storey E. The cerebellum and neuropsychological functioning: a critical review. J Clin Exp Neuropsychol. 2012;34:35–56.
49. Nakashiba T, Cushman JD, Pelkey KA, Renaudineau S, Buhl DL, McHugh TJ, et al. Young dentate granule cells mediate pattern separation, whereas old granule cells facilitate pattern completion. Cell. 2012;149:188–201.
50. Logothetis NK, Pauls J, Augath M, Trinath T, Oeltermann A. Neurophysiological investigation of the basis of the fMRI signal. Nature. 2001;412:150–7.
51. Schridde U, Khubchandani M, Motelow JE, Sanganahalli BG, Hyder F, Blumenfeld H. Negative BOLD with large increases in neuronal activity. Cereb Cortex. 2008;18:1814–27.
52. Hu X, Yacoub E. The story of the initial dip in fMRI. Neuroimage. 2012;62:1103–8.
53. Shmuel A, Augath M, Oeltermann A, Logothetis NK. Negative functional MRI response correlates with decreases in neuronal activity in monkey visual area V1. Nat Neurosci. 2006;9:569–77.
54. Rochefort C, Arabo A, André M, Poucet B, Save E, Rondi-Reig L. Cerebellum shapes hippocampal spatial code. Science. 2011;334:385–9.
55. Onuki Y, Van Someren EJ, De Zeeuw CI, Van der Werf YD. Hippocampal-cerebellar interaction during spatio-temporal prediction. Cereb Cortex. 2015;25(2):313–21.

IX. 脳腫瘍の治療

脳腫瘍の放射線療法

放射線療法：概論

Radiotherapy for the patients with brain tumours

石内勝吾

Key words：脳腫瘍，放射線治療，海馬，神経新生，neurocognition

はじめに

放射線は固形がんの治療において，重要な治療手段である．純型胚細胞腫のように放射線と化学療法を組み合わせることで治癒しうる疾患から，腫瘍塊に90 Gy相当以上の照射を施行しても，照射野内外での腫瘍の再発がしばしば起こる神経膠芽腫に代表される悪性脳腫瘍においても大切な治療手段であることに変わりない[1-3]．技術革新の進歩により従来型のライナックによる外照射のみならずガンマナイフやサイバーナイフを組み合わせて高精度放射線治療を施行するなどの工夫，ホウ素中性子補足療法のような浸潤最先端の腫瘍細胞を標的とする新規治療法も臨床応用されている．とりわけ悪性度の高い神経膠芽腫については，様々な試みが施行されているが，長期の質を維持した生存期間を得る症例は依然少数にとどまる．次世代の放射線治療として期待されている粒子線は質量をもつ放射線であり陽子線(^{1}H)，ヘリウムイオン(^{4}He)，中間子，中性子，重イオン(炭素^{12}C，ネオン^{20}Ne，アルゴン^{40}Ar)に大別され，質量をもたない光子(X線，γ線)や電子線と区別される[4]．粒子線の物理特性で最も重要なことは線量分布が深部でピーク(Bragg peak)をもつことである．これにより良好な空間線量分布を得ることができ，正常組織への被曝を極力抑えることが可能となる．またX線，γ線が単位長あたりに付与するエネルギー(linear energy transfer: LET)が低い低LET放射線であるのに対して，粒子線は高LET放射線であり生物学的効果比(relative biological effectiveness: RBE)が高いことも重要な特性である．RBEに関しては陽子線はX線とほぼ同様の1.1であるが炭素線は3であり，同等の生物学的効果を起こすのにX線が物理線量で3 Gy必要なら炭素線は1 Gy，陽子線は2.7 Gy照射すればよいことになる．小児脳腫瘍と手術不能な骨軟部腫瘍は保険収載された．炭素線を用いた治療システムは本邦が世界に先駆けて開発しているがん細胞をその形状に沿って攻撃する高速3Dスキャニングによる方法や正常組織を回避して選択的に腫瘍を殺傷する回転ガントリーの導入など，今後実臨床の場でのその成果の検証が期待されている．

本稿では悪性脳腫瘍を中心に放射線治療の適応を概説し，また最近注目されている放射線がヒト認知能に及ぼす影響や患者の生活quality of life(QOL)を高めるための試みについても言

Shogo Ishiuchi: Department of Neurosurgery, University of the Ryukyus, Graduate School of Medicine 琉球大学大学院医学研究科 脳神経科分野

0047-1852/16/¥60/頁/JCOPY

及したい.

1. 神経膠芽腫に対する放射線治療

放射線治療計画に関わる標的体積にはMRI造影領域として肉眼的腫瘍体積(gross tumor volume: GTV)にMRI T2強調画像での高吸収域+2 cmまたはMRI FLAIR画像での高吸収域+2 cmの領域にメチオニンPETなどを参考に臨床標的体積(clinical target volume: CTV)を設定しこれらに基づいて計画標的体積(planning target volume: PTV)を決定する. 1p19qの遺伝子共欠失がないIDH1/2野生型の原発性神経膠芽腫ではCTVにIMRT(intensity-modulated radiation therapy)にて40 Gyを, ついでGTVに20 Gyのブーストをtemozolomide(TMZ)内服下(75 mg/m^2)に行うのが標準治療である[5](図1). 腫瘍塊部を放射線単独でアポトーシスを引き起こすためには90 Gy程度の高線量照射が必要とされるが, 過去の臨床治験の成績からは高線量放射線では放射線壊死が必発であり患者のQOLを維持できない[1]. また生存するに従い遠隔転移率が60 Gyの標準治療と比較して増加する[2,3]. 分子基盤に基づいてMGMT非メチル化症例でTMZに反応を示さない症例には今後免疫療法や免疫チェックポイント阻害剤の応用が取り入れられるであろう. これらの治療には腫瘍ペプチドワクチン療法WT1やさらに百日咳菌体をアジュバントしたWT1-W10, メラノーマの臨床治験で効果を上げている抗PD-1(programmed cell death-1)抗体療法などT細胞の免疫応答にかけられたブレーキを解除することでT細胞の活性化状態を維持しがん細胞を細胞死に追いやる試みである. 同じくT細胞の表面に発現する抑制性因子CTLA-4(cytotoxic T-lymphocyte-associated antigen-4)に対する抗体の併用も期待されている.

2. Lower-grade gliomaの治療

1p19q共欠失を認めIDH1が変異型のLower-grade gliomaでは, 全摘出可能であった症例では放射線化学療法は行わずしばらく経過を見てもよいだろう. 浸潤部位や残存がある症例では46-54 Gy程度の放射線治療をIMRTで併用する. 術直後から併用しても再燃・増悪時に併用してもoverall survivalには有意差はないが(OS: 7.2年 vs 7.4年)初回から併用したほうが制御率は向上する(PPF; 5.3年 vs 3.4年)[6]. 従来diffuse astrocytomaあるいはanaplastic astrocytomaと診断された症例の遺伝子異常に着目した分類が最近報告された[7]. grade II, IIIのグリオーマを分子表現型によりType I, II, IIIa, IIIbに分けるものである. Type IはIDH変異があり同時に1p19q共欠失がありTERT変異を併発(テロメレース活性が高くテロメア伸長機能が亢進)する従来のgrade II/III oligodendrogliomaに相当する. Type IIはIDH変異があるが1p19q共欠失なくATRX変異(クロマチン修復に関連)を併発するタイプで従来の星細胞腫に相当する腫瘍群であり, Type IIIはIDHの変異はなく, 組織悪性度がgrade II相当のType IIIaと, 組織悪性度grade III相当のType IIIbで従来のanaplastic astrocytomaに相当する. 今後はこれら分子マーカーも参考にした放射線化学療法の差別化が行われることになろう.

3. 毛様性星細胞腫, 上衣腫, 胚細胞腫, 髄芽腫

1) 毛様性星細胞腫(pilocytic astrocytoma: PA)

小脳に好発する良性(grade I)の星細胞腫では, 全摘出できれば放射線化学療法の必要はない. 視床下部や視交叉に発生したものでは進行すると大脳基底核に浸潤する. 延髄下部や橋など脳幹実質に浸潤している症例では全摘出は困難でIMRT照射45-56 Gyを施行する. カルボプラチン, ビンクリスチンを用いた化学療法は約半数で有効である. 小脳PAではtandem duplicationによるBRAF遺伝子との癒合が, テント上のPAではV600Eの点変異の症例が認められるが, 悪性黒色腫で保険適応化されたBRAF阻害剤の有効性は今後の検討課題である[8].

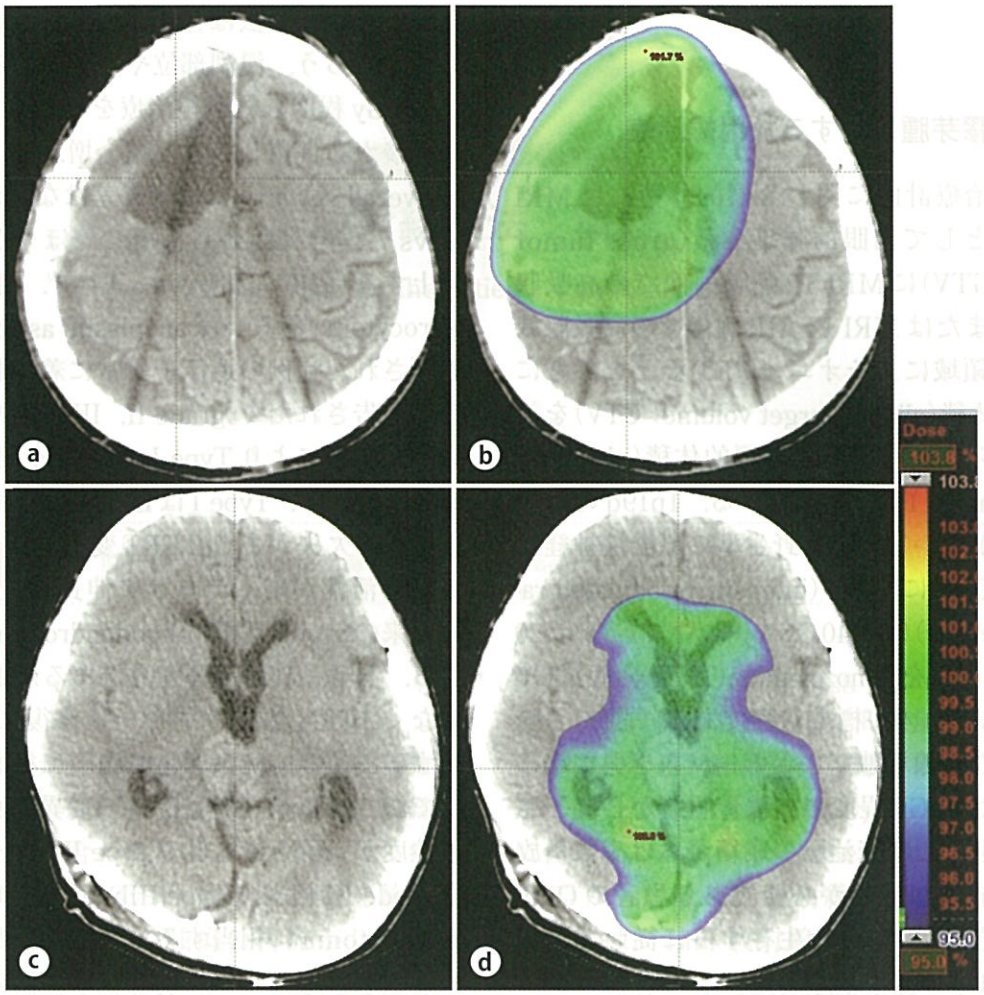

図1　IMRTを用いた悪性脳腫瘍の線量計画

a. 右側前頭葉神経膠芽腫術後のCT画像.

b. FLAIR画像の摘出腔から2 cmのマージンをとったplanning target volume（PTV）に40 Gy（2 Gy×20 fractions），その後摘出腔に20 Gy（2 Gy×10 fractions）のブースト照射を施行.

c. 松果体胚細胞腫の術前のCT画像.

d. PTVは脳室を含む領域に27 Gy（1.8 Gy×15 fractions），その後腫瘍塊に18 Gy（1.8 Gy×10 fractions）ブースト照射を施行.

手術は生検を施行し線量計画は術前画像を用いている.

2）上衣腫

原発性脳腫瘍に占める（2001–2004年全国脳腫瘍統計第13版）上衣腫，退形成性上衣腫の頻度および5年生存率はそれぞれ0.5％，0.4％および88.5％，58.1％である．小児では後頭蓋窩腫瘍が多く，脊髄，大脳にも発生する．Radial glial cellsを発生起源とする説がある．その発育形式は浸潤性格を有するが神経膠芽腫ほどではなく，可塑性を有する発育態度はしばしばルシュカ孔を超えて外側へも進展し，外科的摘出を困難にする．テント上の症例でマージンをとり全摘出を達成できた症例の予後は良好である．grade III，あるいは脳幹浸潤などで全摘出できない場合は白金錯体であるカルボプラチンやシスプラチンにエトポシドを併用した化学療法にIMRTによる46–54 Gy程度の放射線化学療法を併用する．髄液播種が認められた場合は全中枢神経系照射を施行する．本邦では上衣腫の頻度が低いために遺伝子診断は確立されておらず，また予後を規定するバイオマーカーも実用化されていない．grade IIで残存が疑われる症例と退形成性上衣腫に対しては50 Gy以上の放射線

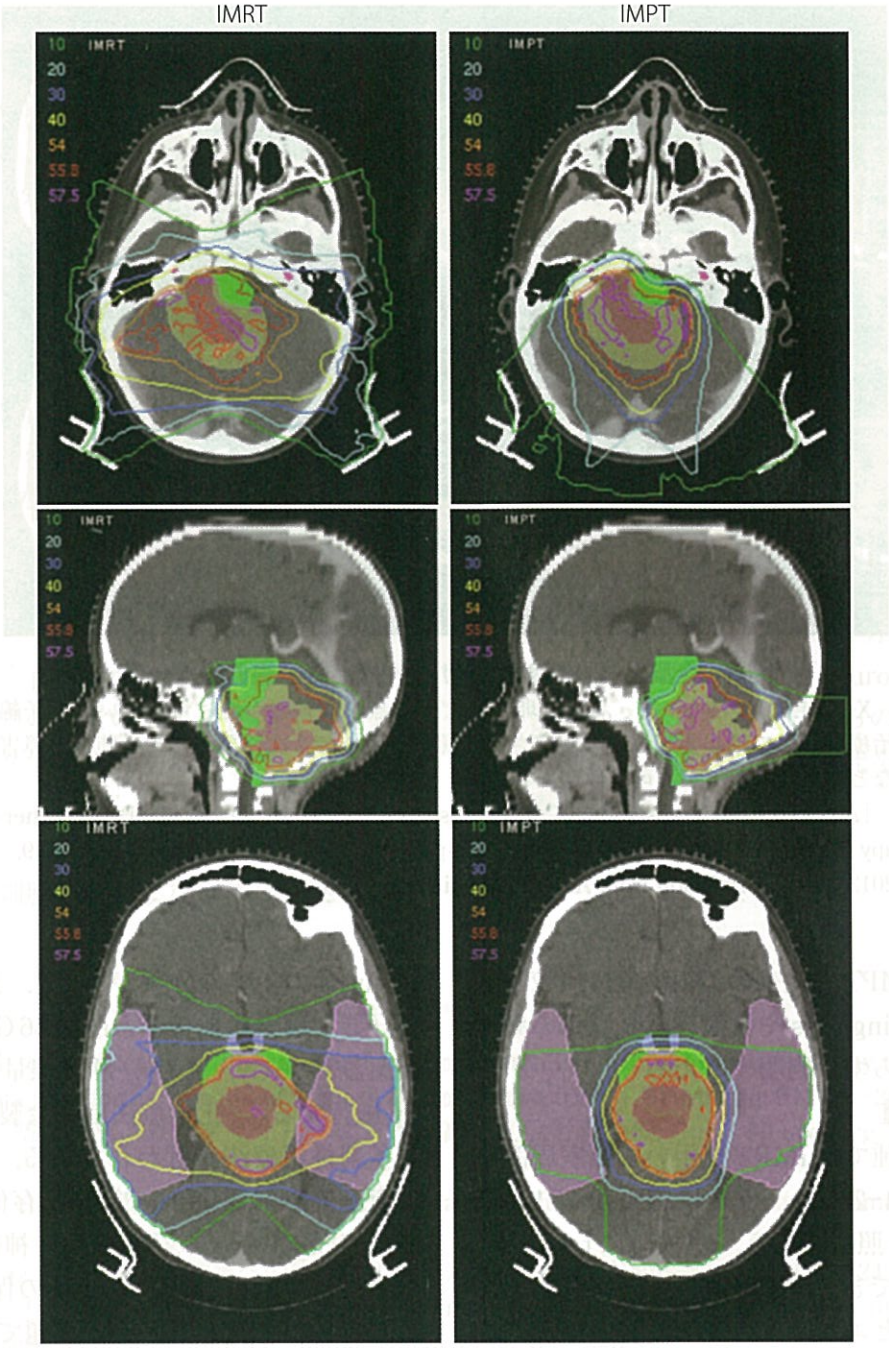

図2　IMRTとIMPT

後頭蓋窩 ependymoma 症例の axial，sagittal dosimetry を上段と中段に，テント上 ependymoma の線量計画を下段 axial view に示す．IMPT は IMRT に比較して蝸牛神経，脳幹，脳下垂体および側頭葉の被曝を防ぐことができる．

［Reprinted from International Journal of Radiation Oncology, Biology, Physics, 71, MacDonald SM, et al, Proton radiotherapy for childhood ependymoma: initial clinical outcomes and dose comparisons, p979–986, Copyright(2008), with permission from Elsevier.］

治療を併用する．小児の ependymoma においては放射線治療は必須であるためプロトンビームを用いた IMPT(intensity modulated proton beam radiation therapy)と従来型の IMRT との比較検証が行われている(**図2**)．IMPT の応用により蝸牛神経，脳下垂体，小脳，側頭葉などの正常脳組織のスペアリングがより改善され治療線量計画に優れ正常組織の保護がより細密に

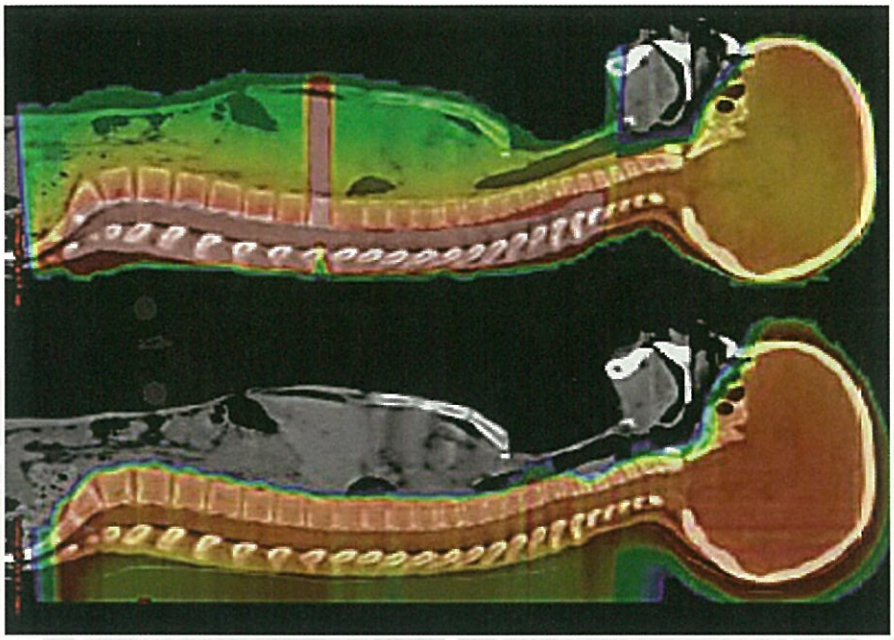

図3　全脳全脊髄照射におけるX線と陽子線の線量分布

X線（上段）では心・肺・胃腸・卵巣などへの無駄な被曝が避けられないが陽子線治療（下段）では必要部位への限定された照射が可能で2次性発がんや心肺機能障害などのリスクが下がる可能性がある．

［Adapted from Translational Cancer Research, 1, Dinh JQ, et al, Particle therapy for central nervous system tumors in pediatric and adult patients, p137–149, 2012, with permission from AME Publishing Company.］

なる[9]．今後IMPTが従来のX線治療に比較してどの程度hearing lossや放射線誘発腫瘍の頻度の低下をもたらすか判明するだろう．

3）胚細胞腫

純型胚細胞腫ではIMRTを用いて脳室周囲を含む領域に24–27 Gy，さらに腫瘍塊に12–18 Gyのブースト照射を行う．生検時にteratomaの成分が確認できれば全摘出を行う（**図1**）．カルボプラチンとエトポシドによる化学療法は放射線治療をはさむ形で放射線治療前と治療後に行う．さらに放射線治療終了後に3クール施行し地固めをする．播種がある場合のみ脊髄照射を併用する．純型胚細胞腫は化学放射線療法で治癒しうる疾患であるが成人後の神経内分泌機能障害や2次性発がんのリスクを下げる線量計画や化学療法の工夫が必要となる（**図2**）．

4）髄芽腫

Molecular subgroupとして予後の良いWNT medulloblastoma，最も予後の悪いGroup 3，intermediate–prognosisのSonic hedgehog（SHH），Group 4の4型の分類がある[10]．悪性群および良好群では全中枢神経系照射36 Gy，23.6 Gy，後頭蓋窩36 Gy，36 Gy，腫瘍線量55.8 Gy，55.8 Gy施行する[11]．化学療法は白金製剤を中心とする多剤併用療法が行われている．5年生存率は手術全摘出例で93％，術後残存例で56％，播種例で38％である．脳神経，神経内分泌器官への放射線量の低減，認知能の保護や改善，2次性腫瘍のリスクの回避が課題である．X線に代わり陽子線治療を応用することで全脳全脊髄照射による心，肺，胃腸，卵巣などの被曝を避けられるのは大きなアドバンテージといえるだろう[12]（**図3**）．

4. 放射線治療の認知能に対する影響

中枢神経系に対して全脳照射治療後半年を経た患者の50–90％に認知能障害が認められる[13]．記憶障害（spacial memory，and verbal memory），注意障害および新規課題に関する解決能

力の低下が顕著となる．放射線は多種類の脳の構成細胞に影響を与える．放射線による脳機能障害は血管内皮障害に起因するvasculopathyと微小環境における栄養不全，星細胞に由来するastrocytosisと栄養障害，希突起細胞の障害から起こる白質障害と神経伝達障害，神経細胞に対してはmaturation deficiencyとシナプス機能の変質，microgliaによるneuroinflammationなどが相互に関連しながら引き起こされる現象である．とりわけ海馬歯状回部の神経新生能低下は患者の記憶と学習能力を大きく阻害する．両側海馬の40％の領域に7.3 Gy以上の線量があたると認知障害が引き起こされるとの報告がある[14]．今後は放射線治療患者の認知能障害を防御する第一歩としてfMRIを用いて海馬神経新生能を反映するpattern separation taskを応用し放射線治療中の患者の海馬の機能を非侵襲的にモニタリングする必要があろう[15]．

おわりに

細胞起源，細胞形態および組織構築に着眼する従来の病理診断から，近年の分子生物学的解析の成果を取り入れた新しいWHO分類では予後診断の精度が高まった分類が作成された．さらに最新の研究からは腫瘍内の遺伝子変化の多様性や悪性転換の様相の一部が明らかにされつつある．その一方でIMRTによる放射線治療にtemozolomideやbevacizumabを用いた現行の治療法では予後の大きな改善が認められないばかりか，一時的な寛解後に起こる急速な浸潤性増殖の悪化という従来とは異なる再燃像が認められるようになってきた．放射線治療を基盤とした悪性グリオーマに対する根本治療を創出して患者QOLを高めるために今後行われなければならない課題は以下の3つに集約できよう．①浸潤性増殖の分子機構の解明，②放射線抵抗性の機序の解明，③患者neurocognitionの評価と治療の3点である．これらの課題を踏まえて精力的に臨床研究と基礎研究を推進することが肝要である．

文献

1) Fitzek MM, et al: Accelerated fractionated proton/photon irradiation to 90 cobalt gray equivalent for glioblastoma multiforme: results of a phase II prospective trial. J Neurosurg **91**: 251–269, 1999.
2) 井内俊彦，幡野和男：悪性グリオーマに対する高精度放射線治療．Jpn J Neurosurg **21**: 207–215, 2012.
3) Tanaka M, et al: High-dose conformal radiotherapy for supratentorial malignant glioma: a historical comparison. Lancet Oncol **12**: 953–960, 2005.
4) 石内勝吾：粒子線治療の脳腫瘍への臨床応用と将来展望．Jpn J Neurosurg **22**: 117–124, 2013.
5) Fuller CD, et al: Standard fractionation intensity modulated radiation therapy(IMRT) of primary and recurrent glioblastoma multiforme. Radiat Oncol **2**: 26–32, 2007.
6) van den Bent MJ, et al: Long-term efficacy of early versus delayed radiotherapy for low grade astrocytoma and oligodendroglioma in adults: the EORTC 22845 randomised trial. Lancet **366**: 985–990, 2005.
7) Suzuki H, et al: Mutational landscape and clonal architecture in grade II and III gliomas. Nat Genet **47**: 458–468, 2015.
8) Jones DT, et al: Tandem duplication producing a novel oncogenic BRAF fusion gene defines the majority of pilocytic astrocytomas. Cancer Res **68**: 8673–8677, 2008.
9) MacDonald SM, et al: Proton radiotherapy for childhood ependymoma: Initial clinical outcomes and dose comparisons. Int J Radiat Oncol Biol Phys **71**: 979–986, 2008.
10) Northcott PA, et al: Molecular subgroups of medulloblastoma. Expert Rev Neurother **12**: 871–884, 2012.
11) Rutkowski S, et al: Treatment of early childhood medulloblastoma by postoperative chemotherapy alone. N Eng J Med **352**: 978–986, 2005.

12) Dinh JQ, et al: Particle therapy for central nervous system tumors in pediatric and adult patients. Transl Cancer Res 1: 137-149, 2012.
13) Greene-Schloesser D, et al: Radiation-induced brain injury: a review. Front Oncol 2: 1-14, 2012.
14) Gondi V, et al: Hippocampal dosimetry predicts neurocognitive function impairment after fractionated stereotactic radiotherapy for benign or low-grade adult brain tumors. Inst Radiat Oncol Biol Phys 83: 487-493, 2012.
15) Shiroma A, et al: Cerebellar contribution to pattern separation of human hippocampal memory circuits. Cerebellum, 2015 Oct 6: 1-18.

膠芽腫〔GBM: glioblastoma multiforme〕

公開日：2017/03/21

企画・制作 ケアネット

インデックスページへ戻る

このコンテンツでは、希少疾病に関しての基本情報・診断・治療などを解説していきます。
今後も随時、追加・更新していきますので、ぜひご活用ください。

希少疾病ライブラリ

講師紹介

石内 勝吾（いしうち しょうご）氏
琉球大学医学部 脳神経外科学 教授

1 疾患概要

■ 概念・定義

膠芽腫（glioblastoma multiforme: GBM）は、悪性脳腫瘍の中で最も頻度が高く、かつ生物学的にもっとも未分化な予後不良の悪性新生物（brain cancer）である。高齢者の大脳半球、ことに前頭葉と側頭葉に好発し、浸潤性増殖を特徴とする。

病理学的に腫瘍細胞は異型性が強く、未分化細胞、類円形細胞、紡錘形細胞、多角細胞および多核巨細胞より構成され、壊死を取り囲む偽柵状配列を特徴とする（pseudopalisading necrosis）。

WHO grade IVに分類され5年生存率は10%、平均余命は15ヵ月。分子生物学的特徴から2型に分類される。イソクエン酸脱水素酵素（IDH1: isocitrate dehydrogenase 1）遺伝子のコドン132のアルギニン（R）がヒスチジン（H）に点変異を有することにより、分化度の高いWHO grade II、IIIの星細胞腫から悪性転換（malignant transformation）した続発性膠芽腫（secondary GBM）と*IDH1*の変異を伴わない原発性膠芽腫（primary GBM）とに区別される。両者ともGBMとしての予後に差異はなく、半年から1年程度である（表）。

前者では、TP53 mutation（>65%）、ATRX mutation（>65%）に続いてLOH 19q（50%）、LOH 10q（>60%）、TERT mutation（30%）が引き起こされる。一方、後者の遺伝子異常とその頻度はTERT mutation（70%）、EGFR amplification（35%）、TP53 mutation（30%）、PTEN mutation（25%）、LOH 10p（50%）、LOH 10q（70%）である。

表　グリオーマ組織型と予後および遺伝子表現型

WHO grade	組織型	予後	遺伝子変化
Grade I	毛様細胞性星細胞腫	良 性	*BRAF*遺伝子の融合（*KIAA1549*）または点変異（V600E）を認める *IDH1*は野生型
Grade II	びまん性星細胞腫	中 間	*IDH1/IDH2*点変異　*ATRX*の変異、*TP53*点変異あり 脳幹、視床、脊髄に発症するものはDiffuse midline gliomaと定義され、H3 K27Mの変異を伴い悪性度はWHO grade IV
	希突起膠細胞腫	中 間	1p19q co-deletionかつ*IDH1*の変異型は予後良好
Grade III	退形成性星細胞腫	悪 性	*IDH*変異型で多くは*ATRX*、*TP53*変異型を伴う
	退形成性希突起膠細胞腫	悪 性	*IDH*変異型で1p19q co-deletionを伴い多くはG-CIMP+でMGMTプロモーターはメチル化されている症例の予後良好
Grade IV	神経膠芽腫	きわめて悪性	*IDH*野生型でG-CIMP-は予後不良

◲画像を拡大する

- Grade Iは、小児に多い分化型腫瘍で予後が良い（10年生存は80%以上）。
- Grade II、IIIは、1年から数年でGrade IVに悪性転換する。
  これとは別に、初発から神経膠芽腫として発症するタイプがある。
  いずれの神経膠芽腫も予後はきわめて悪い（5年生存率10%）。
- *BRAF*: B-Raf proto-oncogene、serine/threonine kinaseでRAS/RAF/MEK/MAPKシグナル伝達の主要な役割を担う。
- *TP53*: p53をコードする遺伝子
- G-CIMP: CpG island methylation phenotype DNA修復酵素MGMTのプロモーター領域のメチル化を示す表現型。
  この表現型ではMGMTの蛋白発現は抑制されるため、予後良好のマーカーとなる。
  GBM患者でCIMP+は若年者、腫瘍の遺伝子表現型がproneural typeに多く全生存期間の延長に寄与する。
- *ATRX*: alpha-thalassemia/mental retardation syndrome x-linked geneで、この遺伝子の変異は、テロメアの機能異常からテロメアの伸長（alternative lengthening of telomeres: ATL）を来す。

なお、遺伝子表現型とグリオーマ予後との関連は、次の文献を参考にした。
Siegal T. J Clin Neurosci. 2015;22:437-444.

欧州で施行された臨床試験においてテモゾロミド（TMZ[商品名:テモダール]）併用群（2年生存率26.5%、平均全生存期間14.6ヵ月）が、放射線治療（RT）単独治療群（2年生存率10.4%、平均全生存期間12.1ヵ月）に比して、有意差をもって生存期間の延長が認められ、TMZ + RTがGBMの標準治療とされている。

GBMは、このように予後不良で“がんの中のがん”といい得るため、創薬の対象となり、さまざまな臨床試験や新規治療薬が開発されている。GBMの根本治療の創出が今後の大きな課題である。

■ 疫学

国内における原発性脳腫瘍患者（年間2万人、人口10万人につき14人）のうち、GBMは2,220人で、悪性脳腫瘍の中で最も多く、11.1%を占める。

大脳半球白質に好発し（前頭葉35%、側頭葉25%、頭頂葉18%、後頭葉6%）、時に脳梁を介して対側半球へ浸潤する。平均発症年齢は60歳、45～75歳の中高年に多く、原発性膠芽腫が9割を占め、その平均発症年齢は62歳、続発性膠芽腫は平均45歳と若い。男性が女性の1.4倍多く、小児ではまれであり、成人と異なり脳幹部、視床、基底核部に好発する。

■ 病因

発生起源細胞の同定および腫瘍形成の分子機構は解明されていない。

BaileyとCushing（1926年）は、組織発生を念頭に起源細胞に基づいた組織分類を提唱し、脳腫瘍を16型に分類し、glioblastomaの起源細胞をbipolar spongioblast（双極性突起を持つ紡錘型細胞）とした。

WHO脳腫瘍分類に貢献した群馬大学の石田陽一は、膠芽腫を星細胞腫とともに星形グリアの腫瘍と定義した[1]。石田の正常な星形グリアとグリオーマの電顕像での詳細な観察によると、 血管壁まで伸び足板を壁におく太い細胞突起には、8～9nmの中間径フィラメントと少量の20～25nmの微小管とグリコーゲン顆粒を有する星形グリアとしての形質が、分化型の星細胞種でよく保たれており、膠芽腫でも保持されていることから、グリオーマを腫瘍性グリアと考察した。さらに星芽細胞腫（astroblastoma）は、腫瘍細胞が血管を取り囲んで放射冠状に配列されていることから、血管足が強調された腫瘍型とした。このように多くの病理学者が、星細胞腫をアストロサイトの脱分化した腫瘍と定義している。

発生学的には、げっ歯類の観察から、成体脳においても脳室周囲の脳室下帯（SVZ）や海馬歯状回（DG）において、neural stem cell/glial progenitorの活発な嗅球や顆粒細胞層へのmigrationが確認されていた。James E Goldmanらは、グリオーマ細胞の特性である高い遊走能は、neural stem cell/glial progenitorの特性を反映していると推察している[2]。Fred H Gageらは、ブロモデオキシウリジンをヒトに投与することで、高齢者においてもSVZとDGではDNA合成するNeuN陽性細胞を同定し、neural stem cell/neural progenitorの存在を確認したと報告した[3]。Sanai Nらは、ヒトSVZ生検材料を用いた培養系の研究から、脳室壁ependyma直下のastrocyteが、neural progenitorであると判定した[4]。状況証拠的には、 現時点で直接証明はなされていないがneural stem cell/glial progenitorが、グリオーマ細胞の起源細胞の有力な候補であると思われる。さらに原発性GBMと続発性GBMでは、前述したように遺伝子異常のパターンが異なるため、起源細胞が異なる可能性も示唆される[5、6]。

以上のほか、歴史的にグリオーマの病因としては、グリア（アストロサイト）の脱分化とする考えと、前駆細胞のmaturation arrestとする説がある。

近年、携帯電話の普及に伴い、公衆衛生学的観点からは、ラジオ波電磁界の発がん性の懸念が提起されている。山口によると[7]、携帯電話と神経膠腫に関する疫学調査では、デンマークの前向きコホート調査が実施されたが、10年以上の長期契約者でもリスクの上昇を認めなかった。スウェーデンにおける症例対照研究では、10年を超えて携帯電話端末を使用した群では、非使用群と比較して2.6倍のリスクが指摘された。日本も参加した国際共同研究「INTERPHONE研究」では、累積使用時間が1,640時間以上でオッズ比1.4倍と、有意な上昇を示した。

以上から、携帯電話は人にがんを生じさせる可能性があると判定されている。

■ 症状

腫瘍塊周囲に脳浮腫を伴いながら急速に浸潤性に増殖するため、早ければ週単位で、少なくとも月単位で症状が進行する。初発症状としては頭痛（31%）が最も多く、次いで痙攣（18%）、性格変化（16%）や運動麻痺（13%）などの巣症状が多い。

症状は、腫瘍の発生した場所の脳機能の障害を反映するのが基本である。また、病変が進行し、広範に浸潤すると症状は顕著となる。たとえば両側前頭葉に浸潤する症例では、性格変化、意欲低下、尿失禁、下肢の麻痺が出現する。一側では、初期には徴候は目立たず、徐々に腫瘍塊を形成し、脳浮腫が顕著になると具現化する。側頭葉腫瘍では、優位半球の病変では失名詞などの失語症状や4分の1半盲などが出現しやすい。また、視野症状に、患者自身が気付いていないことが多い。

前述したように、腫瘍局在に応じた神経学的局在症状の出現が基本であるが、たとえば前頭葉に局在する腫瘍でも神経回路網（frontal-parietal networks）を介して、頭頂葉の症候が認められることがあるので注意しなければならない。

具体例として、右側前頭葉病変ではいつも通りに職場へ通勤できなくなるなどの空間認知能の低下や、左側前頭葉腫瘍では失書・失算や左右失認など優位半球頭頂葉症状としてのゲルストマン症状が認められるなどの例が挙げられる。このような症例では、画像検査で大脳白質を介する脳浮腫が顕著である場合が多い。

小児や若年者では、ひとたび頭痛や吐気などの頭蓋内圧亢進症状が出現すると、急速に脳ヘルニアへと進行し、致命的な事態になるので、時期を逸せず迅速に対応することが重要となる。時として脳腫瘍患者は、内科・小児科、精神科において感冒、インフルエンザ、下痢・嘔吐症、認知症、精神疾患として誤診されている場合もある。たまたま下痢・嘔吐症が、流行する時期に一致すると、症状のみの診断では見逃される可能性が高くなりやすい。

そのため、器質的疾患が強く疑わしい症例に限定して画像検査（MRI）を施行するのではなく、症状が軽快せず、進行・悪化している場合には、致命的な見逃しをなくすため、また、器質的な疾患をスクリーニングするためにも、脳画像検査を診療の早期に取り入れる視点が大切であろう。これによりカタストロフィックな見逃しは回避でき、患者の生命および機能予後の改善につなげることができるからである。強く疑わしい症例でなくとも、鑑別診断をするために、脳神経外科を紹介しておく心がけも重要である。

■ 予後

標準治療、すなわち外科的な切除後にTMZを内服併用した放射線化学療法施行患者の全生存期間（OS）は、15ヵ月程度である。IDH1野生型で9.9ヵ月、IDH1変異型で24.0ヵ月である。ヒト化モノクロナール抗体のベバシズマブ（商品名: アバスチン）やインターフェロンの併用は、OSには寄与しない。組織学的にglioblastoma with oligodendroglioma component、giant cell GBM、 cystic GBMは悪性だが、古典的なGBMよりやや予後が良い傾向にある。分子基盤に基づいてMGMT非メチル化症例やIDH1野生型の予後不良例では、TMZに反応を示さない場合が多く、今後免疫療法や免疫チェックポイント阻害剤の応用が取り入れられるであろう。これらの治療には、腫瘍ペプチドワクチン療法WT1やさらに百日咳菌体をアジュバントしたWT1-W10、抗PD-1 (Programmed cell deah-1) 抗体療法などT細胞の免疫応答にかけられたブレーキを解除することでT細胞の活性化状態を維持し、がん細胞を細胞死に追いやる試みである。

同じくT細胞の表面に発現する抑制性因子CTLA (Cytotoxic T-lymphocyte-associated antigen 4) に対する抗体の併用も期待されている。

▲ページTOPへ

2 診断　（検査・鑑別診断も含む）

■ 検査

造影MRI、 脳血管撮影、 MRS、 PET（methionine、FDG）などの検査と合わせ、総合的に判断する。

■ 鑑別診断

造影MRIや造影CTでは、不規則なリング状の造影効果を示す。GBM、転移性脳腫瘍、脳膿瘍との鑑別が必要である。GBMでは、造影部分は壊死を取り囲む血管新生を反映するので、より不規則なリング状になる。それに比べ脳膿瘍のリングは、円形でよりスムースである。転移性脳腫瘍は、GBMと脳膿瘍の中間を取るので目安になるが、さらに拡散強調MRIやMRスペクトルスコピーなど多種類の検査で、総合的に判断することが重要である。

術中迅速診断では、壊死を取り囲む偽柵状配列が明らかでないとHGG（high grade glioma）と診断されるので、確定診断は永久標本によることになる。摘出腔内にカルムスチン（脳内留置用徐放性製剤: BCNUウェハー[商品名: ギリアデル]）の使用を予定するときは、時に悪性リンパ腫との鑑別が問題となる。

悪性リンパ腫では、血管中心性の腫瘍細胞の集簇に注目して診断するが、LCA、GFAP、MIB-1など免疫組織学的検査では、迅速標本の作成が必要となる症例もある。

転移性脳腫瘍との組織上の鑑別は容易であるが、きわめてまれにadenoid glioblastomaの症例で腺腔形成や扁平上皮性分化を示すので、注意が必要である。

▲ページTOPへ

3 治療　（治験中・研究中のものも含む）

■ 基本治療

腫瘍容量の減圧と確定診断を目的に、まず外科治療を行う。近年、ナビゲーションと術中MRIを用いた画像誘導による外科手術が、一般的となってきている。グリオーマの外科手術の目標は、機能を損なうことなく最大限の摘出をすることにある。

MRI Gd（Gadolinium）-DTPAにて造影された腫瘍塊が、全部摘出された症例の予後では期待でき、腫瘍摘出度が高いほど予後の改善に結び付くと、複数の報告がなされている。

次いで確定診断後には、TMZ併用の化学放射線療法が標準治療である。放射線療法は、拡大局所にtotal 60Gy（2Gy×30 fractions）を週5回、6週間かけて行うのが標準である。

最近は、周囲脳の保護を目的に強度変調放射線治療（Intensity Modulated Radiation Therapy: IMRT）を行うことが多い。

初期治療終了後には、TMZの内服を月5日間行う。再発時にはインターフェロンβの併用や、血管内皮増殖因子に対するベバシズマブの併用などが行われている。

■ その他の治療

手術前日にタラポルフィンナトリウム（商品名: レザフィリン）を投与し、病巣部位に集積させ、手術により最大限の摘出後にレーザー光を照射する摘出断端の浸潤部位に対する光線力学的療法やカルムスチンの摘出腔留置などがある。

▲ページTOPへ

4 今後の展望

陽子線、炭素線やホウ素中性子補足療法などの、新しい線源を用いた悪性脳腫瘍への応用やウイルス療法、脳内標的部位への薬剤分布を高める技術として開発されたconvection-enhanced delivery（CED）、免疫療法などがある。

免疫療法には、がん免疫に抑制性に働くものに対する解除を目的とする、T細胞活性化抑制抗原に対する抗PD-1抗体による治療やがん遺伝子WT1（Wilms tumor 1）を抗原標的として、自己のTリンパ球にがん細胞を攻撃させるWT1ペプチドワクチン療法がある。後者は、脳腫瘍の最新治療法として安全性や有効性が確立されつつあり、ランダム化比較試験の結果が期待される。

▲ページTOPへ

5 主たる診療科

- 脳神経外科

※ 医療機関によって診療科目の区分は異なることがあります。

ページTOPへ

6 参考になるサイト（公的助成情報、患者会情報など）

- 診療、研究に関する情報

国立がん研究センター　がん対策情報センター がん情報サービス
（一般利用者向けと医療従事者向けのまとまった情報）

一般社団法人 日本脳神経外科学会、日本脳神経外科コングレス　脳神経外科疾患情報ページ
（一般利用者向けと医療従事者向けのまとまった情報）

ページTOPへ

参考文献

1) 石田陽一. 北関東医. 1990;40:355-361.
2) Cayre M, et al. Prog Neurobiol. 2009;88:41-63.
3) Eriksson PS,et al. Nat Med. 1998;4:1313-1317.
4) Sanai N, et al. Nature. 2004;427:740-744.
5) Louis DN, et al. WHO Classification of Tumours of the Central Nervous System. Revised 4th Edition.Lyon;IARC Press:2016.pp52-56.
6) Louis DN, et al. Acta Neuropathol. 2016;131:803-820.
7) Yamaguchi N. Clin Neurosci. 2013;31:1145-1146.

公開履歴

初回　2015年02月27日
更新　2017年03月21日

脳神経外科関連の希少疾病ライブラリ

- 脊髄空洞症
- 膠芽腫
- 常染色体優性多発性嚢胞腎
- もやもや病

インデックスページへ戻る

Journal of Pharmacological Sciences 127 (2015) 217–222

HOSTED BY

Contents lists available at ScienceDirect

Journal of Pharmacological Sciences

journal homepage: www.elsevier.com/locate/jphs

Full paper

Effect of caffeine contained in a cup of coffee on microvascular function in healthy subjects

Katsuhiko Noguchi [a, *], Toshihiro Matsuzaki [a], Mayuko Sakanashi [a], Naobumi Hamadate [a], Taro Uchida [a], Mika Kina-Tanada [a], Haruaki Kubota [a], Junko Nakasone [a], Matao Sakanashi [a], Shinichiro Ueda [b], Hiroaki Masuzaki [c], Shogo Ishiuchi [d], Yusuke Ohya [e], Masato Tsutsui [a, *]

[a] Department of Pharmacology, Graduate School of Medicine, University of the Ryukyus, Okinawa, Japan
[b] Department of Clinical Pharmacology and Therapeutics, Graduate School of Medicine, University of the Ryukyus, Okinawa, Japan
[c] Second Department of Internal Medicine, Graduate School of Medicine, University of the Ryukyus, Okinawa, Japan
[d] Department of Neurosurgery, Graduate School of Medicine, University of the Ryukyus, Okinawa, Japan
[e] Third Department of Internal Medicine, Graduate School of Medicine, University of the Ryukyus, Okinawa, Japan

ARTICLE INFO

Article history:
Received 16 October 2014
Received in revised form
26 December 2014
Accepted 13 January 2015
Available online 28 January 2015

Keywords:
Caffeine
Coffee
Endothelial function
Laser-Doppler flowmetry
Microcirculation

ABSTRACT

Recent epidemiological studies have demonstrated that coffee drinking is associated with reduced mortality of cardiovascular disease. However, its precise mechanisms remain to be clarified. In this study, we examined whether single ingestion of caffeine contained in a cup of coffee improves microvascular function in healthy subjects.

A double-blind, placebo-controlled, crossover study was performed in 27 healthy volunteers. A cup of either caffeinated or decaffeinated coffee was drunk by the subjects, and reactive hyperemia of finger blood flow was assessed by laser Doppler flowmetry. In an interval of more than 2 days, the same experimental protocol was repeated with another coffee in a crossover manner. Caffeinated coffee intake slightly but significantly elevated blood pressure and decreased finger blood flow as compared with decaffeinated coffee intake. There was no significant difference in heart rate between caffeinated and decaffeinated coffee intake. Importantly, caffeinated coffee intake significantly enhanced post-occlusive reactive hyperemia of finger blood flow, an index of microvascular endothelial function, compared with decaffeinated coffee intake.

These results provide the first evidence that caffeine contained in a cup of coffee enhances microvascular function in healthy individuals.

1. Introduction

Coffee is the most widely consumed beverage in the world (1). Coffee contains a variety of pharmacologically active ingredients, and it has long been argued whether coffee drinking is beneficial or harmful for cardiovascular disease (2–4). Recently, a large cohort study, in which more than 400,000 participants were prospectively followed up for 13 years, has demonstrated that coffee consumption is associated with reduced mortality of cardiovascular disease (5). Moreover, a meta-analysis of 23 prospective studies has provided quantitative evidence that coffee intake is inversely related to cardiovascular disease mortality (6). These findings suggest the beneficial cardiovascular actions of coffee. However, its precise mechanisms remain to be elucidated.

The vascular endothelium synthesizes and releases several vasodilating substances, such as prostacyclin, nitric oxide, and endothelium-derived hyperpolarizing factors (EDHF). Evaluation of endothelial function has been shown to provide important prognostic information in patients with cardiovascular disease, as evidenced by the facts that the severity of endothelial dysfunction can predict future cardiovascular events (7, 8) and that improvement of endothelial function by pharmacological interventions reduces the risk of cardiovascular disease. Acute effects of caffeine, a major

* Corresponding authors. Department of Pharmacology, Graduate School of Medicine, University of the Ryukyus, 207 Uehara, Nishihara-cho, Okinawa 903-0215, Japan. Tel.: +81 98 895 1133; fax: +81 98 895 1411.
E-mail addresses: noguchi@med.u-ryukyu.ac.jp (K. Noguchi), tsutsui@med.u-ryukyu.ac.jp (M. Tsutsui).
Peer review under responsibility of Japanese Pharmacological Society.

http://dx.doi.org/10.1016/j.jphs.2015.01.003
1347-8613/

pharmacologically active ingredient of coffee, on human endothelial function of large conduit arteries have been examined in several previous studies by using ultrasound-based measurement of brachial artery diameter during post-occlusive reactive hyperemia. However, the results of those studies are quite inconsistent (9–13). It is generally accepted that flow-dependent dilation of conduit arteries is mediated primarily by nitric oxide (14), while in the microcirculation EDHF rather than nitric oxide have been suggested to play a major role in the reactive hyperemic response (15). Microvessels, but not large arteries, regulate tissue blood blow and systemic blood pressure, and thereby play a key role in the circulatory system. However, no study has ever addressed the effect of caffeine on microvascular function.

Based on the above background, we examined in this study the effect of single ingestion of a cup of caffeinated and decaffeinated coffee on finger microvascular function in healthy subjects by laser Doppler flowmetry.

2. Methods

2.1. Subjects

We recruited twenty-seven healthy subjects (13 men and 14 women; 22–30 years old [mean age, 23.7 ± 2.2]; mean body weight, 58.4 ± 15.1 kg; mean height, 162.9 ± 9.6 cm) in our university, and the subjects who wanted to take part in the study voluntarily were investigated. Subjects taking any medication or smokers were excluded from the study, and the experiments were performed when the subjects were well conditioned. All volunteers were asked to abstain from caffeine-contained beverages at least 12 h before the study. All subjects gave written informed consent, and invasive experiments including blood sampling were approved by the Clinical Trial Ethics Committee of the University of the Ryukyus, according to the declaration of Helsinki and the ethical standard.

2.2. Study design

A double-blind, placebo-controlled, crossover study was performed. All participants were examined on two separate days in a quiet temperature-controlled room. Instant coffee of 2 g with or without caffeine (Taster's Choice™, Nestlé, Vevey, Switzerland) was prepared with 150 ml hot water. Neither sugar nor milk was added. A cup of the caffeinated or decaffeinated coffee was ingested in each subject. Hemodynamic variables and reactive hyperemic response were measured before and every 15 min after coffee intake. In a pilot study, we were not able to continue this experiment more than 75 min because some subjects complained of strong pain due to repeated cuff-compression or a fixed position of the test arm. Thus, we set the experiment time for 75 min. In an interval of more than 2 days, the same experimental protocol was repeated with another coffee in a crossover manner. Blood pressures were measured at the brachial artery using a sphygmomanometer (BP-103i, Nihon Colin, Komaki, Japan). A manchette was placed around the right upper arm, and a mean value of three measurements was used for the statistical analyses. Heart rate was obtained from the sphygmomanometer. The subjects were in a sitting position throughout the experiments.

2.3. Assessment of microvascular function

Finger blood flow was measured by a laser Doppler flowmeter (ALF21, Advance, Tokyo, Japan). A flow-probe (type C) was placed at the tip of the left index finger or thumb. Blood flow was calculated by measuring Doppler shifts derived from moving erythrocytes per photon and the mean photon frequency. As the number of Doppler shifts is proportional to the erythrocyte volume and velocity, blood flow is the product of linearized volume and velocity (16). Post-occlusive reactive hyperemia of finger blood flow was assessed as an index of microvascular endothelial function. A cuff was placed on the left upper arm, and reactive hyperemia of finger blood flow was induced by inflating a cuff for 1 min in order to interrupt arterial blood flow and then deflating it. Peak hyperemic flow was defined as the highest blood flow immediately after cuff deflation. Reactive hyperemia was calculated according to the following equation:

Reactive hyperemia (%) = [(peak hyperemic flow − resting flow)/resting flow] × 100

2.4. Measurement of caffeine and catecholamine levels

Venous blood samples were collected before and 30 min after coffee ingestion in five volunteers. The plasma caffeine levels and caffeine contents in decaffeinated and caffeinated coffee were analyzed by high performance liquid chromatography (HPLC; LC-10AD, Shimadzu, Kyoto, Japan) (17). Plasma catecholamine levels were measured by SRL Inc. (Tokyo, Japan) using the HPLC method.

2.5. Statistical analysis

Statistical analyses were performed by a two-way ANOVA followed by a Bonferoni/Dunn post hoc test. When paired or unpaired data were compared, a paired or unpaired Student's *t*-test, respectively, was applied. The computer software StatView-J 5.0 (SAS Institute Japan Ltd, Tokyo, Japan) was used for the statistical analyses. A value of $P < 0.05$ was considered to be statistically significant. Results are expressed as mean ± SD.

Reproducibility of laser Doppler flowmetry was expressed as within-subject coefficients of variability. In our laboratory, the intra-day variability for finger blood flow was 6.3% (range: 0–27.1%) and that for reactive hyperemia assessed by laser Doppler flowmetry was 21.6% (0–54.2%), and the day-to-day variability for finger blood flow was 26.2% (0–76.1%) and that for reactive hyperemia was 33.7% (0–102%). According to the previous studies, the coefficient of variance < 35% can be deemed acceptable (18).

3. Results

3.1. Caffeine content in decaffeinated and caffeinated coffee and plasma caffeine levels before and after coffee intake

Caffeine content in decaffeinated vs. caffeinated coffee was markedly different (1.37 ± 0.09 vs. 54.5 ± 3.4 mg, respectively) (Fig. 1A). Before coffee intake, plasma caffeine levels were identical between subjects with decaffeinated and caffeinated coffee intake. However, 30 min after coffee intake, plasma caffeine levels were markedly increased in the subjects with caffeinated coffee intake (from 0.75 ± 0.85 to 1.57 ± 1.30 μg/ml, $P < 0.05$), but not in those with decaffeinated coffee intake (from 0.76 ± 0.57 to 0.77 ± 0.60 μg/ml) (Fig. 1B).

3.2. Effects of caffeinated coffee intake on blood pressure and finger blood flow

Before coffee intake, there were no significant differences in baseline hemodynamic variables (i.e., systolic, diastolic, and mean blood pressures, finger blood flow, vascular resistance, or heart rate) in the subjects with decaffeinated and caffeinated coffee intake (Table 1). However, caffeinated coffee intake, but not

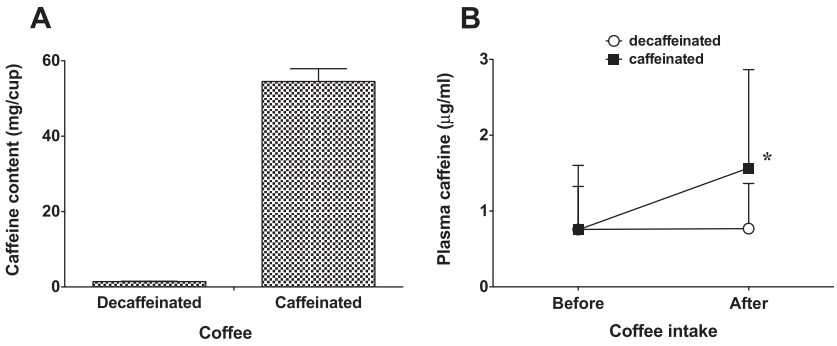

Fig. 1. Caffeine contents in a cup of decaffeinated and caffeinated coffee (A) and plasma caffeine levels before and 30 min after single intake of caffeinated and decaffeinated coffee (B). Data are expressed as mean ± SD. *$P < 0.05$ between before and after coffee intake by a paired *t*-test.

decaffeinated coffee intake, caused slight but significant elevations of systolic, diastolic and mean blood pressures by maximally 2.7, 3.2 and 2.8 mmHg, respectively (each $P < 0.01$, Fig. 2). Furthermore, caffeinated coffee intake significantly reduced finger blood flow (as assessed by laser-Doppler flowmetry, $P < 0.01$, Fig. 3A) and significantly increased vascular resistance of the finger vascular bed when compared with decaffeinated coffee intake ($P < 0.01$, Fig. 3B). On the other hand, there was no significant difference in heart rate in the subjects with decaffeinated and caffeinate coffee intake (Fig. 3C).

3.3. Effects of caffeinated coffee intake on reactive hyperemia of finger blood flow

Before coffee intake, post-occlusive reactive hyperemia of finger blood flow, an index of microvascular endothelial function, were comparable between the subjects with decaffeinated and caffeinated coffee (8.7 ± 4.3 and 10.0 ± 3.4 ml/min/100 g, respectively). However, caffeinated coffee intake significantly enhanced post-occlusive reactive hyperemia of finger blood as compared with decaffeinated coffee intake ($P < 0.01$, Fig. 4).

3.4. Plasma catecholamine levels

Plasma norepinephrine levels did not significantly differ between the subjects with decaffeinated and caffeinated coffee intake at baseline (336 ± 132 vs. 317 ± 165 pg/ml) and at 30 min after the intake (271 ± 95 vs. 272 ± 125 pg/ml). Plasma epinephrine levels also did not significantly alter between the subjects with decaffeinated and caffeinated coffee intake at baseline (35.8 ± 12.5 vs. 33.3 ± 18.5 pg/ml) and at 30 min after the intake (32.0 ± 11.2 vs. 25.8 ± 13.5 pg/ml). The respective plasma catecholamine levels did not significantly change before and after coffee intake.

Table 1
Baseline characteristics in subjects with decaffeinated and caffeinated coffee intake.

Variables	Decaffeinated	Caffeinated	*P* value
Systolic BP (mmHg)	104.9 ± 12.4	106.2 ± 11.2	0.346
Diastolic BP (mmHg)	58.0 ± 8.3	59.1 ± 6.6	0.297
Mean BP (mmHg)	73.6 ± 8.8	74.8 ± 7.6	0.264
Finger blood flow (ml/min/100 g)	23.6 ± 7.7	23.3 ± 7.9	0.916
Vascular resistance (unit)	3.43 ± 1.15	3.67 ± 1.63	0.543
Reactive hyperemia (%)	40.8 ± 25.4	50.3 ± 27.1	0.125
Heart rate (bpm)	74.6 ± 9.4	74.3 ± 8.6	0.815

BP = blood pressure, Vascular resistance = vascular resistance of the finger vascular bed (finger blood flow/mean BP), Reactive hyperemia (%) = 100 × (post-occlusive increase in finger blood flow)/(baseline finger blood flow).

4. Discussion

To the best of our knowledge, this is the first study examining the acute effect of caffeine on endothelial function in the human finger cutaneous microcirculation. The present study demonstrates that an intake of caffeine contained in a cup of coffee may cause a favorable effect on microvascular endothelial function assessed by a noninvasive laser Doppler flowmetry method in Japanese young healthy subjects.

4.1. Pressor effect of caffeine

In the present study, the plasma caffeine concentration after caffeinated coffee intake attained 1.6 μg/ml. This concentration of caffeine has been shown to act as an antagonist of adenosine A_1/A_{2A} receptors (19, 20). As adenosine causes vasodilation in most vascular beds (21), caffeine would induce an increase in vascular resistance. Thus, slight but significant rises in blood pressure observed after caffeinated coffee intake in the present study may, in part, be caused by an increase in basal vascular tone derived from the adenosine antagonism of caffeine, as found by an early study (22). In addition, a direct stimulatory effect of caffeine on myocardial contractility (23) might be involved in a significant increase in blood pressure seen after caffeinated coffee intake.

4.2. Effect of caffeine on microvascular function

The present finding that caffeine ingestion, even at a small dose (54.5 mg = less than 1 mg/kg), improves microvascular endothelial function is consistent with a previous study (24) using venous occlusion plethysmography demonstrating that the acute administration of caffeine at an extremely large dose (300 mg) augments vasodilator responses of forearm vessels to intra-arterial infusion of the endothelium-dependent agonist acetylcholine.

In contrast to our study, however, two previous reports using ultrasound-based measurement of brachial artery diameter during post-occlusive reactive hyperemia demonstrated that caffeinated coffee ingestion impaired endothelial function in healthy volunteers (9, 12). In addition, two other studies showed that acutely administered caffeine had no effect on endothelial function assessed by the brachial artery vasoreactivity measurement (10, 11). Although the reason for conflicting with our data cannot be fully explained at present, it seems plausible that the difference in the type of vessels used for assessing vascular function was mainly involved. Laser Doppler flowmetry employed in the present study measures microvascular function in cutaneous arterioles and capillaries, whereas the ultrasound-based measurement of brachial artery diameter reflects 'macrovascular' function in large conduit

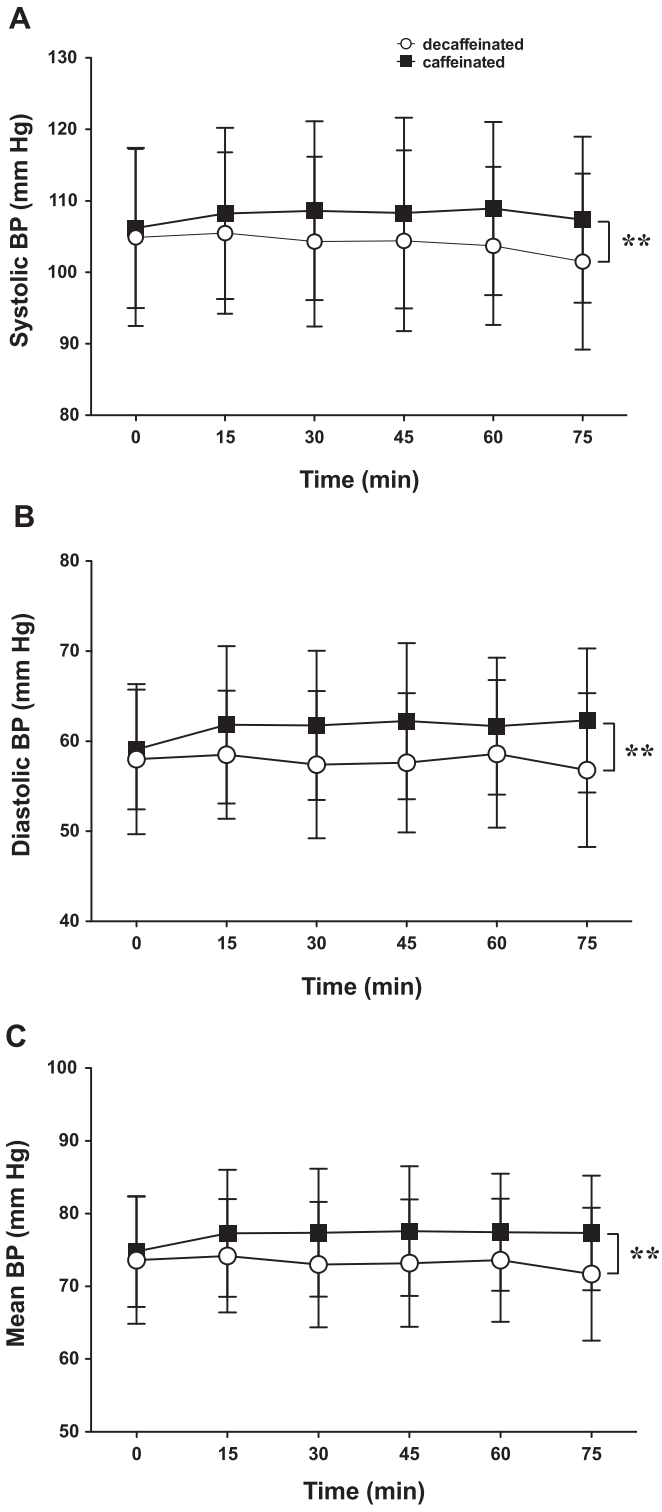

Fig. 2. Effects of caffeinated and decaffeinated coffee intake on systolic (A), diastolic (B) and mean (C) blood pressures (BP). Data are expressed as mean ± SD. $^{**}P < 0.01$ between caffeine (−) and caffeine (+) by ANOVA.

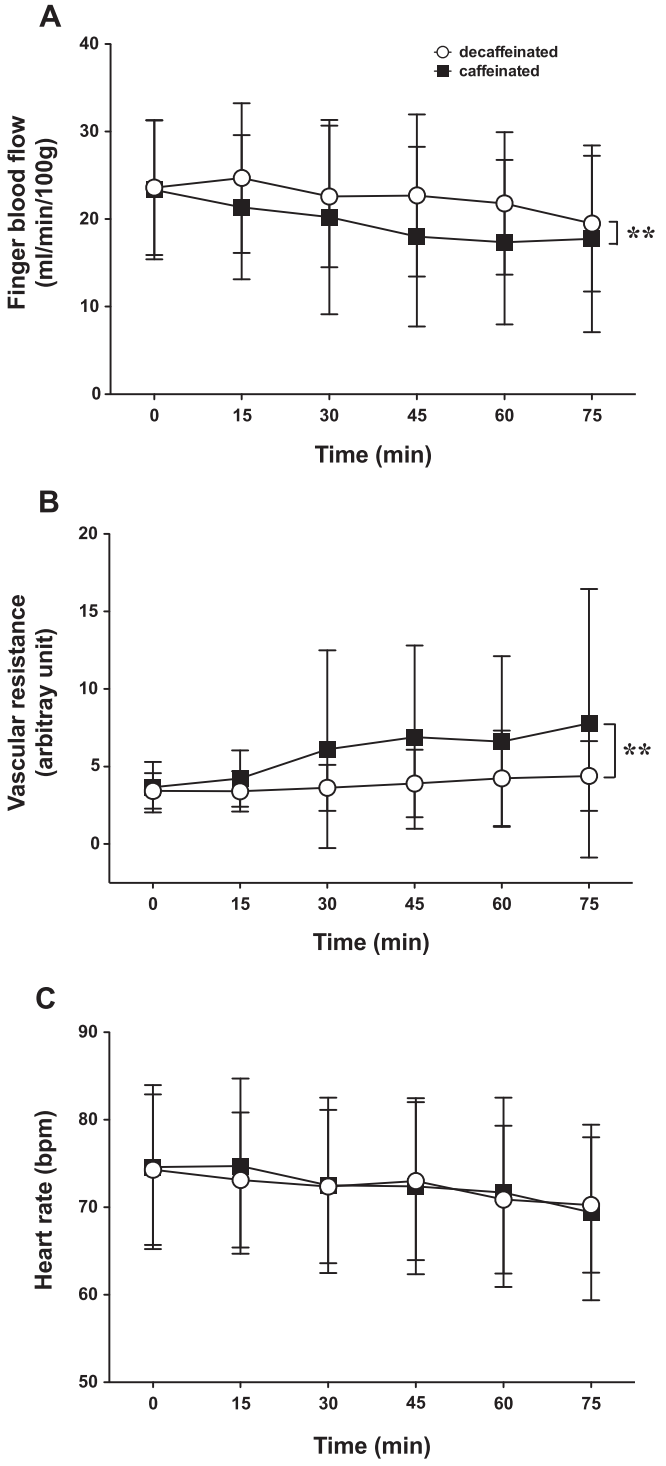

Fig. 3. Effects of caffeinated and decaffeinated coffee intake on finger blood flow (A), vascular resistance of the finger vascular bed (B), and heart rate (C). Data are expressed as mean ± SD. $^{**}P < 0.01$ between caffeine (−) and caffeine (+) by ANOVA.

arteries. Indeed, some previous studies have described that brachial artery responses to reactive hyperemia do not correlate with microvascular function as measured by agonist infusion studies or laser Doppler flowmetry (25, 26). It is generally considered that flow-dependent dilation of conduit arteries is mediated primarily by nitric oxide (14). By contrast, contribution of nitric oxide to post-occlusive reactive hyperemia in microvessels appears minimal (27, 28). Instead, EDHF may have a major role in the reactive hyperemic response in the microcirculation (15). Although the nature and mechanisms of EDHF remain uncertain, EDHF response has been proposed to be divided into two broad categories as follows: the first (classical) EDHF pathway is associated with endothelial cell hyperpolarization due to the opening of endothelial calcium-

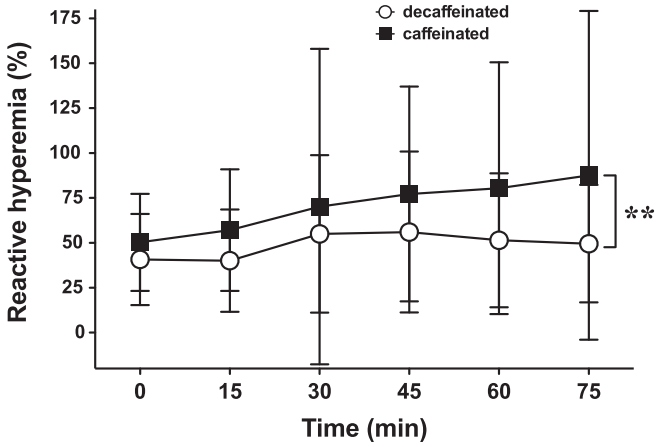

Fig. 4. Effect of caffeinated and decaffeinated coffee intake on post-occlusive reactive hyperemia of finger blood flow. Reactive hyperemia was calculated according to the following equation: reactive hyperemia (%) = [(peak hyperemic flow − resting flow)/resting flow] × 100. Data are expressed as mean ± SD. $^{**}P < 0.01$ between caffeine (−) and caffeine (+) by ANOVA.

activated K^+-channels, and the second EDHF pathway does not require endothelial hyperpolarization but involves the endothelial release of factors that hyperpolarize vascular smooth muscle cells by opening various myocyte K^+-channels such as calcium-activated K^+-channels (29). Experimental studies with animal and human vessels have demonstrated that the activation of vascular smooth muscle Ca^{2+}-activated K^+ channels probably contributes to the EDHF component of reactive hyperemia in microvessels (30, 31). Thus, microvascular endothelial function assessed by laser Doppler flowmetry may reflect the bioavailability of endothelium-dependent hyperpolarization via the activation of Ca^{2+}-activated K^+ channels in the endothelium and/or vascular smooth muscles.

4.3. Possible mechanisms involved in the beneficial effect of caffeine on microvascular function

In addition to the action on adenosine receptors, caffeine has been known to have a variety of pharmacological properties, including inhibition of phosphodiesterase (32), and calcium release from intracellular calcium stores via ryanodine-sensitive calcium channels (33). Interestingly, several electrophysiological experiments have displayed that caffeine at concentrations ranging from 10^{-6} to 10^{-3} M evokes calcium-dependent hyperpolarization in endothelial cells and vascular smooth muscle cells as a result of increased outward K^+ current (34–36). These data suggest that caffeine-induced release of calcium from intracellular calcium stores elicits the activation of calcium-activated K^+-channels in these cells. Considering that EDHF, unlike nitric oxide, has a major role in microvascular reactive hyperemia, it is possible that caffeine has the potential to augment the reactive hyperemic response of microvessels through amplifying hyperpolarization caused by EDHF. This may explain a favorable effect of caffeine on microvascular endothelial function in the present study, because the plasma concentration of caffeine was estimated to be nearly 10^{-5} M (Fig. 1B). It is intriguing that previous experiments in rats have shown that treatment with blockers of calcium-activated K^+-channels dose not affect baseline blood pressure or vascular conductance but attenuates vasodilator responses of resistance vessels produced by endothelium-dependent vasodilators such as acetylcholine (37, 38). These findings indicate that calcium-activated K^+-channels contribute little to the regulation of basal blood pressure but participate in responses to endothelial stimulation, and may be related to the present results that caffeine intake produced enhancement of microvascular endothelial function in spite of the occurrence of a slight increase in baseline blood pressure.

Several clinical studies (13, 39–41) have shown that caffeine exerts acute beneficial metabolic effects such as increased concentrations of adiponectin, a marker of anti-inflammatory and insulin-sensitizing effects (42). In addition, a cross-sectional study has reported that coffee consumption is inversely associated with a plasma marker of inflammation (C-reactive protein) and that of endothelial dysfunction (E-selectin) (43). Thus, these preferable properties of caffeine, besides the effect on endothelial function, may partly account for the beneficial cardiovascular effect of long-term coffee consumption.

4.4. Study limitations

Our study has some potential limitations to be considered. First, the number of subjects examined in this study may have been so small as to provide conclusive proof, although statistically significant effects were found. Second, the long-term effects of caffeine ingestion on endothelial function remain unknown. Third, we did not ask female subjects about the menstrual cycle, and it is thus unknown to what extent its phases affected the finger blood flow response. Finally, assessment of microvascular function was performed solely in Japanese healthy young volunteers. We have not yet elucidated whether or not caffeinated coffee intake ameliorates microvascular endothelial function not only in healthy subjects but also in patients with cardiovascular disease. These issues remain to be examined in future studies.

5. Conclusion

Our double-blind, placebo-controlled, crossover study has demonstrated, for the first time, that caffeine at the amount contained in a cup of coffee may cause improvement of microvascular endothelial function in healthy subjects.

Conflict of interest

None.

Acknowledgments

This work was supported in part by the All Japan Coffee Association and the Special Account Budget for Education and Research grated by the Japan Ministry of Education.

References

(1) Bonita JS, Mandarano M, Shuta D, Vinson J. Coffee and cardiovascular disease: in vitro, cellular, animal, and human studies. Pharmacol Res. 2007;55:187–198.
(2) Cornelis MC, El-Sohemy A. Coffee, caffeine, and coronary heart disease. Curr Opin Lipidol. 2007;18:13–19.
(3) Riksen NP, Rongen GA, Smits P. Acute and long-term cardiovascular effects of coffee: implications for coronary heart disease. Pharmacol Ther. 2009;121:185–191.
(4) Di Castelnuovo A, di Giuseppe R, Iacoviello L, de Gaetano G. Consumption of cocoa, tea and coffee and risk of cardiovascular disease. Eur J Intern Med. 2012;23:15–25.
(5) Freedman ND, Park Y, Abnet CC, Hollenbeck AR, Sinha R. Association of coffee drinking with total and cause-specific mortality. N Engl J Med. 2012;366:1891–1904.
(6) Malerba S, Turati F, Galeone C, Pelucchi C, Verga F, La Vecchia C, et al. A meta-analysis of prospective studies of coffee consumption and mortality for all causes, cancers and cardiovascular diseases. Eur J Epidemiol. 2013;28:527–539.

(7) Perticone F, Ceravolo R, Pujia A, Ventura G, Iacopino S, Scozzafava A, et al. Prognostic significance of endothelial dysfunction in hypertensive patients. Circulation. 2001;104:191–196.
(8) Widlansky ME, Gokce N, Keaney Jr JF, Vita JA. The clinical implications of endothelial dysfunction. J Am Coll Cardiol. 2003;42:1149–1160.
(9) Papamichael CM, Aznaouridis KA, Karatzis EN, Karatzi KN, Stamatelopoulos KS, Vamvakou G, et al. Effect of coffee on endothelial function in healthy subjects: the role of caffeine. Clin Sci (Lond). 2005;109:55–60.
(10) Duffy SJ, Keaney Jr JF, Holbrook M, Gokce N, Swerdloff PL, Frei B, et al. Short- and long-term black tea consumption reverses endothelial dysfunction in patients with coronary artery disease. Circulation. 2001;104:151–156.
(11) Alexopoulos N, Vlachopoulos C, Aznaouridis K, Baou K, Vasiliadou C, Pietri P, et al. The acute effect of green tea consumption on endothelial function in healthy individuals. Eur J Cardiovasc Prev Rehabil. 2008;15:300–305.
(12) Buscemi S, Verga S, Batsis JA, Donatelli M, Tranchina MR, Belmonte S, et al. Acute effects of coffee on endothelial function in healthy subjects. Eur J Clin Nutr. 2010;64:483–489.
(13) Shechter M, Shalmon G, Scheinowitz M, Koren-Morag N, Feinberg MS, Harats D, et al. Impact of acute caffeine ingestion on endothelial function in subjects with and without coronary artery disease. Am J Cardiol. 2011;107:1255–1261.
(14) Joannides R, Haefeli WE, Linder L, Richard V, Bakkali EH, Thuillez C, et al. Nitric oxide is responsible for flow-dependent dilatation of human peripheral conduit arteries in vivo. Circulation. 1995;91:1314–1319.
(15) Lorenzo S, Minson CT. Human cutaneous reactive hyperaemia: role of BK_{Ca} channels and sensory nerves. J Physiol. 2007;585:295–303.
(16) Bonner R, Nossal R. Model for laser Doppler measurements of blood flow in tissue. Appl Opt. 1981;20:2097–2107.
(17) Schreiber-Deturmeny E, Bruguerolle B. Simultaneous high-performance liquid chromatographic determination of caffeine and theophylline for routine drug monitoring in human plasma. J Chromatogr B, Biomed Appl. 1996;677:305–312.
(18) Roustit M, Blaise S, Millet C, Cracowski JL. Reproducibility and methodological issues of skin post-occlusive and thermal hyperemia assessed by single-point laser Doppler flowmetry. Microvasc Res. 2010;79:102–108.
(19) Snyder SH, Katims JJ, Annau Z, Bruns RF, Daly JW. Adenosine receptors and behavioral actions of methylxanthines. Proc Natl Acad Sci U S A. 1981;78:3260–3264.
(20) Fredholm BB, Battig K, Holmen J, Nehlig A, Zvartau EE. Actions of caffeine in the brain with special reference to factors that contribute to its widespread use. Pharmacol Rev. 1999;51:83–133.
(21) Rongen GA, Floras JS, Lenders JW, Thien T, Smits P. Cardiovascular pharmacology of purines. Clin Sci (Lond). 1997;92:13–24.
(22) Smits P, Boekema P, De Abreu R, Thien T, van 't Laar A. Evidence for an antagonism between caffeine and adenosine in the human cardiovascular system. J Cardiovasc Pharmacol. 1987;10:136–143.
(23) Riksen NP, Smits P, Rongen GA. The cardiovascular effects of methylxanthines. Handb Exp Pharmacol. 2011;200:413–437.
(24) Umemura T, Ueda K, Nishioka K, Hidaka T, Takemoto H, Nakamura S, et al. Effects of acute administration of caffeine on vascular function. Am J Cardiol. 2006;98:1538–1541.
(25) Shamim-Uzzaman QA, Pfenninger D, Kehrer C, Chakrabarti A, Kacirotti N, Rubenfire M, et al. Altered cutaneous microvascular responses to reactive hyperaemia in coronary artery disease: a comparative study with conduit vessel responses. Clin Sci (Lond). 2002;103:267–273.
(26) Eskurza I, Seals DR, DeSouza CA, Tanaka H. Pharmacologic versus flow-mediated assessments of peripheral vascular endothelial vasodilatory function in humans. Am J Cardiol. 2001;88:1067–1069.
(27) Wong BJ, Wilkins BW, Holowatz LA, Minson CT. Nitric oxide synthase inhibition does not alter the reactive hyperemic response in the cutaneous circulation. J Appl Physiol. 2003;95:504–510.
(28) Zhao JL, Pergola PE, Roman LJ, Kellogg Jr DL. Bioactive nitric oxide concentration does not increase during reactive hyperemia in human skin. J Appl Physiol. 2004;96:628–632.
(29) Edwards G, Feletou M, Weston AH. Endothelium-derived hyperpolarising factors and associated pathways: a synopsis. Pflugers Arch. 2010;459:863–879.
(30) Huang A, Sun D, Jacobson A, Carroll MA, Falck JR, Kaley G. Epoxyeicosatrienoic acids are released to mediate shear stress-dependent hyperpolarization of arteriolar smooth muscle. Circ Res. 2005;96:376–383.
(31) Liu Y, Bubolz AH, Mendoza S, Zhang DX, Gutterman DD. H_2O_2 is the transferrable factor mediating flow-induced dilation in human coronary arterioles. Circ Res. 2011;108:566–573.
(32) Butcher RW, Sutherland EW. Adenosine 3′,5′-phosphate in biological materials. I. Purification and properties of cyclic 3′,5′-nucleotide phosphodiesterase and use of this enzyme to characterize adenosine 3′,5′-phosphate in human urine. J Biol Chem. 1962;237:1244–1250.
(33) Endo M. Calcium release from the sarcoplasmic reticulum. Physiol Rev. 1977;57:71–108.
(34) Fujii K, Miyahara H, Suzuki H. Comparison of the effects of caffeine and procaine on noradrenergic transmission in the guinea-pig mesenteric artery. Br J Pharmacol. 1985;84:675–684.
(35) Chen GF, Suzuki H. Calcium dependency of the endothelium-dependent hyperpolarization in smooth muscle cells of the rabbit carotid artery. J Physiol. 1990;421:521–534.
(36) Rusko J, Van Slooten G, Adams DJ. Caffeine-evoked, calcium-sensitive membrane currents in rabbit aortic endothelial cells. Br J Pharmacol. 1995;115:133–141.
(37) Shinde UA, Desai KM, Yu C, Gopalakrishnan V. Nitric oxide synthase inhibition exaggerates the hypotensive response to ghrelin: role of calcium-activated potassium channels. J Hypertens. 2005;23:779–784.
(38) Parkington HC, Chow JA, Evans RG, Coleman HA, Tare M. Role for endothelium-derived hyperpolarizing factor in vascular tone in rat mesenteric and hindlimb circulations *in vivo*. J Physiol. 2002;542:929–937.
(39) Kempf K, Herder C, Erlund I, Kolb H, Martin S, Carstensen M, et al. Effects of coffee consumption on subclinical inflammation and other risk factors for type 2 diabetes: a clinical trial. Am J Clin Nutr. 2010;91:950–957.
(40) Wedick NM, Brennan AM, Sun Q, Hu FB, Mantzoros CS, van Dam RM. Effects of caffeinated and decaffeinated coffee on biological risk factors for type 2 diabetes: a randomized controlled trial. Nutr J. 2011;10:93–101.
(41) Yamashita K, Yatsuya H, Muramatsu T, Toyoshima H, Murohara T, Tamakoshi K. Association of coffee consumption with serum adiponectin, leptin, inflammation and metabolic markers in Japanese workers: a cross-sectional study. Nutr Diabetes. 2012;2:e33–e38.
(42) Li S, Shin HJ, Ding EL, van Dam RM. Adiponectin levels and risk of type 2 diabetes: a systematic review and meta-analysis. JAMA. 2009;302:179–188.
(43) Lopez-Garcia E, van Dam RM, Qi L, Hu FB. Coffee consumption and markers of inflammation and endothelial dysfunction in healthy and diabetic women. Am J Clin Nutr. 2006;84:888–893.

Surgical Neurology International

SNI: Stereotactic, a supplement to Surgical Neurology International

OPEN ACCESS

For entire Editorial Board visit : http://www.surgicalneurologyint.com

Editor
Antonio A. F. DeSalles, MD
University of California, Los Angeles, CA, USA

Progression of cerebellar chronic encapsulated expanding hematoma during late pregnancy after gamma knife radiosurgery for arteriovenous malformation

Takashi Watanabe, Hideki Nagamine, Shogo Ishiuchi

Department of Neurosurgery, Faculty of Clinical Medicine, University of the Ryukyus, Okinawa, Japan

E-mail: *Takashi Watanabe - wtakashi@med.u-ryukyu.ac.jp; Hideki Nagamine - h082632@med.u-ryukyu.ac.jp; Shogo Ishiuchi - ishogo@med.u-ryukyu.ac.jp
*Corresponding author

Received: 30 April 14 Accepted: 04 August 14 Published: 30 December 14

This article may be cited as:
Watanabe T, Nagamine H, Ishiuchi S. Progression of cerebellar chronic encapsulated expanding hematoma during late pregnancy after gamma knife radiosurgery for arteriovenous malformation. Surg Neurol Int 2014;5:S575-9.
Available FREE in open access from: http://www.surgicalneurologyint.com/text.asp?2014/5/17/575/148054

Abstract

Background: The etiology and appropriate management strategy of chronic encapsulated expanding hematoma during pregnancy after gamma knife radiosurgery for arteriovenous malformation (AVM) remain unclear.

Case Description: A 34-year-old female developed chronic encapsulated expanding hematoma during late pregnancy, after angiographic disappearance of cerebellar AVM following two courses of gamma knife radiosurgery. The present case implicates pregnancy as a potential promoter of growth and enlargement of chronic encapsulated expanding hematoma, which may become life-threatening and require surgical intervention.

Conclusion: Immediate surgical management after delivery may be associated with a favorable outcome, so close follow-up management and patient education are very important in women planning pregnancy.

Key Words: Arteriovenous malformation, gamma knife, pregnancy, radiosurgery

Access this article online
Website: www.surgicalneurologyint.com
DOI: 10.4103/2152-7806.148054
Quick Response Code:

INTRODUCTION

Gamma knife radiosurgery is an effective treatment for cerebral arteriovenous malformation (AVM) resulting in angiographic disappearance in more than 80-90% of cases. Actual rates of obliteration of cerebellar AVMs, with median target volume of 3.85 cm^3 and median marginal dose of 21 Gy, were 53% at 3 years and 76% at 5 and 10 years.[1] However, relatively rare complications such as cyst formation and chronic encapsulated expanding hematoma may develop more than 5 years after gamma knife radiosurgery even if angiographic disappearance has been achieved.[4,10,15,16,19] Furthermore, little is known about the mechanisms and appropriate management of chronic encapsulated expanding hematoma during pregnancy. We present a case of cerebellar chronic encapsulated expanding hematoma encountered during late pregnancy, 4 years after angiographic disappearance of AVM nidus following two courses of gamma knife radiosurgery, with a cumulative dose of 44 Gy to the margin at the 50-60% isodose line, carried out at an interval of 4 years.

CASE REPORT

A 20-year-old female presented with sudden onset of severe headache associated with nausea followed by disturbance of consciousness, and was admitted to another hospital. The diagnosis of cerebellar and subarachnoid hemorrhage from AVM supplied by the

posterior inferior cerebellar artery (PICA) was based on the findings of computed tomography (CT) [Figure 1a] and cerebral angiography. Emergency evacuation of the hematoma was performed via a midline suboccipital approach. Four months after surgery, vertebral angiography demonstrated left cerebellar hemispheric AVM supplied by the PICA [Figure 1b]. Fourteen months after the initial hemorrhage, gamma knife radiosurgery was performed to treat the AVM nidus with a volume of 0.487 cm^3 at another institution using a Leksell Gamma Knife model B unit (Elekta AB). The procedure was planned using GammaPlan software based on stereotactic digital subtraction angiography and magnetic resonance (MR) imaging. A prescribed dose of 20 Gy was delivered to the lesion margin at the 50% isodose line. Three years after the first radiosurgery, vertebral angiography showed a small residual nidus in the left cerebellar hemisphere [Figure 1c]. The patient underwent repeat radiosurgery at the previous institution using a Leksell Gamma Knife model C unit (Elekta AB) 4 years after initial radiosurgery. The target volume of the nidus was 1.5 cm^3, a larger volume than that at the initial radiosurgery, and was intended to improve the treatment efficacy. The procedure was planned using GammaPlan software and a prescribed dose of 24 Gy was delivered to the lesion margin at the 60% isodose line. Vertebral angiography obtained at 5 years after the second radiosurgery revealed complete disappearance of the AVM [Figure 1d]. However, T2-weighted MR imaging and postcontrast T1-weighted MR imaging obtained at 7 years after the second radiosurgery revealed an enhanced lesion adjacent to the cyst formation in the left cerebellar hemisphere [Figure 2a, b]. The patient was lost to follow up during the 18 months after the last examination. The patient subsequently presented with headache and nausea, which had persisted over 3 weeks, at age 34 years in the 32nd week of pregnancy, and was referred to our institution 9 years after the second radiosurgery.

The patient had headache and nausea, but no other neurological deficits were identified except for House–Brackmann grade 3 facial palsy persisting since her childhood. Other medical history was unremarkable. On admission, CT demonstrated an irregularly shaped, heterogeneous high density hematoma with perifocal edema in the vermis extending to the left cerebellar hemisphere [Figure 2c]. Her infant was delivered by cesarean section immediately after admission and osmotic therapy was started. Despite conservative management, disturbance of consciousness developed and deteriorated due to the extensive perifocal edema and hydrocephalus. Three-dimensional CT angiography revealed no vascular abnormality around the lesion.

Midline suboccipital craniotomy was performed and cerebrospinal fluid was released from the ventricular drainage. A very firm, reddish angiomatous nodular granuloma with adjacent cyst was visualized in the cerebellar hemisphere. Indocyanine green videoangiography confirmed the absence of abnormal vasculature around the lesion. The lesion contained angiomatous capsule and firm organized hematoma. Gross total resection was achieved without injury to the surrounding structures. No AVM nidus was observed during surgery. Her symptom was completely resolved

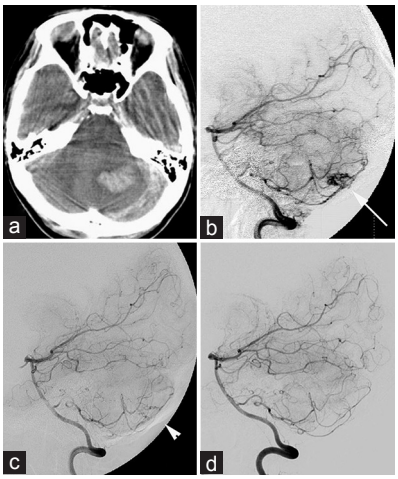

Figure 1: (a) CT scan at initial onset demonstrating left cerebellar hemorrhage with subarachnoid hemorrhage. (b) Left vertebral angiogram before first gamma knife radiosurgery showing a left cerebellar hemispheric AVM supplied by posterior inferior cerebellar artery (*arrow*). (c) Left vertebral angiogram at 3 years after first radiosurgery revealing residual nidus in the left cerebellar hemisphere (*arrowhead*). (d) Left vertebral angiogram obtained at 5 years after the second radiosurgery revealing no residual AVM nidus

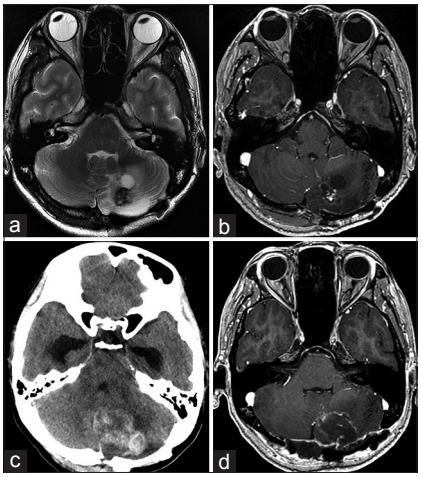

Figure 2: Axial T2-weighted MR image (a) and postcontrast T1-weighted MR image (b) demonstrating appearance of the enhanced lesion adjacent to the cyst formation in the left cerebellar hemisphere at 7 years after second radiosurgery. (c) CT scan showing an irregularly shaped, mixed density lesion with extensive edema in the left cerebellar hemisphere. (d) Postoperative gadolinium-enhanced T1-weighted MR image demonstrating total removal of the lesion

immediately after surgery and the postoperative course was uneventful. Postoperative MR imaging revealed total resection of the hematoma with the adjacent cyst [Figure 2d]. Postoperative angiography confirmed disappearance of the AVM. Her baby's growth and development was also normal.

Histological examination of the lesion obtained during surgery demonstrated encapsulated hematoma consisting of a dense collagenous outer layer and a granulated, newly vascularized, angiomatous inner layer with extensive multinodular hemorrhage at various stages of organization [Figure 3a]. Hemosiderin deposits and coagulation necrosis were also observed [Figure 3b]. The microvasculature in the inner layer demonstrated inflammatory infiltration in the vascular walls and thickening of the vessel walls with hyaline degeneration, which are characteristic findings of vasculitis [Figure 3c]. Immunohistochemical examination demonstrated strong staining for CD34 in the microvasculature [Figure 3d].

DISCUSSION

Chronic encapsulated expanding hematoma after gamma knife radiosurgery

Chronic encapsulated expanding hematoma is a rare but very important late onset complication after gamma knife radiosurgery for AVMs, and may develop even if angiographic disappearance has been achieved. Surgical treatment may be required due to progression in some cases.[10,15,19] Chronic encapsulated expanding hematoma is often accompanied by cyst formation, which tends to occur in patients followed up for longer than 5 years after gamma knife radiosurgery.[16] Larger nidus volume and higher radiation dose may be risk factors for delayed cyst formation,[4] but cyst formation may still occur despite a relatively small nidus and low prescribed margin dose.[19] Total obliteration can be achieved after repeat stereotactic radiosurgery (SRS) for incomplete obliteration after initial SRS.[8,9,13,23] Delayed cyst formation occurred in 4.6% of cases at a median of 108 months after repeat SRS. In the present case, chronic encapsulated expanding hematoma occurred 9 years after the second radiosurgery for the relatively small residual nidus. The cumulative radiation dose was 44 Gy to the lesion margin, which was presumably high enough to induce the hematoma.

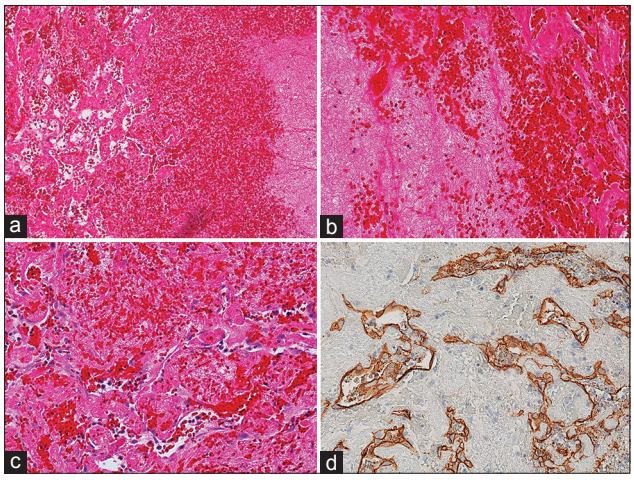

Figure 3: (a) Photomicrographs of the chronic encapsulated expanding hematoma demonstrating angiomatous abnormal vessels, multifocal hemorrhage, and coagulation necrosis. HE, original magnification ×100. (b) Areas of coagulation necrosis and extensive hemorrhage. HE, original magnification ×200. (c) Angiomatous region showing thickening of the vessel walls with hyaline degeneration and inflammatory infiltration. HE, original magnification ×200. (d) Immunohistochemical examination demonstrating strong staining for CD34 in the microvasculature. Original magnification ×200

Chronic encapsulated expanding hematoma during pregnancy

The present case of cerebellar chronic encapsulated expanding hematoma occurred during pregnancy, 9 years after the second radiosurgery. Such occurrence of chronic encapsulated expanding hematoma during pregnancy has not been reported previously, and the etiology and appropriate management strategies remain unclear. Several studies have demonstrated rapid enlargement of intracranial meningiomas during pregnancy.[11,14,22] The rate of presentation increased in the second and third trimesters. Several mechanisms, such as increased blood volume, vascular engorgement, increase in tumor-associated vascularity, increase in intracellular fluid, and increased edema, may explain both the rapid increase in tumor size during pregnancy as well as the frequent partial regression postpartum.[11,12,14,22] Recent studies showed that pregnancy and the puerperium are associated with increased risks of hemorrhage and aggressive behavior in cavernous malformations and other vascular lesions.[3,17] In the present case, the chronic encapsulated expanding hematoma became symptomatic in the third trimester, suggesting relatively rapid progression during pregnancy because this period was only 18 months after the last follow-up examination.

Recent experimental studies have revealed that representative histological changes in smaller arterioles or the microvasculature after irradiation are likely to be caused by microvasculitis, which consists of hyaline degeneration, fibrinoid necrosis, lymphocytic infiltration, and adventitial fibrosis.[2,6,7,18,21] Histological examination of the present case revealed extensive multifocal hemorrhage with multi-stage organization from abnormal angiomatous vessels with hyaline degeneration adjacent to coagulation necrosis. These findings are compatible with those of the experimental studies. On the basis of these findings, we suggest that repeated hemorrhage from the abnormal fragile

vasculature with subsequent multi-stage organization in the lesion occurred during pregnancy due to increased blood volume and vascular engorgement, and this may have caused the rapid enlargement of the hematoma and increased perifocal edema resulting in the progressive deterioration of neurological symptoms during late pregnancy.

The optimum timing for neurosurgical intervention in pregnant patients remains to be elucidated. The indications for surgery and delivery must be determined in relation to the severity of the neurological symptoms in the mother, the aggressiveness of the lesion, and the gestational period.[12] The general recommendation is that neurosurgical intervention should be avoided in the late second and third trimester, because of the high risk of intracranial hemorrhage associated with increased maternal intravascular volume. However, cesarean delivery under general anesthesia with subsequent neurological decompression should be considered for patients with risk of cerebellar herniation.[5,20] Chronic encapsulated expanding hematoma in the cerebellum may cause severe clinical problems and is potentially life-threatening because of the proximity to the brainstem and fourth ventricle. The urgency of such condition increases the likelihood of surgical intervention during pregnancy. Most obstetricians and pediatricians would consider that the delivery should be delayed to 32 weeks of gestation to ensure fetal maturity and survival. In the present case, the patient only complained of headache and was relatively stable on admission, so that cesarean section could be performed under general anesthesia immediately after admission, because the gestational age was 32 weeks and the condition of her infant was stable. After delivery, her neurological status rapidly deteriorated due to increased perifocal edema and development of hydrocephalus, so that midline suboccipital craniotomy was performed. Her neurological deficits were immediately resolved after surgery.

The present case implicates pregnancy as a potential promoter of growth and enlargement of chronic encapsulated expanding hematoma, which may become life-threatening and require surgical intervention. Accurate diagnosis and immediate surgical management after delivery are likely to result in favorable outcome. We suggest that cesarean section followed by craniotomy is indicated for patients with chronic encapsulated expanding hematoma who are neurologically unstable with conservative therapy in late pregnancy.

CONCLUSION

The present case shows that chronic encapsulated expanding hematoma after gamma knife radiosurgery may develop and increase the risk of hemorrhage, with more aggressive behavior during late pregnancy. Craniotomy and total removal of the lesion after delivery by cesarean section under general anesthesia resulted in good outcome. However, the patient should be warned of the risk of this life-threatening complication prior to attempts at becoming pregnant. Therefore, follow-up examinations should be regularly scheduled for young women of child bearing age after gamma knife radiosurgery for AVMs, despite the confirmation of angiographic disappearance of AVM nidus, because of the difficulty in predicting rapid progression of the chronic encapsulated expanding hematoma during pregnancy.

REFERENCES

1. Bowden G, Kano H, Tonetti D, Niranjan A, Flickinger J, Lunsford LD. Stereotactic radiosurgery for arteriovenous malformations of the cerebellum. J Neurosurg 2014;120:583-90.
2. Chuang VP. Radiation-induced arteritis. Seminars in roentgenology 1994;29:64-9.
3. Dias MS, Sekhar LN. Intracranial hemorrhage from aneurysms and arteriovenous malformations during pregnancy and the puerperium. Neurosurgery 1990;27:855-65.
4. Izawa M, Hayashi M, Chernov M, Nakaya K, Ochiai T, Murata N, *et al*. Long-term complications after gamma knife surgery for arteriovenous malformations. J Neurosurg 2005;102 Suppl: 34-7.
5. Jayasekera BA, Bacon AD, Whitfield PC. Management of glioblastoma multiforme in pregnancy. J Neurosurg 2012;116:1187-94.
6. Kamiryo T, Kassell NF, Thai QA, Lopes MB, Lee KS, Steiner L. Histological changes in the normal rat brain after gamma irradiation.Acta Neurochir (Wien) 1996;138:451-9.
7. Kamiryo T, Lopes MB, Berr SS, Lee KS, Kassell NF, Steiner L. Occlusion of the anterior cerebral artery after Gamma Knife irradiation in a rat. Acta Neurochir (Wien) 1996;138:983-90.
8. Kano H, Kondziolka D, Flickinger JC, Yang HC, Flannery TJ, Awan NR, *et al*. Stereotactic radiosurgery for arteriovenous malformations, Part 3: Outcome predictors and risks after repeat radiosurgery. J Neurosurg 2012;116:21-32.
9. Karlsson B, Kihlstrom L, Lindquist C, Steiner L. Gamma knife surgery for previously irradiated arteriovenous malformations. Neurosurgery 1998;42:1-5.
10. Kurita H, Sasaki T, Kawamoto S, Taniguchi M, Kitanaka C, Nakaguchi H, *et al*. Chronic encapsulated expanding hematoma in association with gamma knife stereotactic radiosurgery for a cerebral arteriovenous malformation. Case report. J Neurosurg 1996;84:874-8.
11. Lusis EA, Scheithauer BW, Yachnis AT, Fischer BR, Chicoine MR, Paulus W, *et al*. Meningiomas in pregnancy: A clinicopathologic study of 17 cases. Neurosurgery 2012;71:951-61.
12. Lynch JC, Gouvea F, Emmerich JC, Kokinovrachos G, Pereira C, Welling L, *et al*. Management strategy for brain tumour diagnosed during pregnancy. Br J Neurosurg 2011;25:225-30.
13. Maesawa S, Flickinger JC, Kondziolka D, Lunsford LD. Repeated radiosurgery for incompletely obliterated arteriovenous malformations. J Neurosurg 2000;92:961-70.
14. Moscovici S, Fraifeld S, Cohen JE, Dotan S, Elchalal U, Shoshan Y, *et al*. Parasellar meningiomas in pregnancy: Surgical results and visual outcomes. World Neurosurg 2013 Jul 10. pii: S1878-8750 (13) 00765-1. DOI: 10.1016/j.wneu.2013.06.019.
15. Nakamizo A, Suzuki SO, Saito N, Shono T, Matsumoto K, Onaka S, *et al*. Clinicopathological study on chronic encapsulated expanding hematoma associated with incompletely obliterated AVM after stereotactic radiosurgery. Acta Neurochir (Wien) 2011;153:883-93.

16. Pan HC, Sheehan J, Stroila M, Steiner M, Steiner L. Late cyst formation following gamma knife surgery of arteriovenous malformations. J Neurosurg 2005;102 Suppl: 124-7.
17. Safavi-Abbasi S, Feiz-Erfan I, Spetzler RF, Kim L, Dogan S, Porter RW, *et al*. Hemorrhage of cavernous malformations during pregnancy and in the peripartum period: Causal or coincidence? Case report and review of the literature. Neurosurg Focus 2006;21:e12.
18. Schultheiss TE, Kun LE, Ang KK, Stephens LC. Radiation response of the central nervous system. Int J Radiat Oncol Biol Phys 1995;31:1093-112.
19. Shuto T, Ohtake M, Matsunaga S. Proposed mechanism for cyst formation and enlargement following Gamma Knife Surgery for arteriovenous malformations. J Neurosurg 2012;117 Suppl: 135-43.
20. Tewari KS, Cappuccini F, Asrat T, Flamm BL, Carpenter SE, Disaia PJ, *et al*. Obstetric emergencies precipitated by malignant brain tumors. Am J Obstet Gynecol 2000;182:1215-21.
21. Watanabe T, Saito N, Hirato J, Shimaguchi H, Fujimaki H, Sasaki T. Facial neuropathy due to axonal degeneration and microvasculitis following gamma knife surgery for vestibular schwannoma: A histological analysis. Case report. J Neurosurg 2003;99:916-20.
22. Weyand RD, MacCarty CS, Wilson RB. The effect of pregnancy on intracranial meningiomas occurring about the optic chiasm. Surg Clin North Am 1951;31:1225-33.
23. Yen CP, Jain S, Haq IU, Jagannathan J, Schlesinger D, Sheehan J, *et al*. Repeat gamma knife surgery for incompletely obliterated cerebral arteriovenous. malformations. Neurosurgery 2010;67(1):55-64.

Biochemical and Biophysical Research Communications 457 (2015) 206–212

Contents lists available at ScienceDirect

Biochemical and Biophysical Research Communications

journal homepage: www.elsevier.com/locate/ybbrc

Identification of a novel cell-penetrating peptide targeting human glioblastoma cell lines as a cancer-homing transporter

Moritoshi Higa [a], Chiaki Katagiri [b], Chigusa Shimizu-Okabe [c], Tomoyuki Tsumuraya [a], Masanori Sunagawa [a], Mariko Nakamura [a], Shogo Ishiuchi [b], Chitoshi Takayama [c], Eisaku Kondo [d], Masayuki Matsushita [a,*]

[a] Department of Molecular and Cellular Physiology, Graduate School of Medicine, University of the Ryukyus, 903-0215 Okinawa, Japan
[b] Department of Neurosurgery, Graduate School of Medicine, University of the Ryukyus, 903-0215 Okinawa, Japan
[c] Department of Molecular Anatomy, Graduate School of Medicine, University of the Ryukyus, 903-0215 Okinawa, Japan
[d] Division of Molecular and Cellular Pathology, Niigata University Graduate School of Medical and Dental Sciences, 1-757 Asahimachi-dori, Chuou-ku, Niigata 951-8510, Japan

ARTICLE INFO

Article history:
Received 15 December 2014
Available online 3 January 2015

Keywords:
CPP
DDS
Peptide
Glioblastoma
Cancer

ABSTRACT

Cell-penetrating peptides (CPPs) as a novel biomedical delivery system have been highly anticipated, since they can translocate across biological membranes and are capable of transporting their cargo inside live cells with minimal invasiveness. However, non-selective internalization in various cell types remains a challenge in the clinical application of CPPs, especially in cancer treatment. In this study, we attempted to identify novel cancer-homing CPPs to target glioblastoma multiforme (GBM), which is often refractory and resistant to treatment. We screened for CPPs showing affinity for the human GBM cell line, U87MG, from an mRNA display random peptide library. One of the candidate peptides which amino-acid sequence was obtained from the screening showed selective cell-penetrating activity in U87MG cells. Conjugation of the $p16^{INK4a}$ functional peptide to the GBM-selective CPP induced cellular apoptosis and reduced phosphorylated retinoblastoma protein levels. This indicates that the CPP was capable of delivering a therapeutic molecule into U87MG cells inducing apoptosis. These results suggest that the novel CPP identified in this study permeates with high affinity into GBM cells, revealing it to be a promising imaging and therapeutic tool in the treatment of glioblastoma.

1. Introduction

Glioblastoma multiforme (GBM, WHO grade IV astrocytoma) is the most common malignant brain tumor originating in the central nervous system in adults. Despite advances in surgical resection, chemotherapy, and radiotherapy combined with adjuvant therapy, the median survival in patients with GBM is generally less than 12 months after the time of diagnosis because of its rapid progression and invasive nature [1]. Thus, there is an urgent need for more effective therapeutic strategies for refractory GBM.

Recently, cell-penetrating peptides (CPPs), also referred to as protein transduction domains (PTDs), which have the ability to permeate across the plasma membrane and can facilitate the efficient cellular internalization of biomolecules, have attracted attention as peptide-based delivery systems [2,3]. To date, CPPs such as the human immunodeficiency virus type1 (HIV-1) transcriptional activator TAT protein [4], the Antennapedia (Antp) homeodomain of *Drosophila* [5], and poly-arginine ((Arg)*n*, *n* = 4–16) [6,7] have been the most widely studied with respect to enhancing the intracellular delivery of CPP-conjugated molecules. Since these peptides could efficiently deliver a variety of biological macromolecules, including proteins, peptides, DNAs, RNAs and nanoparticles into various living cells with minimal cytotoxicity, the use of CPPs as a delivery system to directly introduce biologically active molecules into cells has been expected [2,8,9]. However, from a clinical point of view, non-selective internalization of CPPs into various cells is the limiting factor for cell-type or tissue specific targeting applications such as cancer treatments [4,10]. Development of target-selective CPPs may contribute to improving therapeutic efficacy and reducing side effects on normal tissues [11,12]. Accordingly, the purpose of the present study was to identify novel CPPs targeting GBM as selective transporters.

mRNA displayed peptides comprise a genotype (mRNA/cDNA) template and phenotype (nascent protein) that is encoded by its mRNA, and are linked by a covalent bond through the puromycin linker [13]. The *in vitro* cell-free protein synthesis system boasts a diversity of approximately 10^{12}–10^{13} individual sequences, each

* Corresponding author. Fax: +81 98 895 1402.
E-mail address: masayuki@med.u-ryukyu.ac.jp (M. Matsushita).

http://dx.doi.org/10.1016/j.bbrc.2014.12.089
0006-291X/

containing 10 contiguous random amino acids that are encoded by a synthetic cDNA library (templates), which is greater than that of phage display technology ($<10^9$) [14]. The amino acid sequence of an mRNA displayed polypeptide can be identified easily by nucleic acid sequencing [15,16]. Thus, mRNA display technology provides a means of screening for useful physiologically active peptides and novel functional proteins. Here, we aimed to investigate novel CPPs with an affinity for the U87MG human GBM cell line using an mRNA display random peptide library *in vitro*. In this article, we present a novel CPP as a potential tool for GBM selective intracellular delivery.

2. Materials & methods

2.1. Peptide synthesis

All peptides in the present study were synthesized chemically by SIGMA–ALDRICH (Tokyo, Japan). Peptide purity was 90% or greater, which was confirmed by high-performance liquid chromatography analysis and mass spectroscopy. Peptides were dissolved in distilled water to generate 1 mM stock solutions.

2.2. Cell culture

The human glioblastoma (GBM) cell line U87MG used in the present study was purchased from the American Type Culture Collection (USA). The other cell lines used for *in vitro* assays are shown in Table 1. All human cell lines were maintained in Dulbecco's modified Eagle's medium (DMEM) (Invitrogen) supplemented with 10% (v/v) heat-inactivated fetal bovine serum (FBS) (Invitrogen), 100 U/ml penicillin, and 100 μg/ml streptomycin (Invitrogen) at 37 °C with 5% CO_2. Primary cultured neurons were obtained from the hippocampus of 18-embryonic-day fetal C57BL6/J mice and maintained in neurobasal medium supplemented with 2% B-27 (Invitrogen), 1% penicillin/streptomycin, and 0.5 mM L-glutamine.

2.3. Fluorescence cellular imaging and quantitative analysis

Cells were seeded at a density of 3×10^5 cells per 35 mm glass bottom dish and incubated with 10 μM of FITC-labeled peptides in complete medium for 2 h at 37 °C. For fluorescence microscopy imaging, cells were washed twice with fresh medium, and cell fluorescence was immediately analyzed using confocal laser scanning microscopy (CLSM) (Olympus Tokyo Japan, FLUOVIEW FV-1000) without fixation. Fluorescence intensities at the region of interest (ROI) of 3 cells per microscopic image were measured by Meta Morph software Version 6 (Olympus), and experiments were conducted in triplicate. Background fluorescence intensity was subtracted from all experiments. For fluorescence-activated cells sorting (FACS) analysis, the cells were washed twice with phosphate-buffered saline (PBS) and collected by trypsinization. Detached cells were resuspended in FACS buffer (PBS, 2% FBS), then samples (1×10^4 cells) were immediately subjected to flow cytometric analysis (MILLIPORE Guava Easy Cyte Plus) using guava soft version2 (MILLIPORE) without fixation.

Table 1
Cell lines of histologically different origins, including human GBM, were used in the cell-penetration assay. Primary cultured mouse neurons were used as a non-neoplastic counterpart.

Cell line	Origin (histological type)
U87MG	Brain (glioblastoma)
U118MG	Brain (glioblastoma)
HeLa	Uterus (squamous cell carcinoma)
MSTO-211H	Lung (adenocarcinoma)
NCI-H226	Lung (adenocarcinoma)
A549	Lung (adenocarcinoma)
PANC-1	Pancreas (epithelioid carcinoma)
HepG2	Liver (hepatoblastoma)
Caco-2	Colon (adenocarcinoma)
HEK293	Non-neoplastic, embryonic kidney
Neuron	Brain (mouse hippocampal neuron)

2.4. RT-PCR

Total RNA was extracted with TRIzol (Invitrogen) from the human glioblastoma cell lines U87MG and U118MG, and HeLa cells. cDNA was synthesized from the RNA product using an oligo (dT) primer and cDNA synthesis kit (TAKARA) according to the manufacturer's instructions. Reverse transcription-PCR was performed with Ex-Taq polymerase (TAKARA) under the following amplification conditions: denaturation at 94 °C for 2 min, followed by 40 cycles of denaturation at 98 °C for 10 s, annealing at 55 °C for 30 s, extension at 72 °C for 2 min, and a final extension at 72 °C for 10 min. The sense/antisense primer sequences for human $p16^{INK4a}$ were 5′-TTCCTGGACACGCTGGTGGTG-3′ and5′-GGCATCTATGCGGG CATGGTTA-3′, respectively. Actin was used as internal standard gene.

2.5. Detection of apoptotic cells

U87MG cells were seeded at a density of 5×10^5 cells per 60 mm dish and incubated with 20 μM of peptide1NSΔ-p16 MIS or peptide1NSΔ-p16 V95E in complete medium for 4 h at 37 °C, respectively. After treatment, the cells were washed twice with PBS and collected by trypsinization. Then, the cells were resuspended in 100 μl of binding buffer (0.5 M HEPES pH 7.4, 1 M NaCl, 1 M KCl, 1 M $MgCl_2$, 0.2 M $CaCl_2$) containing 5 μl FITC-Annexin V (BD Pharmingen) and 5 μl Propidium iodide (PI) (SIGMA–ALDRICH), and incubated under darkness for 15 min according to the manufacturer's instructions. The cells were immediately subjected to flow cytometric analysis at 1×10^4 cells per sample.

2.6. Western blotting

U87MG cells were seeded at a density of 3×10^5 cells to 35 mm well plate and incubated with 20 μM of peptide1NSΔ-p16 MIS or peptide1NSΔ-p16 V95E in DMEM under a serum free condition for 24 h at 37 °C, respectively. After treatment, the cells were washed with complete medium and further incubated at 37 °C for 4 h. Then, the cells were lysed with 2× SDS sample buffer, and extracts were separated by sodium dodecyl sulfate polyacrylamide gel electrophoresis (SDS–PAGE) using an 8% SDS–PAGE gel and transferred onto a nitrocellulose membrane (BIO-RAD). After blocking with Blocking One (NACALAI TESQUE), the membrane was sequentially probed with the following antibodies: primary antibodies were rabbit polyclonal anti-Ser 807/811 phosphorylated pRB antibody 1:1000 (CST, Cell Signaling Technology), and anti-actin monoclonal antibody 1:3000 (Chemicon); secondary antibodies were anti-rabbit antibody 1:3000 (CST), and anti-mouse antibody 1:3000 (Millipore). After washing with Tris-buffered saline Tween solution (TBS-T), signals were detected using ECL Prime Western Blotting Detection Reagent (GE Healthcare) and Versa Doc (BIO-RAD). Quantifications were carried out by densitometric analysis using Quantity One software (BIO-RAD).

2.7. Statistical analysis

Statistical significance was calculated using Statcel 3 software (OMS publishing Inc.). A student's *t*-test was used for data analysis and p value <0.05 was considered statistically significant. All values

are shown as means ± standard deviation (SD) from at least 3 independent experiments.

3. Results

3.1. Screening for candidate CPPs targeting U87MG GBM cells

First, to identify peptides capable of permeating into glioblastoma multiforme (GBM), we screened for cell-penetrating peptides (CPPs) targeting the human GBM cell line U87MG from an mRNA displayed random peptide library (Fig. 1A). The mRNA display library was constructed as previously described [13]. From about 60 sequences derived from concentration libraries, we randomly selected ten candidates and synthesized chemically fluorescein isothiocyanate (FITC)-labeled peptides (Fig. 1B). Nona-arginine (RRRRRRRRR: R9) was used as a nonselective permeation CPP. To evaluate the cell-penetrating activity of these peptides, U87MG cells were incubated with 10 μM of each numbered FITC-labeled peptide. We examined intracellular fluorescence signals in cells using confocal laser scanning microscopy (CLSM) (Fig. 1C). Moreover, we confirmed their mean fluorescence intensity using Meta Morph software (Fig. 1D). Consequently, we identified a novel CPP, peptide1 (NTCTWLKYHS), whose cell-penetrating activity was stronger than the other candidates.

3.2. Peptide1 is incorporated selectively into GBM cells

Because peptide1 showed the best cell-penetrating activity into U87MG cells, we further investigated its GBM cell selectivity using cells derived from various tissues (Table 1). Fluorescent images and quantitative analysis showed high selective permeability of the peptide1 into U87MG cells compared with other cell lines (Fig. 2A and B). As shown in Fig. 2C, FITC-labeled peptide1 also permeated into the U118MG GBM cell line. These results indicate that peptide1 might have selective permeability into GBM cells.

3.3. Peptide1-NSΔ exhibits increased cell-penetrating activity in U87MG cells

To improve penetration efficiency, we modified the amino acid sequence of peptide1. In one sequence, Cys (C) was substituted with Gly (G), because Cys might allow disulfide bonding to other proteins; in the other sequences, N- and/or C-terminus amino acid residues were deleted in each mutant peptide (Table 2). We synthesized seven FITC-labeled peptide1 variants, and examined intracellular fluorescence signals in U87MG cells using CLSM and flow cytometry. Images showed that the fluorescence signals of peptide1-NSΔ (TCTWLKYH) and peptide1-NTSΔ (CTWLKYH) increased compared with peptide1, although they were inferior to R9 as a

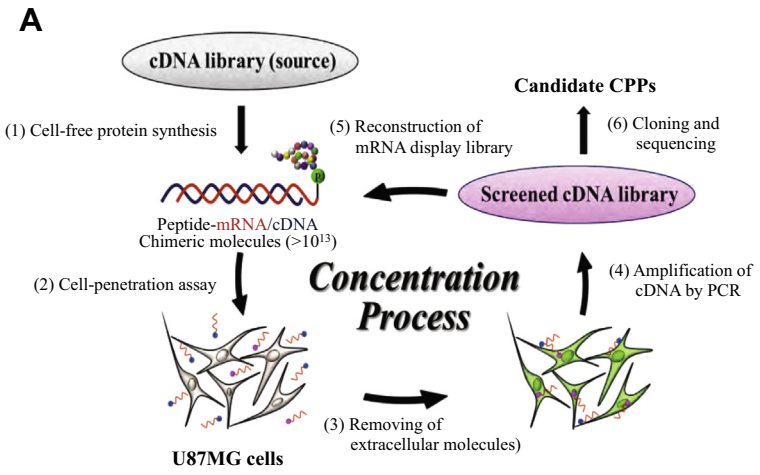

B

Peptide	Amino acid sequence	Length (a.a.)
Peptide 1	NTCTWLKYHS	10
Peptide 2	CASGQQGLLKLC	12
Peptide 3	YNNFAYSVFL	10
Peptide 4	ECYPKKGQDP	10
Peptide 5	RHVYHVLLSQ	10
peptide 6	HATKSQNINF	10
Peptide 7	YRDRFAFQPH	10
Peptide 8	IWRYSLASQQ	10
Peptide 9	YQKQAKIMCS	10
peptide 10	VQLRRRWC	8
R9	RRRRRRRRR	9

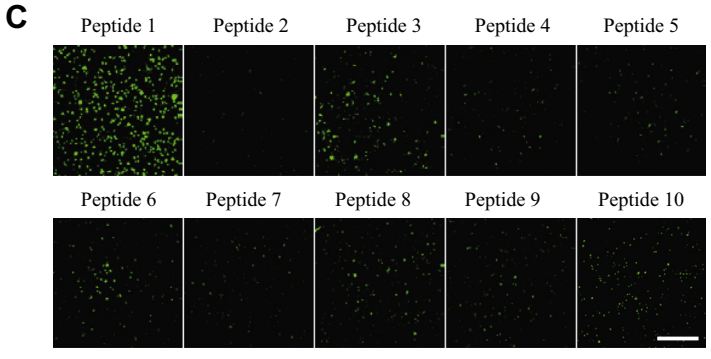

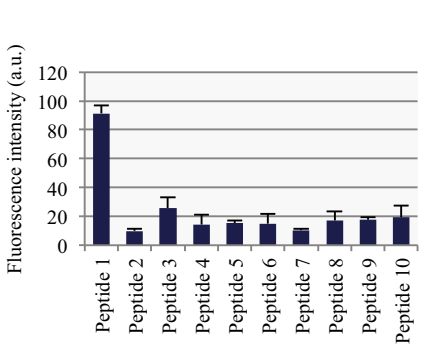

Fig. 1. Screening of candidate CPPs with an affinity for U87MG cells. (A) Scheme of screening for CPPs using mRNA display technology. (1) Construction of mRNA display random peptide libraries in a cell-free translation system. (2) Peptide libraries in the solution were added to the U87MG cell medium. (3) Extracellular peptides were removed by trypsinization and washing. (4) The genomes of chimeric molecules incorporated into the cells were recovered and amplified by their anchored template cDNA using PCR. (5) Reconstruction of mRNA display random peptide libraries for the next selection cycles. (6) After the selection cycles, the peptide sequences of candidate CPPs were predicted by cloning and sequencing. (B) List of peptide sequences selected randomly from the peptides obtained by screening. Poly-arginine (R9) was used as a representative nonselective permeable CPP. (C) U87MG cells were treated with 10 μM of each numbered FITC-labeled peptide for 2 h at 37 °C. Fluorescence images were observed using CLSM. Scale bar, 200 μm. (D) Meta Morph quantitative analysis of fluorescence intensity of ten candidate CPPs in U87MG cells. The mean fluorescence intensity of the peptides against background was calculated in each image obtained by fluorescence microscopy a.u.; arbitrary unit. Data are presented as the means ± SD of 3 independent experiments.

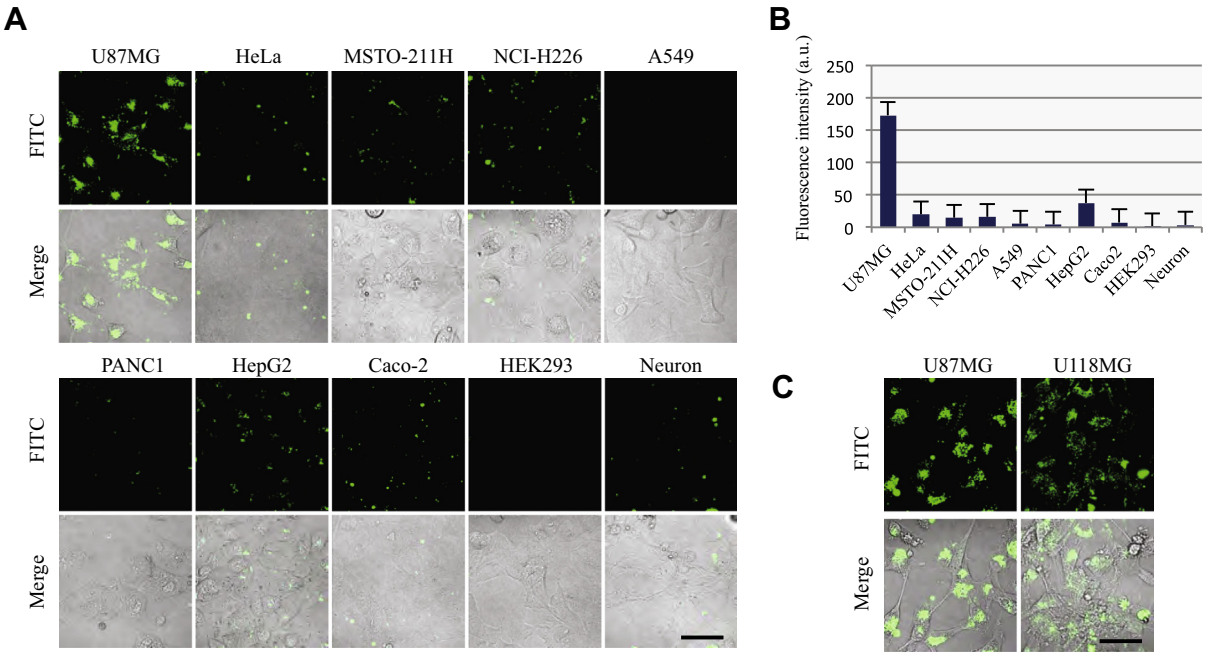

Fig. 2. Cell-penetration assay of peptide1 using cells derived from various tissues. (A) Histologically different cell types were treated with 10 μM of FITC-labeled peptide1 for 2 h at 37 °C. Fluorescence images were observed using CLSM. Scale bar, 50 μm. (B) Meta Morph quantitative analysis of fluorescence intensity of peptide1 in cells. The mean fluorescence intensity of peptide1 against background was calculated in each image obtained by fluorescence microscopy a.u.; arbitrary unit. Data are presented as the means ± SD of 3 independent experiments. (C) Fluorescence images of FITC-labeled peptide1 in U118MG. These cells were treated under the same conditions as mentioned above.

positive control (Fig. 3A). Fluorescence-activated cell sorting (FACS) analysis revealed that intracellular localization of the FITC-labeled peptide1-NSΔ was 2.0-fold higher than that of peptide1 (Fig. 3B). On the other hand, C3G (NTGTWLKYHS), NTCSΔ (TWLKYH), and NTHSΔ (CTWLKY) were decreased. Further, fluorescence images and quantitative analysis showed that peptide1-NSΔ preserves the permeability into U87MG and U118MG cell lines (Fig. 3C and D). These results suggest that peptide1-NSΔ has potential as a GBM homing intracellular transporter.

3.4. Antitumor effect of p16 MIS fusion peptide1-NSΔ against U87MG cells

Deficiency of the $p16^{INK4a}$ tumor suppressor gene is frequently found in the majority of human cancers including GBM [17]. Expression loss of the $p16^{INK4a}$ gene in both U87MG and U118MG cell lines was confirmed by reverse transcription-PCR (Fig. 4A). Therefore, to assess whether peptide1-NSΔ can deliver cargo into U87MG cells, we focused on a small peptide that comprises the minimal inhibitory sequence of p16 (FLDTLVVLHR: p16 MIS), the function of which was described in previous studies [18,19]. The antitumor peptide was designed by fusing peptide1-NSΔ and p16 MIS (peptide1NSΔ-p16 MIS) via the Gly-Pro-Gly spacer, and R4 (RRRR) was tagged at its C-terminus to enhance solubility. Peptide1NSΔ-p16 V95E, which substitutes valine 95 (V95) in the MIS sequence with glutamate (E), was used as a control (Fig. 4B). U87MG cells were treated with 20 μM of peptide1NSΔ-p16 MIS or peptide1NSΔ-p16 V95E for 4 h. After treatment, FACS analysis using Annexin V-FITC and PI (propidium iodide) showed that the early apoptosis rate increased significantly in the p16 MIS conjugate-treated cells (70 ± 6.25%) compared with p16 V95E conjugate-treated cells (10 ± 3.26%) and untreated cells (12 ± 1.70%) (Fig. 4C, right graph). Furthermore, to confirm whether cellular apoptosis was caused by the p16 MIS, we examined the phosphorylation status of retinoblastoma protein (pRB), which is regulated by Cdk4/6, the target for $p16^{INK4a}$. Twenty-four hours after treatment, western blot analysis revealed that phosphorylated pRB (p-pRB) ($Ser^{807/811}$ phosphorylation) was significantly decreased only in the p16 MIS-treated cells compared with the p16 V95E-treated cells. The p-pRB levels of untreated cells and p16 V95E-treated cells were the same in U87MG cells (Fig. 4D and E). The levels of phosphorylated pRB correlate with the induction of early apoptosis shown in Fig. 4C. These results demonstrated that peptide1-NSΔ can deliver the p16 functional peptide into U87MG cells as a transporter.

Table 2
Peptide1-C3G was substituted Cys (C) with Gly (G), and peptide1 deletion series were made by deleting residues from N- and/or C-terminus.

Peptide	Amino acid sequence	Length (a.a.)
Peptide 1	NTCTWLKYHS	10
Peptide 1-C3G	NTGTWLKYHS	10
Peptide 1-NΔ	TCTWLKYHS	9
Peptide 1-SΔ	NTCTWLKYH	9
Peptide 1-NSΔ	TCTWLKYH	8
Peptide 1-NTSΔ	CTWLKYH	7
Peptide 1-NTCSΔ	TWLKYH	6
Peptide 1-NTHSΔ	CTWLKY	6

4. Discussion

Targeted cancer therapy holds promise by reducing adverse effects on normal cells and enhancing therapeutic effects [20]. Because CPPs have high biocompatibility and can deliver efficiently a variety of biologically active cargos into cells, studies of cancer-specific drug delivery systems using CPPs have been widely carried out.

In the present study, we report on the GBM selective CPP, peptide1-NSΔ (TCTWLKYH), which was obtained using mRNA display technology. A protein database search revealed that this peptide appears to encode an artificial sequence, as it has no significant

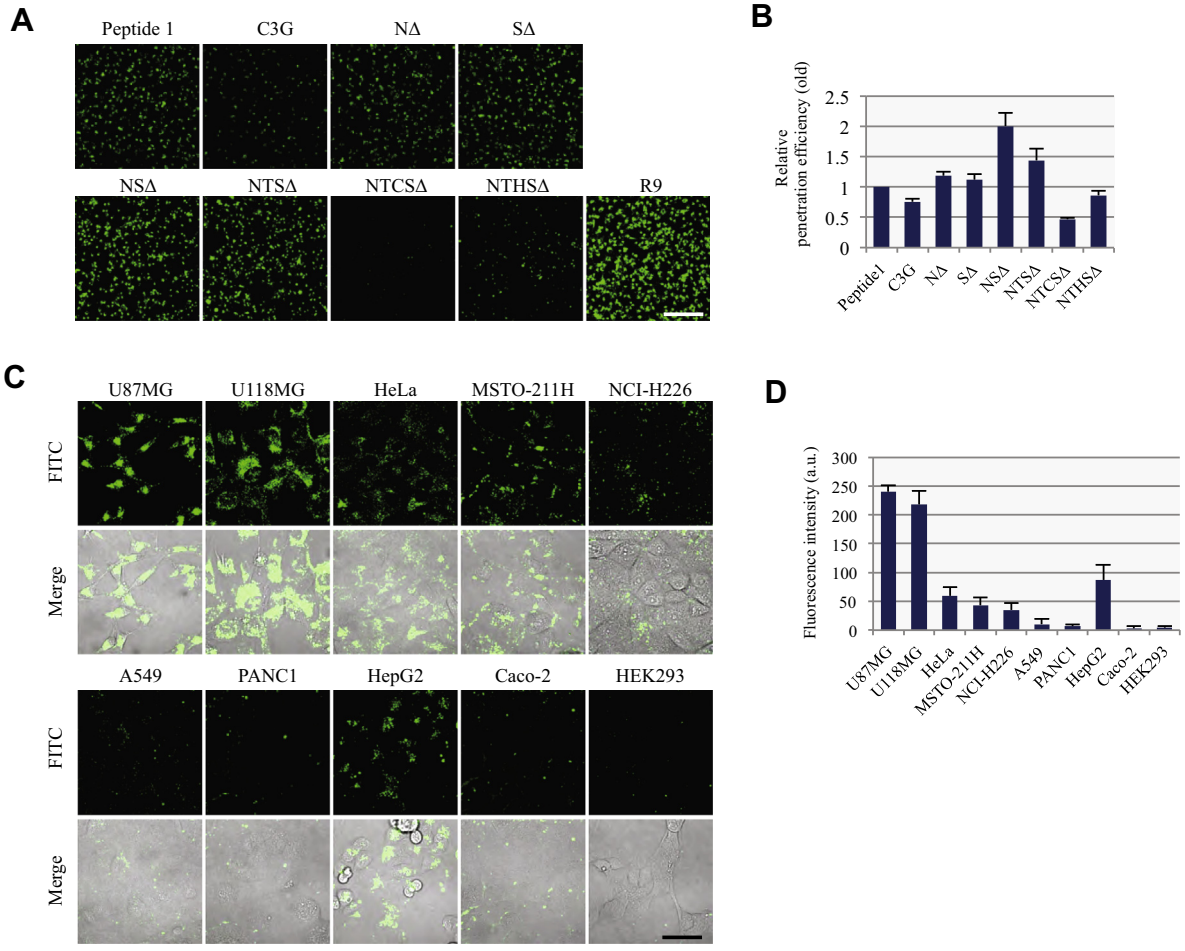

Fig. 3. Analysis of the cell-penetration efficiency of peptide1 variants. (A) U87MG cells were treated with 10 μM of FITC-labeled peptide1 variants for 2 h at 37 °C. Fluorescence images were observed using CLSM. Scale bar, 200 μm. (B) FACS quantitative analysis of mean fluorescence intensity of the peptide1 variants in U87MG cells. The relative fluorescence intensity of each peptide compared with peptide1 (1.0) was measured using flow cytometry. Data are presented as means ± SD of 3 independent experiments. (C) Histologically different cell types were treated with 10 μM of FITC-labeled peptide1-NSΔ for 2 h at 37 °C. Fluorescence images were observed using CLSM. Scale bar, 50 μm. (D) Meta Morph quantitative analysis of fluorescence intensity of peptide1-NSΔ in cells. The mean fluorescence intensity of peptide1-NSΔ against background was calculated in each image obtained by fluorescence microscopy a.u.; arbitrary unit. Data are presented as means ± SD of 3 independent experiments.

identity to any recorded mammalian proteins, including previously reported CPP sequences. The fluorescence-labeled peptide1-NSΔ was incorporated selectively into U87MG GBM cells *in vitro* (Fig. 3C and D). In most human malignancies, genetic abnormality of tumor suppressor genes has been well characterized [21]. In particular, expressional loss of $p16^{INK4a}$ occurs in U87MG cells (Fig. 4A) [22,23]. The $p16^{INK4a}$ tumor-suppressor gene has been found to be homozygously deleted, mutated or transcriptionally inhibited by methylation in GBMs [24]. $p16^{INK4a}$ binds directly to and inhibits the activity of CDK4 and CDK6, the D-type cyclin-dependent kinases that initiate the phosphorylation of pRB [25], leading to cellular apoptosis and senescence as a result of G1/S phase cell cycle arrest [26]. Analysis of a variety of human cancers has revealed a pattern in the pathway, in which only one of the four members such as cyclin D1, CDK4/CDK6, p16, and pRB of the $p16^{INK4a}$/CDK/pRB pathway is inactivated [27]. Therefore, restoration of the p16INK4a/CDK/pRB pathway is proposed to be an attractive target for therapeutic intervention because of its important role in cancer development as a cell cycle-regulatory pathway. The peptide1-NSΔ conjugated p16 MIS functional peptide induced a decrease in the level of phosphorylated pRB and an increase in early cellular apoptosis (Fig. 4C and D). These results suggest that peptide1-NSΔ can deliver imaging and antitumor agents into U87MG cells as a transporter.

In previous studies, CPPs such as HIV1-TAT and poly-arginine were used as intracellular delivery vehicles in a variety of cell types including peripheral blood lymphocytes, diploid human fibroblasts, keratinocytes, bone marrow stem cells, osteoclasts, fibrosarcoma cells, osteosarcoma, glioma, hepatocellular carcinoma, renal carcinoma, and NIH 3T3 cells (mouse fibroblast-like cell line) [4]. The most important observation in this study is that peptide1-NSΔ was incorporated selectively into GBM cell lines as compared with other cell lines (Fig. 3C). Although the mechanism responsible for the selective penetration of peptide1-NSΔ into GBM remains unclear, this unique ability differs notably from the existing CPPs mentioned previously, which enables the targeting function as a GBM-homing peptide.

This study has several limitations. Fluorescence signals of peptide1-NSΔ were detected at low levels in several cell lines, especially HepG2 and HeLa cells (Fig. 3D). Therefore, these findings may indicate that the level of selectivity requires further improvement in order to warrant designation as a GBM-specific delivery system. Moreover, when we added p16 MIS conjugates to the cell culture medium, aggregates in the medium were observed (data not shown), probably due to the interaction of proteins contained in the medium with the conjugates. This observation indicates that the functionality of this system is likely to be limited by solubility issues. Also, it seems likely that various environmental factors,

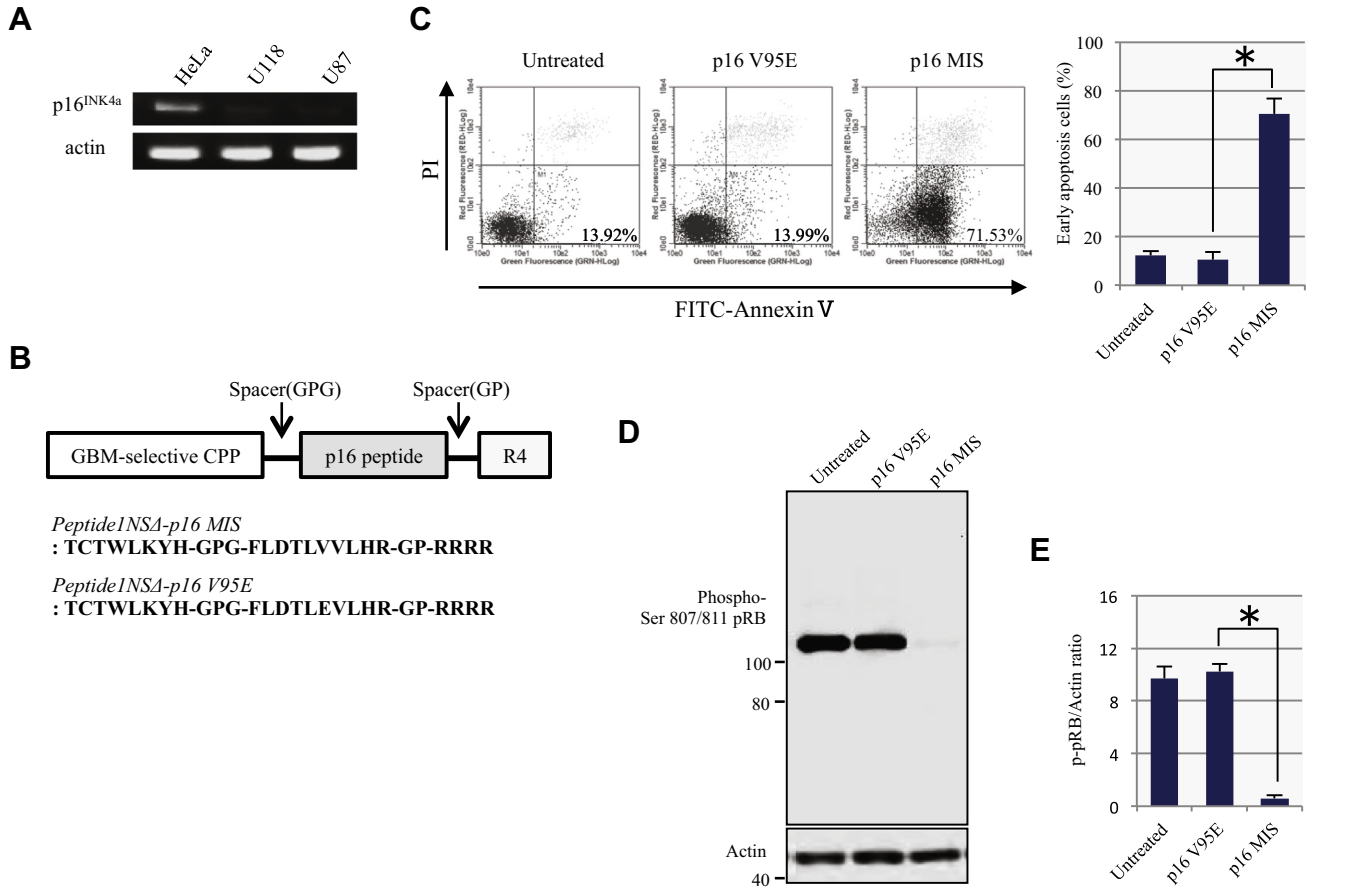

Fig. 4. Therapeutic effect of peptide1NSΔ-p16 MIS conjugates against U87MG cells. (A) RT-PCR analysis of the endogenous mRNA expression of the $p16^{INK4a}$ tumor suppressor gene in two human GBM cells, U87MG and U118MG. HeLa cells were used as a positive control. (B) Design of CPP-p16 antitumor peptide conjugate, which is composed of peptide1-NSΔ and the functional amino acid sequence of $p16^{INK4a}$ (p16 MIS: minimal inhibitory sequence). p16 V95E was used as a control that substitutes valine 95 (V95) in the MIS sequence with glutamate (E). (C) FACS analysis for cellular apoptosis in U87MG cells treated with 20 μM of peptide1-NSΔ fused with p16 MIS or p16 V95E for 4 h, respectively. Cells in the lower right quadrant (Annexin V positive/PI negative) represent early apoptotic cells. Percentage of early apoptotic cells (right). Data are presented as the means ± SD of 3 independent experiments per treatment group. (D) Phospho-$Ser^{807/811}$ pRB (p-pRB) status in U87MG cells was assessed by western blotting. Cells were treated with 20 μM of peptide1-NSΔ fused with p16 MIS or p16 V95E for 24 h, respectively. (E). Ratio of p-pRB/actin of (D). Data are presented as the means ± SD of 3 independent experiments per treatment group. Significant differences of $p < 0.01$ (*) are indicated.

including concentration, treatment time, medium components, and cell sensitivity, are involved in an optimum effect. Thus, further improvement of both the solubility and stability of the p16 MIS conjugate in the medium is needed.

In conclusion, we identified a novel CPP, peptide1-NSΔ, which exhibits selectivity to the U87MG GBM cell line and is capable of delivering its payload into cells *in vitro*. Our findings may provide new avenues for both effective therapeutics and diagnostics in clinical applications as a peptide based delivery system. However, the critical mechanism of tumor selectivity remains to be elucidated. Consequently, further research is required to clarify the GBM-selective recognition mechanisms.

Conflict of interest

The authors disclose no potential conflicts of interest.

Acknowledgments

This research was supported by grants-in-aid for scientific research from the Japanese Ministry of Education, Culture, Sports, Science and Technology (MEXT) (M.M.). This research was also supported by the Uehara Memorial Foundation, Takeda Science Foundation, Special Account Budget for Education and Research granted from MEXT and The Promotion Project of Medical Clustering of Okinawa prefecture (M.M.).

References

[1] R. Stupp, W.P. Mason, M.J. van den Bent, M. Weller, B. Fisher, M.J.B. Taphoorn, et al., Radiotherapy plus concomitant and adjuvant temozolomide for glioblastoma, N. Engl. J. Med. 352 (2005) 987–996, http://dx.doi.org/10.1056/NEJMoa043330.
[2] J.S. Wadia, S.F. Dowdy, Protein transduction technology, Curr. Opin. Biotechnol. 13 (2002) 52–56.
[3] M.C. Morris, J. Depollier, J. Mery, F. Heitz, G. Divita, A peptide carrier for the delivery of biologically active proteins into mammalian cells, Nat. Biotechnol. 19 (2001) 1173–1176, http://dx.doi.org/10.1038/nbt1201-1173.
[4] S.A. Ezhevsky, S.F. Dowdy, Hikaru Nagahara, Adamina M. Vocero-Akbani, Eric L. Snyder, Alan Ho, Dawn G. Latham, Natalie A. Lissy, Michelle Becker-Hapak, Transduction of full-length TAT fusion proteins into mammalian cells : TAT-p27 Kip1 induces cell migration, Nat. Med. (1998) 1449–1452
[5] D. Derossi, A.H. Joliot, G. Chassaing, A. Prochiantz, The third helix of the Antennapedia homeodomain translocates through biological membranes, J. Biol. Chem. 269 (1994) 10444–10450.
[6] S. Futaki, T. Suzuki, W. Ohashi, T. Yagami, S. Tanaka, K. Ueda, et al., Arginine-rich peptides, J. Biol. Chem. 276 (2001) 5836–5840, http://dx.doi.org/10.1074/jbc.M007540200.
[7] E. Kondo, M. Seto, K. Yoshikawa, Highly efficient delivery of p16 antitumor peptide into aggressive leukemia / lymphoma cells using a novel transporter system, Mol. Cancer Ther. (2005) 1623–1630
[8] H. Noguchi, S. Matsumoto, Protein transduction technology: a novel therapeutic perspective, Acta Med. Okayama 60 (2006) 1–11.
[9] E. Koren, V.P. Torchilin, Cell-penetrating peptides: breaking through to the other side, Trends Mol. Med. 18 (2012) 385–393.

[10] S.F.D. Jehangir, S. Wadia, Transmembrane delivery of protein and peptide drugs by TAT-mediated transduction in the treatment of cancer, Adv. Drug Deliv. Rev. (2005) 579–596
[11] K.J. Lim, B.H. Sung, J.R. Shin, Y.W. Lee, D.J. Kim, K.S. Yang, et al., A cancer specific cell-penetrating peptide, BR2, for the efficient delivery of an scFv into cancer cells, PLoS ONE 8 (2013) e66084, http://dx.doi.org/10.1371/journal.pone.0066084.
[12] E. Kondo, K. Saito, Y. Tashiro, K. Kamide, S. Uno, T. Furuya, et al., Tumour lineage-homing cell-penetrating peptides for peptide-based anti-cancer molecular delivery systems, Nat. Commun. 951 (2012) 1–13.
[13] K. Kamide, H. Nakakubo, S. Uno, A. Fukamizu, Isolation of novel cell-penetrating peptides from a random peptide library using in vitro virus and their modifications, Int. J. Mol. Med. 25 (2010) 41–51, http://dx.doi.org/10.3892/ijmm.
[14] D. Lipovsek, A. Plu, In-vitro protein evolution by ribosome display and mRNA display, J. Immunol. Methods 290 (2004) 51–67, http://dx.doi.org/10.1016/j.jim.2004.04.008.
[15] N. Nemoto, E. Miyamoto-Sato, Y. Husimi, H. Yanagawa, In vitro virus: bonding of mRNA bearing puromycin at the 3'-terminal end to the C-terminal end of its encoded protein on the ribosome in vitro, FEBS Lett. 414 (1997) 405–408.
[16] E. Miyamoto-Sato, M. Ishizaka, K. Horisawa, S. Tateyama, H. Takashima, S. Fuse, et al., Cell-free cotranslation and selection using in vitro virus for high-throughput analysis of protein-protein interactions and complexes, Genome Res. 15 (2005) 710–717, http://dx.doi.org/10.1101/gr.3510505.
[17] H. Ohgaki, P. Kleihues, Genetic pathways to primary and secondary glioblastoma, Am. J. Pathol. 170 (2007) 1445–1453, http://dx.doi.org/10.2353/ajpath.2007.070011.
[18] K.L. Ball, D.P. Lane, Robin Fahraeus, Sonia Lain, Characterization of the cyclin-dependent kinase inhibitory domain of the INK4 family as a model for a synthetic tumour suppressor molecule, Oncogene 16 (1998) 587–596.
[19] E. Kondo, T. Tanaka, T. Miyake, T. Ichikawa, M. Hirai, M. Adachi, et al., Potent synergy of dual antitumor peptides for growth suppression of human glioblastoma cell lines, Mol. Cancer Ther. 7 (2008) 1461–1471, http://dx.doi.org/10.1158/1535-7163.MCT-07-2010.
[20] L. Agemy, D. Friedmann-Morvinski, V.R. Kotamraju, L. Roth, K.N. Sugahara, O.M. Girard, et al., Targeted nanoparticle enhanced proapoptotic peptide as potential therapy for glioblastoma, Proc. Natl. Acad. Sci. U.S.A. 108 (2011) 17450–17455, http://dx.doi.org/10.1073/pnas.1114518108.
[21] M. Weller, J. Rieger, C. Grimmel, E.G. Van Meir, N. De Tribolet, S. Krajewski, et al., Predicting chemoresistance in human malignant glioma cells: the role of molecular genetic analyses, Int. J. Cancer 79 (1998) 640–644.
[22] J. He, J.J. Olson, C.D. James, C. Lines, Lack of p16 INK4 or retinoblastoma protein (pRb), or amplification-associated overexpression of cdk4 Is observed in distinct subsets of malignant glial tumors and cell lines, Cancer Res. 55 (1995) 4833–4836.
[23] F.D. Ragione, G.L. Russo, A. Oliva, C. Mercurio, S. Mastropietro, V.D. Pietra, et al., Biochemical characterization of p16INK4- and p18-containing complexes in human cell lines, J. Biol. Chem. 271 (1996) 15942–15949, http://dx.doi.org/10.1074/jbc.271.27.15942.
[24] M.A. Al-Mohanna, P.S. Manogaran, Z. Al-Mukhalafi, K. A Al-Hussein, A. Aboussekhra, The tumor suppressor p16(INK4a) gene is a regulator of apoptosis induced by ultraviolet light and cisplatin, Oncogene 23 (2004) 201–212, http://dx.doi.org/10.1038/sj.onc.1206927.
[25] J. Calbó, M. Marotta, M. Cascalló, J.M. Roig, J.L. Gelpí, J. Fueyo, et al., Adenovirus-mediated wt-p16 reintroduction induces cell cycle arrest or apoptosis in pancreatic cancer, Cancer Gene Ther. 8 (2001) 740–750, http://dx.doi.org/10.1038/sj.cgt.7700374.
[26] K. Zennami, K. Yoshikawa, E. Kondo, K. Nakamura, Y. Upsilonamada, M.A. De Velasco, et al., A new molecular targeted therapeutic approach for renal cell carcinoma with a p16 functional peptide using a novel transporter system, Oncol. Rep. 26 (2011) 327–333, http://dx.doi.org/10.3892/or.2011.1290.
[27] K. Fujimoto, R. Hosotani, Y. Miyamoto, R. Doi, T. Koshiba, A. Otaka, et al., Inhibition of pRb phosphorylation and cell cycle progression by an antennapedia-p16(INK4A) fusion peptide in pancreatic cancer cells, Cancer Lett. 159 (2000) 151–158.